UNIVERSITY OF NOVA GORICA
GRADUATE SCHOOL

STUDY OF INITIAL GROWTH OF PENTACENE ON GRAPHENE

DISSERTATION

Manisha Chhikara

Mentor: Prof. dr. Gvido Bratina

Nova Gorica, 2014

UNIVERZA V NOVI GORICI
FAKULTETA ZA PODIPLOMSKI ŠTUDIJ

ŠTUDIJ ZAČETNE RASTI PENTACENA NA GRAFENU

DISERTACIJA

Manisha Chhikara

Mentor: Prof. dr. Gvido Bratina

Nova Gorica, 2014

Acknowledgments

I am grateful to my supervisor Prof. dr. Gvido Bratina for his support throughout my PhD dissertation. He gave me freedom to work on my own ideas which helped me a lot to become an independent researcher on graphene field. Not only he is a good scientist but a tremendous person. I am fortunate to graduate under his guidance.

I am also thankful to my labmate Egon Pavlica for his fruitful discussions and friendly nature. His assistance helped me in getting expertise on atomic force microscope which was a crucial tool for my research. I would also like to thank all the colleagues for their friendly nature that helped to work in a healthy atmosphere.

I would also like to thank the collaborator Aleksandar Matkovic from Institute of Physics, Belgrade, Serbia for his continuous support and crucial discussions for the experimental work. I would like to express my gratitude to Prof. dr. Gajic Rados for allowing me for such a wonderful collaboration in his lab.

I would like to thank my parents, relatives for their endless affection and support throughout my dissertation and in maintaining harmony between me and my work. Most importantly, I thank to my sister Pooja Chhikara for being great inspiration to me and for her support throughout my life.

Last but not the least, apart from my efforts, I thank God for giving me such a wonderful life and courage to fulfil my dreams.

Abstract

We have examined growth of ultrathin pentacene layers on graphene using atomic force microscope (AFM). Graphene prepared from two different methods was used as a substrate for growth of pentacene. Firstly, graphene prepared by chemical vapour deposition (CVD) and secondly by micromechanical exfoliation from KISH graphite. The first part of our research is focused on growth of pentacene on single layer graphene fabricated by CVD method. We have used wet chemical route to transfer graphene from Copper foil to a 300 nm-thick SiO_2 substrate using polymethyl methacrylate (PMMA) as a support. Extensive heating in H_2/Ar was used to clean the PMMA off the graphene surface. Morphology of transferred graphene was examined by AFM prior to pentacene deposition. We have observed from surface analysis that graphene is characterized by folds. Folds in graphene—grafolds are frequently present even after transferring graphene layers onto the substrates. Typical height of grafolds ranges from 1 nm to 6 nm. We observe that grafolds have a crucial role in determining the morphology of pentacene layers on graphene. Our AFM investigation of the initial stages of growth of vacuum-evaporated pentacene on CVD graphene shows three-dimensional growth at submonolayer coverage of pentacene. Moreover, islands were found to preferentially nucleate at the location of the grafolds. With increasing pentacene thickness, pentacene islands acquire an elongated shape, which is likely a consequence of compensation of the elastic strain resulting from lattice mismatch. Kelvin force microscopy (KFM) reveals that grafolds exhibit substantially different contact potential that unfolded graphene. Preferential nucleation of pentacene on grafolds is therefore likely a consequence of increased chemical reactivity of grafolds.

The second part of our work focussed on the deposition of sub-monolayers of pentacene on graphene prepared by micromechanical exfoliation of graphite. We have examined morphology of sub-monolayer thick pentacene layers, deposited on exfoliated single-layer and bilayer graphene, transferred onto SiO_2. We observe two-dimensional (2D) island growth in the range of substrate temperatures from 10 °C to 60 °C. Height of pentacene islands is 1.5 nm which corresponds to thin-film phase. For substrate temperature < 40 °C, islands are significantly smaller in size than the system size. We find that island size distributions on single-layer graphene are broader and centered at higher average island areas than on bilayer graphene. However, at substrate temperature 50 °C and 60 °C, islands are enlarged due to rapid

coalescence. Islands in this regime correspond to percolation regime. We have found activation energy for molecule aggregation of E_a= 427±25 meV, and E_a= 537±46 meV for single layer and bilayer graphene, respectively. We associate the observed differences in pentacene layer morphology with the influence of the dipole field that can be associated with the water layer at the graphene/SiO_2 interface.

Furthermore, we have analysed early stages of growth of pentacene on mechanically exfoliated single layer graphene at different pentacene coverages. Island size distribution of pentacene has been examined for coverage in the range $0.07 < \theta < 0.40$ at substrate temperature, T_s = 29 °C. We have observed that width of the island size distribution increases with coverage and centroid moves to larger island size. On the contrary, pentacene on graphene flakes that were annealed at 350 °C for 3 hours proceeds in three-dimensional (3D) growth mode. Height of 3D islands is 25 nm on annealed graphene samples. In order to elucidate the role of SiO_2/graphene interface, we have compared Raman spectra of as-prepared and annealed graphene. The observed shift in Raman features can be attributed to the strain in graphene, caused during annealing. The change in morphology of pentacene on annealed graphene is likely to be driven by depletion of water layer and higher degree of conformation of graphene to the SiO_2 substrate. Compellingly, similar three-dimensional morphology has been observed on graphene transferred onto SiO_2 that was treated with hexamethyldisilazane. Height of the islands was found to be 25 nm. We have also examined the morphology of pentacene on multilayer graphene. Our AFM results show that multilayer graphene reflects almost no contribution from HMDS and 2D growth is observed. In this case, the observed height of 2D islands is 1.5 nm. The observed difference in pentacene morphology can be attributed to the change in surface energy of graphene due to interfacial layers.

Keywords

organic semiconductors, thin films, pentacene, graphene, organic molecular beam deposition, atomic force microscopy, nucleation

Povzetek

Preučili smo rast tankih plasti pentacena na grafenu z uporabo mikroskopa na atomsko silo (Atomic Force Microscopy-AFM). Grafen, pripravljen po dveh različnih metodah, smo uporabili kot substrat za rast pentacena. Grafen smo pripravili z metodo kemičnega naparjevanja (Chemical Vapour Deposition-CVD) in z mikro-mehansko eksfoliacijo s KISH grafita. Prvi del naših raziskav se osredotoča na rast pentacena na enoslojnem grafenu, pripravljenim s CVD metodo. Za prenos grafena z bakrene folije na SiO_2 podlago debeline 300 nm s polimetil metakrilatom (PMMA) kot podlago smo uporabili mokro-kemijsko tehniko. Za očiščenje PMMA s površine grafena smo uporabili ekstenzivno segrevanje v H_2/Ar atmosferi. Pred nanosom pentacena smo morfologijo prenesenega grafena preverili z AFM. Z analizo površine smo opazili, da so na grafenovi plasti prisotni zgibi. Zgibi na grafenovih plasteh so pogosto prisotni tudi po prenosu plasti na substrate. Tipična višina zgibov sega od 1 nm do 6 nm. Opažamo, da imajo zgibi ključno vlogo pri določanju morfologije pentacenovih plasti na grafenu. Naša AFM preiskava začetnih faz rasti vakuumsko-naparjenega pentacena na CVD grafenu je pokazala, da je rast v primeru enoplastne pokritosti s pentacenom tridimenzionalna. Poleg tega je bilo ugotovljeno, da se na območju zgibov pojavljajo otoki pentacena. Z naraščajočo debelino pentacena otoki pridobivajo podolgovato obliko, ki je verjetno posledica kompenzacije elastične deformacije, ki izhaja iz neusklajenosti kristalne mreže. Analiza z mikroskopijo na kelvinovo silo (Kelvin Force Microscopy-KFM) je razkrila, da imajo področja z zgibi bistveno drugačen kontakten potencial kot področja brez zgibov. Preferenčna nukleacija pentacena na zgibih je zato verjetno posledica povečane kemične reaktivnosti zgibov.

V drugem delu raziskovalnega dela smo se osredotočili na nanos sub-enoslojnega pentacena na grafen, pripravljen z mikromehansko eksfoliacijo grafita. Analizirali smo morfologijo sub-enoslojnih plasti pentacena, nanešenih na listasti enoslojni in dvoslojni grafen, prenesenih na SiO_2. Opažamo dvodimenzionalno (2D) rast otokov v območju temperatur podlage (od 10 °C do 60 °C). Višina pentacenovih otokov je 1.5 nm, kar ustreza fazi tankih filmov. Za temperaturo substrata < 40 °C , je velikost otokov bistveno manjša od velikosti sistema. Ugotovili smo, da je porazdelitev velikosti otokov na enoslojnem grafenu širša in osredotočena na višja povprečna območja otokov kot na dvoslojnem grafenu. Vendar pa so pri temperaturi podlage 50

°C in 60 °C otoki povečani zaradi hitrega zraščanja. Otoki v tem režimu ustrezajo režimu prekolacije. Ugotovili smo aktivacijsko energijo agregacije molekul, ki znaša E_a= 427±25 meV za enoslojni grafen in E_a= 537±46 meV za dvoslojni grafen. Sklepamo, da obstaja povezava med ugotovljenimi razlikami v morfologiji pentacenovega sloja z vplivom področja dipola, ki je lahko povezano z vodno plastjo na stiku grafen/SiO_2.

V nadaljnjem delu smo analizirali zgodnje faze rasti pentacena z različno prekritostjo na enoslojnem grafenu pripravljenim z mehanično eksfoliacijo. Preučili smo porazdelitev velikosti otokov pentacena za prekritost v območju $0,07<\theta<0,40$ pri temperaturi substrata Ts = 29 °C. Opazili smo, da širina porazdelitve velikosti otokov narašča s prekritostjo ter, da se središče premakne proti večji velikosti otoka. Nasprotno pa rast pentacena na grafenovih lističih, pripravljenih s tri urnim gretjem v peči pri 350 °C, poteka v tridimenzionalnem (3D) načinu. Višina 3D otokov je 25 nm na temperaturno obdelanih vzorcih plasti grafena. Z namenom boljšega razumevanja vloge stika SiO_2/grafen, smo primerjali Raman spektre prvotno pripravljenega in temperaturno obdelanega grafena. Opazili smo premik v Ramanovih spektralnih karakteristikah, kar je mogoče pripisati deformacijam v grafenu nastalim med gretjem. Do spremembe morfologije pentacena na temperaturno obdelanem grafenu verjetno pride zaradi zmanjšanja vodne plasti in višje stopnje konformacije grafena na SiO_2 podlagi. Podobno tridimenzionalno morfologijo smo opazili na grafenu prenesenem na SiO_2, ki je bil obdelan s heksametildisilazanom. Višina otokov je bila 25 nm. Pregledali smo tudi morfologijo pentacena na večplastnem grafenu. Z AFM analizo nismo opazili vpliva HMDS in 2D rasti na večplastni grafen. V tem primeru je bila višina 2D otokov 1.5 nm. Opažene razlike morfologije pentacena lahko pripišemo spremembi površinske energije grafena zaradi medploskovnih plasti.

Ključne besede

organski polprevodniki, tanke plasti, pentacen, grafen, epitaksija z molekularnimi curki, mikroskopija na atomsko silo, nukleacija

Contents

1 Introduction **1**

2 Experimental methods **5**

2.1 Organic molecular beam deposition 5

2.2 Atomic force microscopy 12

2.3 Electric force microscopy 19

2.4 Kelvin force microscopy 20

2.5 Raman spectroscopy 22

2.6 Materials 25

2.6.1 Graphene 25

2.6.2 CVD graphene 28

2.6.3 Exfoliated graphene 31

2.6.4 Epitaxial growth of graphene on SiC 34

2.6.5 Reduction from graphene oxide 35

2.6.6 Pentacene 36

3 Theory **39**

3.1 Nucleation and growth of thin layers 39

3.2 Dynamic scaling theory 41

3.3 Rate equation theory 43

3.4 Review on pentacene growth 50

4 Grafold -driven nucleation of pentacene on graphene **56**

4.1 Introduction 56

4.2 Results and Discussion 57

4.3 Conclusion 72

5 Pentacene on graphene: differences between single layer and bilayer 73
5.1 Introduction 73
5.2 Experimental 75
5.3 Results and discussion 77
5.4 Conclusion 94

6 Effect of heating on morphology of pentacene on graphene 95
6.1 Introduction 95
6.2 Experimental 96
6.3 Results and Discussion 96
6.4 Conclusion 109

7 Conclusions 110

Bibliography 112

1 Introduction

Graphene has attracted considerable attention due to its interesting electronic, thermal, mechanical and optical properties that can lead to new applications [1-3]. Most frequently graphene-based electronic and optoelectronic devices require some form of integration of graphene with organic semiconductors (OSs). This integration is typically achieved by thin layers of OSs [4]. To develop the full potential of graphene-based devices, thin-film growth process of organic molecules on graphene needs to be understood at a fundamental level. Adsorption of organic molecules on graphene shows two important characteristics. Firstly, well-ordered organic layers on graphene can be formed. And secondly, charge transfer between adsorbed molecules and graphene can modify the electronic properties of graphene [5]. The morphology of the first few layers of organic molecules is crucial as all the charge transport is confined to the first two or three organic layers [6].

This has motivated us to embark on a systematic study of the initial stages of growth of organic molecules on graphene. Recently, organic molecules such as perylene-3,4,9,10-tetracarboxylic dianhydride (PTCDA), tetracyanoquinodimethane (TCNQ), phthalocyanine (Pc), tetracyanoethylene (TCNE), 1,3,5-triazine and pentacene on graphene has been studied [5, 7]. It was observed that each of these molecules have different adsorption orientations on graphene that is transferred on different substrates [5, 8]. One of the frequently used OSs in organic devices is pentacene – a small molecule that exhibits high-charge-carrier mobility. Pentacene can be readily synthesized in ultrathin layers that exhibit – depending on the layer thickness and growth temperature – one or two polymorphs – thin-film phase and bulk phase [9, 10]. P-type field-effect mobility of pentacene devices exceeds 3.0 cm^2/Vs.

The electronic and optical properties of OS thin layers are determined by their structure and morphology. Preparation of organic layers depends on the type of organic molecules. One of the ubiquitous techniques to facilitate high ordered OS layers is organic molecular beam deposition that has emerged in mid-1980s [11]. This technique has an advantage of providing a precise control of layer thickness and provides high purity environment for layer growth. Well-ordered and smooth layers of

high-purity can be grown with this technique. In this process, a beam of molecules impinges on the surface of the substrate, which is maintained at an elevated temperature in high vacuum chamber. Molecules react with each other and with the substrate to form ordered layers. Growth process can be controlled with a relatively slow deposition rate (~ 1 monolayer/s). The prime factor that influences the process of organisation of molecules is the surface diffusion. The diffusion of molecules on the surface of the substrate allows them to accumulate at the adsorption sites of the substrate. These sites lead to the morphology of the layers that depends on the physical and/or chemical properties of the substrate surface.

A detailed understanding of the growth dynamic of pentacene requires examinations of the molecule dynamics during the initial stages of growth (the submonolayer growth regime). Pentacene growth has been studied so far by many groups on dielectric SiO_2 substrates (pure SiO_2, modified SiO_2 and Si substrates) [12-14]. Their study was further extended on organic and polymeric substrates, which are of special interest for organic optoelectronic devices. Surprisingly few reports on the growth of the pentacene graphene have been published todate [5, 15].

Several methods have been developed to synthesize graphene to use, by mechanical exfoliation, chemical vapor deposition and epitaxial growth of graphene by thermal decomposition of SiC [3, 16, 17]. We have elected single layer graphene (SLG) synthesized by chemical vapor deposition method and by exfoliation from KISH graphite. CVD-grown graphene is very promising due to the possibility of fabrication of large area continuous sheet which are of great importance for future electronic devices [18]. Recently, Kobayashi et al. [19] have synthesized 100 m long and 230 mm wide graphene sheet by the CVD method. On the other hand, exfoliated flakes are used due to their high purity and high structural quality. There have been few reports of pentacene on Highly Ordered Pyrolytic Graphite (HOPG) and graphene, which indicate less ordered growth than the dielectric substrates [7, 20]. All have addressed relatively thick layers of pentacene. No research on initial stages of growth of pentacene on graphene has been reported yet. Therefore, we have focused our study on the growth of the submonolayer of pentacene on graphene.

The growth of organic semiconductors is governed by the surface properties of the graphene. The interaction between organic molecules and substrate plays a crucial role in determining the structure of the first monolayer of organic molecules. And,

morphology of the first monolayer determines the morphology of the subsequent grown layers.

This thesis is organised into seven chapters. After the Introduction, the second Chapter introduces different experimental techniques used in the characterization of the samples. Submonolayers of pentacene were deposited on graphene by OMBD in high vacuum chamber. AFM was the prime technique to study the morphology of deposited pentacene on graphene. The morphological study was performed in non-contact mode for all the experiments. In this Chapter, we have described the basic properties of materials used in the study as graphene and pentacene. Graphene preparation by different methods is described in detail. We have used graphene synthesized from two different methods: 1) exfoliation of graphite and 2) graphene grown by CVD technique and transferring to the desired substrates. Major experiments on surface study were done at Laboratory of Organic Matter Physics, University of Nova Gorica, Slovenia. A part of electrical measurements was performed at Applied Physics and Engineering (APE) Research, LDP Trieste. Raman measurements were done at the Institute of Physics, Belgrade, Serbia.

The third Chapter describes the basic phenomena of the growth process of organic molecules on the substrates and the model to describe the growth. Smoluchowski kinetic equations for evolution of island size distribution and their corresponding rate equations are described for atom density and island density. In addition, we discuss the scaling theory for island size distribution and define the relevant exponents that characterize the scaling behaviour of atom density, island density and island size distribution as a function of coverage. Later in the Chapter, a detailed literature review of the growth of pentacene on metal, inorganic and organic substrates is discussed.

The fourth Chapter is dedicated to the detailed analysis of the growth of submonolayers of pentacene on CVD-graphene. The procedure to transfer graphene from Cu foil to SiO_2 is described in detail. Two different submonolayer coverages of pentacene were studied, and the results have been recently published in Ref. [21]. Height distribution for both coverages has been studied. Kelvin force microscopy study was performed to examine the contact potential of folds in graphene (grafolds) with respect to unfolded graphene regions [18]. In addition, contact angle measurements on graphene, graphite and SiO_2 were performed to extract the surface energy of these substrates.

The fifth Chapter focusses on the initial stages of growth of pentacene on exfoliated graphene. The effect of substrate temperature on the pentacene morphology was studied. Morphology of pentacene islands grown in the temperature range from 10 °C to 60 °C was studied systematically on single layer graphene and bilayer graphene (BLG). A comparative statistical analysis of islands on SLG and BLG is presented. Also, fractal dimensions of pentacene islands in this temperature range were obtained for both the SLG and BLG. The results have been published in Ref. [22].

In the sixth Chapter, we present the studies of the effect of water layer at SiO_2/graphene interface on pentacene morphology. The measurements were performed on exfoliated flakes. Raman spectrum was recorded for as-prepared and annealed graphene samples. Firstly, the morphology of islands on graphene before annealing was investigated at different pentacene coverages. Subsequently, growth of pentacene on as exfoliated and annealed graphene samples was studied. The effect of the substrate treatment on the pentacene morphology was studied. Thirdly, pentacene growth on single layer graphene and multilayer graphene transferred onto SiO_2 treated with hexamethyldisilazane (HMDS) was examined.

In the last chapter, we have summarized the results of our research.

2 Experimental methods

2.1 Organic molecular beam deposition

Organic molecular beam deposition (OMBD) is a well-known technique to deposit the thin layers of organic material [23]. Monolayers of organic molecules can be grown with relatively low deposition rate (~1 monolayer/min) allowing one to achieve controlled growth on molecular scale. Layers grown in OMBD are of high structure precision. In OMBD, deposition of thin layers takes place in a vacuum chamber with base pressure ranging from 10^{-5} to 10^{-9} Pa. A schematic of the OMBD chamber is shown in Fig. 2.1. A mechanical shutter is used to turn on or off the beam of molecules. The flux of the incoming molecules arriving on the substrate surface is controlled by the temperature of the effusion cell as well as with the shutter. The beam of molecules from the effusion cell strikes the substrate which is held at a desired temperature. The substrate is held perpendicular to the beam at a distance that allows for uniform flux of the impinging molecules. A quartz crystal monitor is used to measure the thickness of the depositing material. A vacuum chamber may contain several effusion cells that are used to deposit different materials and/or to make alternate layers of different organic materials.

The background pressure should be low enough to avoid contamination from entering into the high vacuum chamber (~ 10^{-9} Pa). The mean-free path of the molecules (average distance travelled by the molecules between successive collisions) at low pressure should be greater than the distance from the outlet of the effusion cell to the surface of the substrate. According to the kinetic theory of an ideal gas, the mean-free path (L) of the molecules can be described using the following equation [24]:

$$L = \frac{1}{\sqrt{2}\pi n_c d^2} \tag{2.1}$$

n_c = concentration of the molecules, d = diameter of the molecules.

The concentration of the gas molecules is related to pressure p and temperature T by the equation:

$$n_c = \frac{p}{K_B T} \tag{2.2}$$

where K_B is Boltzmann constant.

The average velocity of the molecules can be described as

$$\upsilon = \sqrt{\frac{3\ K_B T_s}{m}} \tag{2.3}$$

where m is the mass of the molecules and T_s is the substrate temperature.

The flux of the molecules (F) is defined by the number of molecules impinging on unit area of the surface per unit time. The substrate temperature (T_s) is usually lower than source cell temperature (T_i). Reevaporation can occur if the molecules have sufficient energy at a given site to overcome the attractive surface forces.

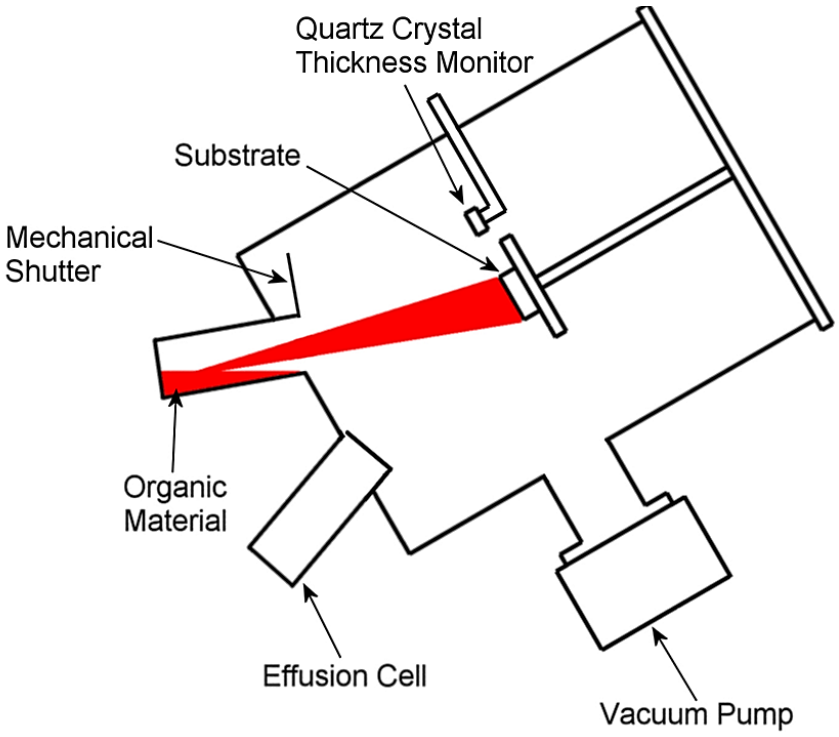

Fig. 2.1: A schematic representation of organic molecular beam deposition chamber (OMBD)

The type of interactions that take place between incoming molecules and the substrate depend on the energy of the molecules. The incoming molecules on the substrate exchange energy with the atoms or molecules of the substrate until they are in thermodynamic equilibrium. The sticking coefficient (s_0) of the molecules is defined

as the ratio of the number of molecules attached to the substrate (N_{att}) to the molecules reaching to the surface (N_{tot}):

$$s_0 = \frac{N_{att}}{N_{tot}} \tag{2.4}$$

Practically, the sticking coefficient is less than one. There is a finite probability that impinged molecules reevaporate if there is no condensation of the molecules. During the condensation, the molecules stay on the substrate for sufficiently long time to adsorb there or to form chemical bonding.

The fundamental processes that occurs during the film growth when organic molecules arrive on the substrate surface are shown in Fig. 2.2 and are a) adsorption of molecules impinging on the substrate surface, b) diffusion of molecules on the surface, c) formation of an island when critical number of molecules meet (an island is a cluster of immobile monomers), d) growth or expansion of islands by new incoming molecules and e) desorption of the adsorbed molecules that were not incorporated into the crystal lattice [23]. The adsorption of molecules on the surface of the substrate can occur in two forms depending on the type of forces between molecules and substrate: 1) physical adsorption and 2) chemical adsorption. In physical adsorption, there is no charge transfer between molecules (adsorbate) and substrate (adsorbent) and the force of attraction between adsorbate and adsorbent is of the van-der Waals-type.

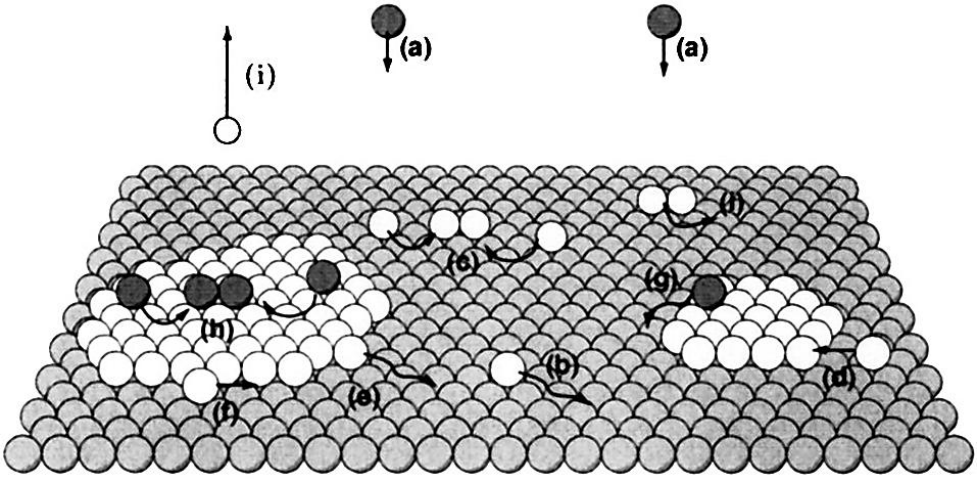

Fig. 2.2: Schematic illustration of atomistic processes involved in layer formation. An atom approaching the surface (a) can adsorb on the surface, becoming an adatom and (b) undergo surface diffusion. (c) adatoms can meet to form dimers, (d) incorporate into existing islands, (e) detach from them or (f) even diffuse along the island edge. (g, h) deposition of adatoms on top of islands and corresponding processes are to be considered as well. (i) desorption of some of the adatoms also takes place. Figure is taken from Ref. [25].

On the other hand, in chemical adsorption, there occurs charge transfer to form chemical bonding between the adsorbent and the adsorbate. In this case, the adsorption energy of the molecules is much higher than (~ few eV/atom) that of physical adsorption (~100 meV/atom).

The key parameters which determine the quality of the grown layers by OMBD are:

1) substrate temperature
2) deposition rate
3) type of molecule − substrate interaction
4) purity of the source material
5) substrate

At low substrate temperature, there is a high probability that impurities adsorb on the substrate. A typical range of substrate temperature to grow thin organic layers is from 80 K to 400 K. On the other hand, higher substrate temperature allows the molecule to diffuse on the substrate surface and find an energetically favorable lattice site to form islands. Deposition rate has similar effect to that substrate temperature. At low deposition rate, impurities tend to adsorb on the substrate at a higher rate than the organic molecules. On the contrary, it is difficult to control the growth of layers at high deposition rate. Typical growth rate to grow thin layers ranges from 0.1 to 5 Å/s. The purity of the material and the density of defects on the surface of the substrate also play a crucial role in the quality of the grown layers [11]. The purification of the source material is essential to avoid the contamination in high vacuum chamber which can result in high background pressure. Therefore, the deposition rate of the layers should be higher than the incorporation rate of impurities.

2.1.1 Growth modes of thin layers

Depending on the type of molecule − substrate interactions, layers deposited on the substrates exhibit three characteristics modes of growth as:

a) Frank-van-der-Merve growth mode (layer-by-layer growth)
b) Volmer-Weber growth mode (island growth)
c) Stranski-Krastanov growth mode (layer-plus-island growth)

The thermodynamic driving force of nucleation process is supersaturation, i.e. the difference $\Delta\mu$ between the chemical potential of the vapour phase μ_v, and the

chemical potential of the infinitely large organic crystal μ_c of the same material [26]. The nucleation mode is determined by $\Delta\mu$, and by the difference of cohesion and adhesion energies $\Delta\sigma = \sigma + \sigma_i - \sigma_s$, with σ, σ_i and σ_s, as surface energies of the island, the substrate –island interface and the substrate, respectively. A 2D growth mode is referred as layer-by-layer growth mode and 3D growth mode corresponds to island growth mode. When $\Delta\sigma < 0$, i.e. when molecule − substrate interaction exceeds inter-

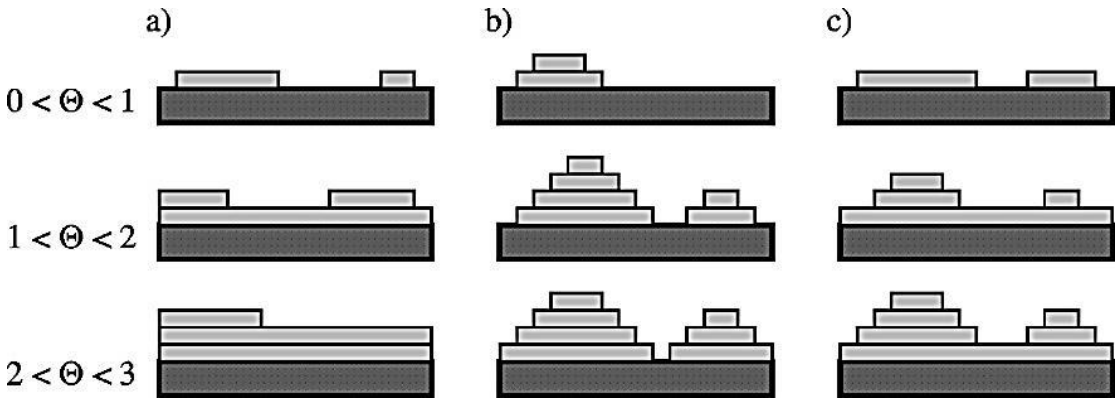

Fig. 2.3: Growth modes for thin layers. a) shows layer–by-layer growth mode with submonolayer coverage to multilayer coverage. b) represents island growth and c) represents layer plus island growth [Figure from: www.physik.uw.kl.de).

-molecular interactions, a 2D nucleation is preferred. This growth mode is called as Frank-van-der-Merve growth mode or layer-by-layer growth mode as shown in Fig. 2.3a. On the other hand, if intermolecular interaction is stronger than the molecule – substrate interaction $\Delta\sigma > 0$, a 3D nucleation or Vollmer-Weber growth mode occurs (Fig. 2.3b).

Stranski-Krastanov growth mode occurs, when thickness of a layer exceeds a critical thickness, 3D islands start to nucleate due to relaxation from strain during thin film growth (Fig. 2.3c). This kind of growth occurs when a large lattice mismatch i.e. 3% – 7% is present. In both, layer-by-layer and layer-plus-island growth mode first monolayer is formed via nucleation of 2D islands.

The areal density of islands (number of islands per unit area (N)) for all growth modes depends on the deposition rate and the substrate temperature. Several physical models have been proposed to describe the island growth of the organic layers [13, 27, 28]. The dependence of N on the deposition rate (R) and substrate temperature (T_s) is expressed as:

$$N = R^{\delta} exp^{\left(\frac{E_N}{K_B T_s}\right)} \quad (2.5)$$

where δ is the critical nucleus size, K_B is the Boltzmann constant and E_N is the activation energy for nucleation and is defined as:

$$E_N = \frac{(E_i + iE_d)}{(i+2)} \quad (2.6)$$

E_d is the activation energy of diffusion, i is the number of molecules forming a stable island. E_i is the difference in surface energy between i adsorbed molecules on substrate and i molecules in a stable island. E_N and value of δ depends on critical nucleus size and their dimensions.

2.1.2 Issues related to organic thin layer growth

1) Organic molecules being extended objects have internal degree of freedom (vibrational, orientational and conformational) [29, 30] and this is a fundamental difference between the growth of thin layers of organic and inorganic materials (Fig. 2.4). There are several issues with organic molecules which can lead to different growth behaviour.
   a) Orientational degree of freedom: it forms tilt domains which results in lying-down and standing-up orientation of molecules as shown in Fig. 2.4a. Even if there is no transition during the growth, difference of 'lying-down' and 'standing-up' layers is important and is possible only for molecular systems. Conventional growth models for atoms do not take this into account.
   b) Vibrational degree of freedom: interaction of molecules with the substrate can be influenced by their vibrational degree of freedom. The reason is that translational energy of molecules can be converted to internal vibrational energy, which can further affect the thermalization process upon adsorption of molecules.
   c) Conformational degree of freedom: This is related to the fact that building blocks within the layers can change to accommodate the stress released from lattice mismatch.

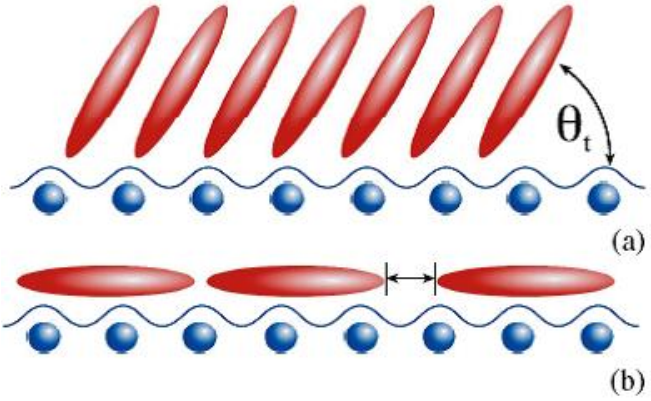

Fig. 2.4: a) Orientational degree of freedom, b) translational degree of freedom. Figure is taken from Ref. [29].

2) Intermolecular interaction and molecule – substrate interactions are dominated by weak van-der Waals interaction. Interaction energy per atom for an organic molecule is lower than atomic adsorbates. However, when weak interaction energies are summed up after integrating over all the atoms within a molecule, they lead to substantial molecular binding energy in eV range. Weak interaction causes high thermal expansion coefficient (~ 10^{-4} K^{-1}) which leads to high thermally-induced strain at the layer – substrate interface.

The OMBD used in our laboratory comprised of two vacuum chambers, an introduction chamber and a main chamber that is equipped with two temperature controlled effusion cells and a quartz crystal thickness monitor (Fig. 2.5). These chambers are separated by a gate valve and connected to a rotary pump and a turbo pump. Substrates are mounted on a sample holder which is connected to a manipulator. The distance between a substrate and outlet of the effusion cell is ~10 cm. The sample holder allows for heating and cooling of the sample in the temperature range from -20 °C to 150 °C with the precision of ± 0.5 °C.

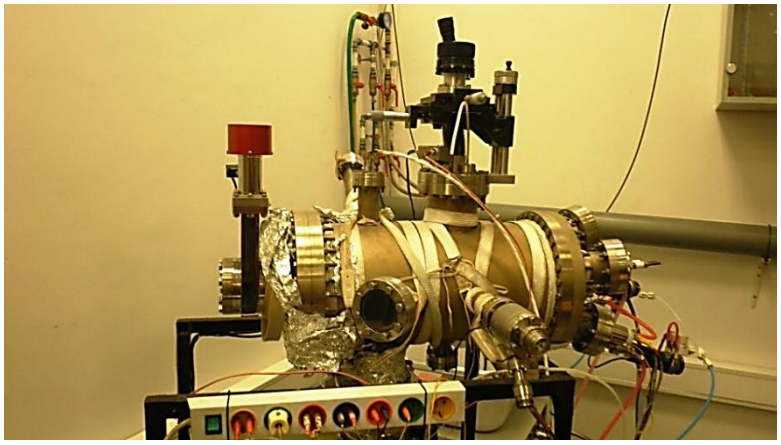

Fig. 2.5: OMBD chamber used for pentacene evaporation

2.2 Atomic force microscope

Atomic force microscopy is a tool to characterize the surface of samples with a lateral resolution of 0.1 nm. AFM was introduced by Gerd Binning and Heinrich Rohrer in early 1980 which earned them Nobel Prize for Physics in 1986. It is used to investigate a variety of different organic and inorganic materials. It can operate in ambient as well as in liquid atmosphere, making it possible to examine biological macromolecules and living organisms in fluid cells. In AFM, a sharp tip is attached to one end of the cantilever that is 100-200 µm in length. The tip is brought in close contact with the surface of the sample (Fig. 2.6). The sample is mounted on a piezoelectric crystal which can move the sample in two lateral directions for scanning and in a vertical direction. A schematic of an AFM is shown in Fig. 2.6.

Forces that act between the tip and the sample lead to a deflection in cantilever according to Hooke's law:

$$F = -\text{ƙ}\Delta x \tag{2.7}$$

where ƙ is spring constant of the cantilever and Δx is the deflection in the cantilever. In order to detect this deflection, a laser spot is focused on the back of the cantilever and is reflected into a four-segment photodiode. The position of the reflected spot changes with the deflection in the cantilever. A photodetector converts this change in an electrical signal. Subsequently, the map of the topography of sample is generated and processed using imaging software. Typical spring constants of the cantilever used in AFM are in the range from 0.1 – 1 N/m.

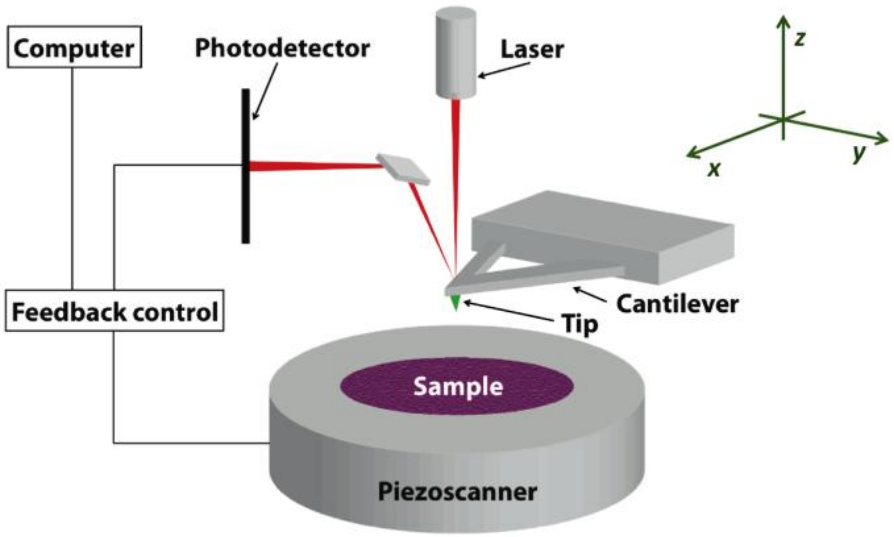

Fig. 2.6: A Schematic of Atomic Force Microscope. Figure from: amyhallr.wordpress.com.

In AFM, the distance controlled during the measurement is not the actual tip – sample distance (D). It is the distance Z between the surface of the sample and the rest position of the cantilever as shown in the Fig. 2.7. These two distances differ because of cantilever deflection (δ_c) and sample deformation (δ_s) and are related as:

$$D = Z - (\delta_c + \delta_s) \tag{2.8}$$

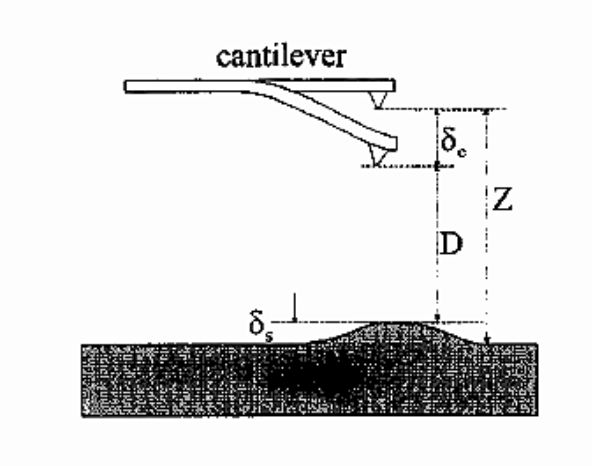

Fig. 2.7: The tip – sample interaction system. D is the actual the distance between the tip and the sample. Z is the distance between the sample and the rest position of the cantilever. Figure is taken from Ref. [31].

Hence, force – distance curve is a result of two contributions: the tip – sample interaction and the elastic force of the cantilever. Since cantilever deflections and deformations in the sample are not known in advance, only distance is the Z distance that can be controlled.

This force can be attractive or repulsive depending on the distance between the tip and the sample. At large distance between tip and sample, the force is attractive and is repulsive for short distances, as can be seen in the force – distance curve (Fig. 2.8). Force – distance curve is a plot of tip – sample interaction forces versus tip – sample distance. At each distance, the cantilever deflects until its elastic force balances the tip-sample interaction force so that the system is in equilibrium. When the tip is far away from the surface, a deflection in cantilever is constant with respect to the sample displacement. When the gradient of attractive force becomes larger than the spring constant, equilibrium is lost and the tip jumps onto the surface.

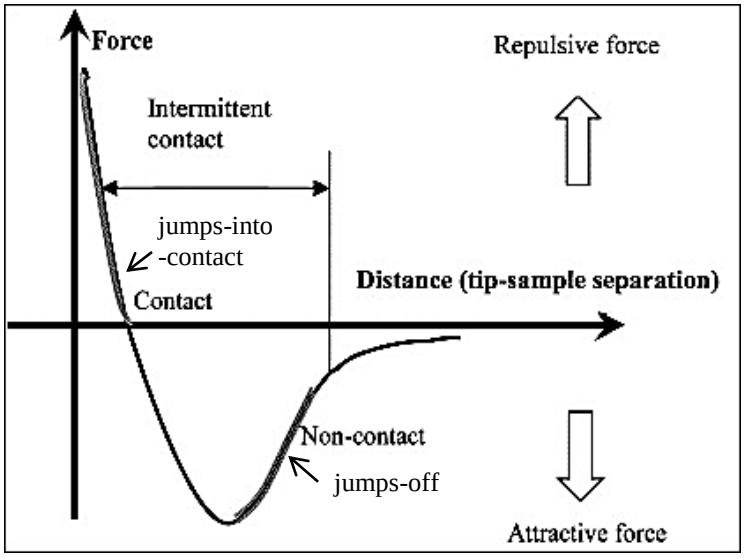

Fig. 2.8: Force distance curve between AFM tip and sample. Figure from: invsee.asu.edu/nmodule/spmmode/afm.html.

When the tip is brought into contact with the surface of the sample, decreasing the sample displacement results in a linear curve according to equation 2.7. Adhesion between the tip and the sample surface generates an hysteresis in the force versus distance curve. When a negative normal force is exerted by the cantilever, the tip jumps-off out of contact. The most interesting regions of the force – distance curves are two non-contact regions containing the tip jumps-into the contact and jumps-off the contact and are indicated in the Fig. 2.8. The non-contact region in the approach curves gives information about the attractive and repulsive forces before contact. During imaging under ambient conditions, adhesion mainly occurs from capillary forces between the tip and a water layer that forms on the surface of the sample.

2.2.1 Modes of Operation

AFM can be operated in three modes depending on the application

1) Non-contact mode

In this mode, the tip does not make any contact with the surface of the sample, but the cantilever is oscillated with a resonant frequency, and a typical amplitude of oscillation <10 nm. Distance between the tip and the sample surface is ~5-10 nm, but it also depends on the surface of the sample. Long-range van-der Waals forces between the tip and the sample are detected by the oscillating tip which is excited

with resonant frequency. Force between the tip and the sample is of the order of (~ 10^{-12} N). The advantage of this mode is that it does not destroy the surface of the sample, and is thus suitable for organic thin layers and biological samples. Therefore, we have used AFM in non-contact mode for this thesis. The spring constant of the cantilever is ~20-100 N/m.

2) **Contact mode**

The tip is brought in close contact with the surface of the sample and the distance between the tip and the sample is few Å. The interatomic force between the tip and the sample is repulsive. There are two types of contact mode, constant-force and constant-height mode. In constant-height mode, deflection is measured directly and deflection force is used to calculate the distance between the tip and the sample. In constant force mode, the force between the tip and the surface is kept constant and a constant deflection is maintained during scanning. A feedback loop is required to move the sample or the tip position. AFM images are taken in constant force mode. Cantilever has a spring constant of < 1 N/m. A high resolution image can be obtained with this mode. On the other hand, tip can damage the sample surface if the surface is soft.

3) **Tapping mode**

This mode allows high-resolution imaging of sample surfaces, which can be easily damaged or loosely bound to the substrate. In this mode, cantilever is oscillated close to the resonant frequency similar to non-contact mode. But the amplitude of oscillation is > 10 nm (100-200 nm). The tip is close enough to the surface of the sample to detect short-range forces, avoiding the damage to the sample surface due to dragging across surface. Forces acting between the tip and the sample cause change in the oscillation amplitude as well as in the resonant frequency. An electronic feedback loop is required to keep the amplitude of oscillation constant. This mode is also called as intermittent contact mode. In this mode, a lateral resolution (1-5 nm) higher than contact mode can be obtained.

2.2.2 Applications of AFM

Since its invention, a number of applications have emerged, such as

1) **Roughness analysis:** The obtained topography of the AFM image corresponds to the measured height values $z(x, y)$. Each height value is associated with a pair of

surface coordinates (x, y). An AFM image is described by a matrix with M rows and Q columns. $\bar{z}$ is the average height. Data is recorded as line scans along x-axis that link together to form two-dimensional image. AFM is used to study the surface roughness of the sample at nanoscale. The value of surface roughness depends on the scale of the measurement. Surface roughness is quantified by the vertical spacing of the real surface from its ideal form. Therefore, roughness of the surface represents the standard deviation of the surface heights. Surface roughness can be used to estimate the quality of the thin layers. This quantity is denoted as R_{rms} where rms is root mean square value and is expressed as:

$$R_{rms} = \sqrt{\frac{1}{M}\sum_{x=1}^{M}\left(z(x,y) - \bar{z}(M,Q)\right)^2} \tag{2.9}$$

2) **Grain analysis:** grain analysis is performed firstly by masking the grains by a threshold value of either height, slope or curvature. Then the surface area, volume, and height distributions of the grains can be estimated. Surface area of grains can be calculated by first calculating the area that lies inside each pixel. A schematic is shown in Fig. 2.9 to calculate the area of pixel by triangulation method. Let z_j for j = 1, 2, 3, 4 denote the values in four neighbour points (pixel centres), and H_x and H_y denotes the pixel dimensions along the corresponding axes. Four triangles are formed by placing an additional point in the centre of the rectangle (gray color). And area of one triangle can be approximated as:

$$A_{12} = \frac{H_x H_y}{4}\sqrt{1 + \frac{(z_1 - z_2)^2}{H_x} + \frac{(z_1 + z_2 - 2\bar{z})^2}{H_y}} \tag{2.10}$$

Therefore, surface area of one pixel can be calculated by adding the area of all triangles as:

$$A = A_{12} + A_{23} + A_{34} + A_{41} \tag{2.11}$$

By calculating the surface area inside each pixel, area of grains or masked areas can be calculated. Once all the grains in the image are identified using the procedure described above, we have performed a statistical analysis of the data. In addition to the typical quantities such as mean island size, island density and mean island area, we have frequently used probability density distribution and the island size distributions in Chapters 5 and 6. First, data (text file) for area (height)

of pentacene islands is extracted from the AFM micrographs using Gwyddion software [32]. Subsequently, the number of times an island of a given area is present in the micrograph (frequency) was determined from the data and the pertinent histogram was constructed. The height of the bar in histogram represents the number of islands per unit area (height) and area of each bar represents the number of islands in bin. Therefore, probability density represents the fraction of islands per unit area. Throughout this work the area for normalization is the area of the graphene flake, and not the area of the image.

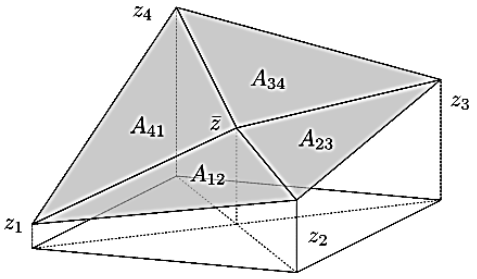

Fig. 2.9: A schematic of surface area calculation. The thick lines symbolize the triangulation. The surface area calculated equals to the area covered by the mask (grey) in this scheme. Figure from: gwyddion.net.

3) Tip – sample force curve for layers to study Young′s modulus of the layer.
4) In addition, several modes of operation are possible such as magnetic force microscopy, lateral force microscopy, electric filed microscopy and Kelvin force microscopy.

2.2.3 Limitations of AFM

The level of information obtained from the morphology of AFM images depends on the size and shape of the tips used for imaging the sample surface. The cantilever of AFM system is typically made of Si or SiN_3 with a tip radius of < 10 nm and typical length of the tip of a few microns. Imaging performed by these tips, which has high cone angle lack the information on deep and narrow features of the sample surface. The morphology represents the interaction of the tip with the surface and is called as tip – sample convolution (Fig. 2.10). Due to the tip – sample convolution, broadening of the profile (features) occurs and is a major AFM artifact. A sharp tip (left hand side image) with a high-aspect ratio represents better surface features and high resolution. On the other hand, a low-aspect ratio tip limits the lateral resolution of the surface (right hand side image of Fig. 2.10). To avoid such problems, there are commercially available tips with high aspect ratio. These tips are made of carbon nanotubes or

tungsten spikes. A spike of carbon material is deposited onto the end of pyramidal of AFM tip.

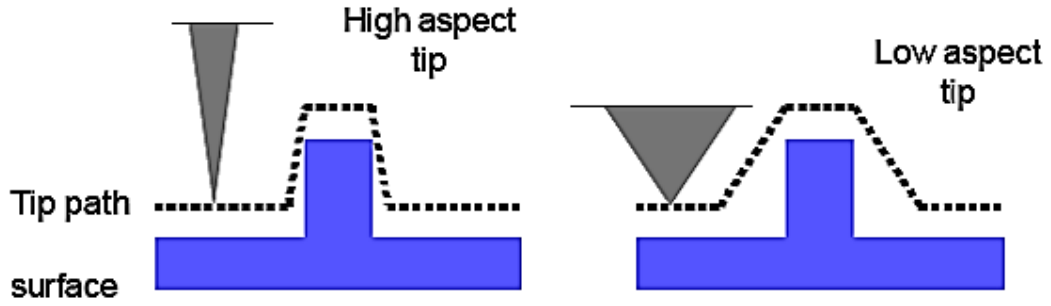

Fig. 2.10: A perfect tip with high aspect ratio scanning over the surface (left image). Right hand side image shows a tip with low aspect ratio resulting in poor lateral resolution. Figure from: asdlib.org.

Fig. 2.11 shows the commercial AFM (Veeco CP-II) for this thesis, with primary components as scanner, electronics modules, Auto-Probe head, optical microscope and photodetector. An Auto-Probe system consists of a probe head, a manual XY-stage, a motorized Z-stage and a scanner. The probe head consists of a deflection sensor comprised of a laser diode, a mirror and a position-sensitive photodetector. This probe head allows us to operate in different AFM modes (contact, noncontact and tapping mode). Different alignments and indicators on this head help in align the deflection sensor before measurements. XY-stage is used to position the tip over the desired position on the sample. Sample is fixed on the sample holder which is attached at the top of scanner. An optical microscope is used to view the tip relative to the sample.

Fig. 2.11: Commercial Veeco CP-II AFM used in our laboratory

2.3 Electric force microscopy

Electric force microscope (EFM) measures the electrostatic force gradient on the sample by measuring the electrostatic force between the sample surface and the biased AFM tip [33]. The tip interacts with the sample through long-range Coulomb forces. These interactions change the amplitude of oscillation and the phase of the AFM cantilever and are detected to create EFM images. Fig. 2.12 shows a schematic representation of EFM measurements. The information on the surface topography and the electrostatic forces are recorded simultaneously. There are two factors which contribute to the EFM signals. One is the capacitance between the tip and the sample, determined by the tip – sample distance, the material and the shape of the sample and the tip. The other is the potential difference between the tip and the sample. The component of the electrostatic force perpendicular to the sample surface between the tip and the conducting material due to the applied bias voltage on the tip can be written as [31]:

$$F_z = \frac{1}{2}\frac{\partial C}{\partial z}(\Delta V)^2 = \frac{1}{2}\frac{\partial C}{\partial z}(V_{tip} - \varphi(x,y))^2 \qquad (2.12)$$

where V_{tip} is the voltage applied to the cantilever and $\varphi(x,y)$ is a z-independent potential distribution on the sample surface. C is the capacitance of the tip – sample system.

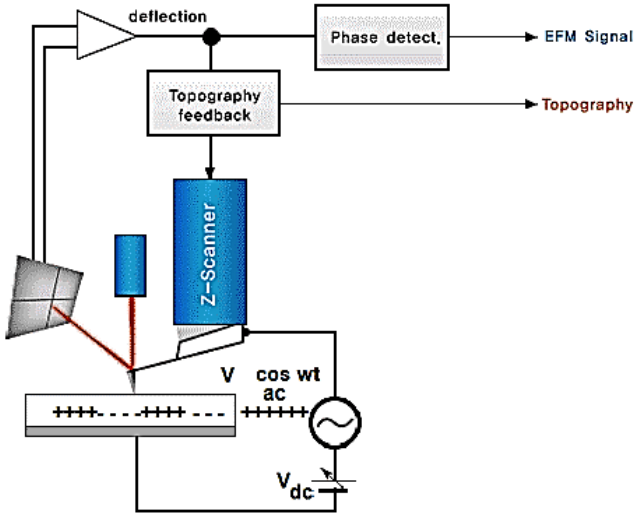

Fig. 2.12: A Schematic diagram of electric force microscope. Figure from: www.parkafm.com

2.4 Kelvin Force Microscope

This technique is based on the measurements on forces rather than force gradients. Kelvin force microscope is used to measure the contact potential difference (V_{CPD}) by measuring the electrostatic force between the tip and the sample surface [34]. Contact potential difference between the tip and the sample is defined as:

$$V_{CPD} = \frac{\phi_t - \phi_s}{(e)} \tag{2.13}$$

where ϕ_t and ϕ_s are the work-functions of the tip and the sample, e is the electronic charge.

Fig. 2.13 represents the electronic energy levels diagram of the tip and the sample. Fig. 2.13a) shows the Fermi energy levels of the sample (E_{fs}) and the tip (E_{ft}), when the tip and the sample are separated by a large distance *d.*

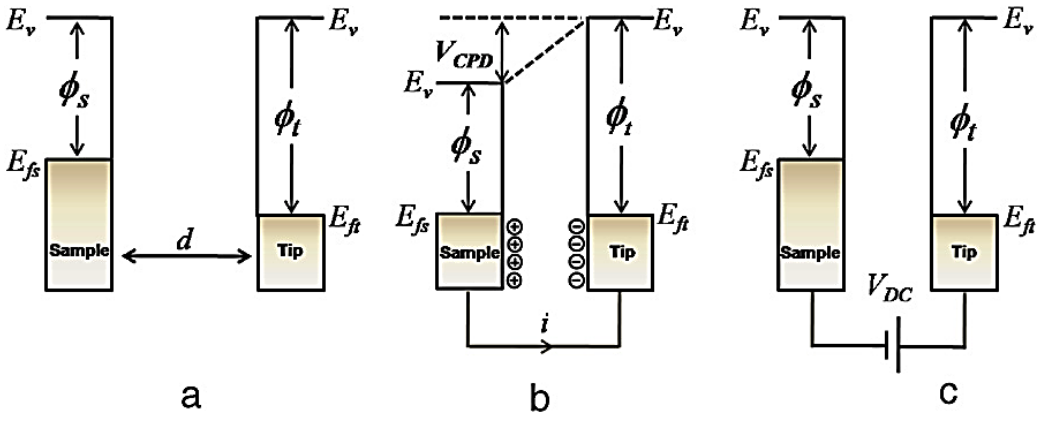

Fig. 2.13: Electronic energy levels of the tip and the sample, a) the tip and the sample are separated by a distance *d* without making any electric contact, b) the tip and the sample are in electric contact, c) A bias V_{DC} is applied between the tip and the sample to compensate the CPD, and hence, the electrical force between tip and sample. $E_{v,}$ E_{ft}, E_{fs} are the vacuum level, Fermi level of the tip and Fermi level of the sample respectively. Figure is taken from Ref. [34].

Fermi levels of the tip and the sample are aligned when the tip and the sample surface becomes close enough to make an electric contact (Fig. 2.13b). Due to difference in work function, charge transfer takes place between the tip and the sample. Equal and opposite charges will be induced on the surfaces of the sample and the tip. Electrical current starts to flow due to electron tunneling. The tip and the surface of the sample will be charged and a local electrostatic potential V_{CPD} is generated between the tip and the sample. Electrostatic energy is stored between the tip and the sample. An

electric force acts on the contact area due to the V_{CPD}. If an external bias V_{DC} (Fig. 2.13c) of the same magnitude as that of V_{CPD} with opposite direction is applied, this force is compensated. The surface charges in the contact area are eliminated by the applied voltage. An applied V_{DC} bias that compensates the electrical force due to the V_{CPD} is equal to the work function difference between the tip and the sample. Hence, the work function of the sample can be calculated if the work function of the tip is known. The electrostatic force between the tip and the sample is expressed by equation 2.12.

In KFM measurements, both an alternating current (ac) and a direct current (dc) bias are applied between the tip and the sample. When $V_{tip} = V_{DC} + V_{AC}\sin(\omega t)$ is applied to the tip, the voltage difference ΔV can be written as:

$$\Delta V = V_{tip} \pm V_{CPD} = (V_{DC} \pm V_{CPD}) + V_{AC}\sin(\omega t) \tag{2.14}$$

V_{DC} is the dc offset potential and V_{AC} and ω are the amplitude and frequency of the applied ac voltage respectively. V_{tip} is the voltage applied to the tip. Frequency of the ac voltage is set to the resonance frequency of the cantilever. Sign "±" depends whether the bias (V_{DC}) is applied to the tip (-) or the sample (+). Using equation (2.14) in (2.12) gives the expression of the electrostatic force applied to the tip as [34]:

$$F_z = -\frac{1}{2}\frac{\partial C}{\partial z}\left[((V_{DC} \pm V_{CPD}) + V_{AC}\sin(\omega t))\right]^2 \tag{2.15}$$

This equation can be separated into three parts:

$$F_{DC} = -\frac{\partial C(z)}{\partial z}\left[\frac{1}{2}(V_{DC} \pm V_{CPD})^2\right] \tag{2.16}$$

$$F_{\omega} = -\frac{1}{2}\frac{\partial C(z)}{\partial z}\left[(V_{DC} \pm V_{CPD})V_{AC}\sin(\omega t)\right] \tag{2.17}$$

$$F_{2\omega} = \frac{\partial C(z)}{\partial z}\frac{1}{4}{V_{AC}}^2[\cos(2\omega t) - 1] \tag{2.18}$$

Force F_{DC} in equation (2.16) is a measure of the static deflection of the tip. $F_{2\omega}$ in equation (2.17) with frequency ω is used to measure the V_{CPD}. The term $F_{2\omega}$ comprised of three terms and yields a nontrivial solution (at ω = 0) in which V_{DC} is equal to the difference in work function between the tip and the sample surface. $F_{2\omega}$is

used for capacitance microscopy. In capacitance microscopy, a change in capacitance between the tip and the sample is measured using high-frequency resonant circuit. Equation (2.15) is valid for measurements of contact potential difference on metallic surfaces.

The difference between EFM and KFM is that EFM directly measures the electrostatic force between the tip and the sample, while KFM uses a compensating technique to determine local surface potential. An ac and dc voltage is applied to modulate the interaction between tip and sample surface to detect the electrostatic signal. As KFM measures the local surface potential, this technique is not restricted to the conductive samples.

2.5 Raman spectroscopy

It is a versatile and non-destructive technique which is used to study the optical and electronic properties of the materials [35]. It is based on the study of the inelastic scattering of incoming photons on atoms or molecules on the sample. In this process, energy is transferred between an incident photon and the sample, resulting in a scattered photon of different energy.

When a photon of a given energy is incident upon the sample (solid, liquid or gaseous), it interacts with molecules or atoms of the sample, and is either reflected, absorbed or scattered. Photons incident on the sample are re-emitted with the same or different frequency. Scattered light is collected by an optical system and is passed to a spectrometer. An energy level diagram for the levels involved in Raman process is shown in Fig. 2.14. When a photon is absorbed by Raman inactive mode, the excited molecule returns back to the original vibrational level and emits light of the same energy as the incident photons. This kind of interaction is called elastic Rayleigh scattering. Raman scattering can be categorized into Stokes-scattering and anti-Stokes scattering. In this process, a photon excites the molecules from the ground state to virtual energy states. After scattering, the energy of the scattered photon increases or decreases relative to the energy of the incident photon. The energy of the photon is decreased if the final vibrational level of the molecule is more energetic than initial state. This shift is called Stokes shift. On the contrary, if the energy of the final vibrational level is lower than the energy of the incoming photon, emitted photon shifts towards the higher energy which is called anti-Stokes shift. These shifts in

energy provide the information about the vibrational and rotational levels of the sample.

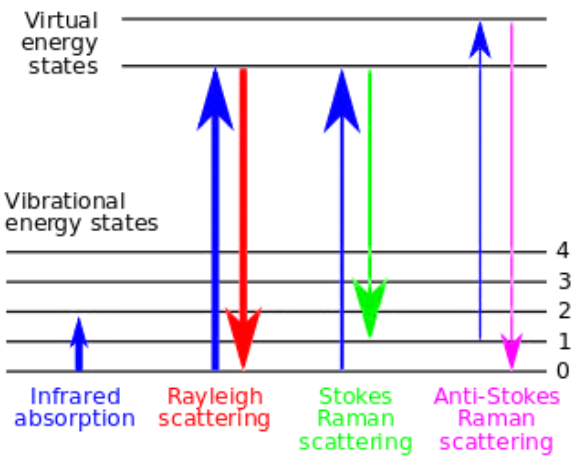

Fig. 2.14: Energy level diagram of the levels involved in Raman scattering. Figure from: en.wikipedia.org/wiki/Raman_spectroscopy.

A Raman spectroscopy experiment gives the eigenfrequencies of the elementary excitation from the analysis of the peak frequencies ω_{sc} in the scattered light. The frequency of the incident light ω_{in} is defined by the laser-light source. Energy conservation implies:

$$\hbar\omega_{sc} = \hbar\omega_{in} \pm \hbar\Omega_g \tag{2.19}$$

where $\hbar\omega_{in}$ is the energy of the incident photon and $\hbar\omega_{sc}$ is the energy of the scattered photon.

$\hbar\Omega_g$ is the eigenenergy of an elementary excitation and corresponds to amount of energy transferred. "-"sign corresponds to Stokes scattering while "+" sign corresponds to anti-Stokes scattering. A plot of intensity of the scattered light versus frequency difference $\Delta\omega = \omega_{in} - \omega_{sc}$ gives peak at the eigen frequencies Ω_j of the elementary excitations (j = 1, 2). Similar to energy conservation, momentum conservation law yields the correlation between the wave vector $\vec{k}_{in}$ of the incident photon, $\vec{k}_{sc}$ of the scattered photon and the excitation wave vector $\vec{q}_j$:

$$\vec{k}_{sc} = \vec{k}_{in} \pm \vec{q}_j \tag{2.20}$$

A schematic of Raman spectrometer is shown in Fig. 2.15 that consists of the following components:

1) Laser (excitation light)
2) Sample illuminating devices and lens, gratings

3) Spectrophotometer or filter for wavelength selection
4) Photodetector

A laser light in ultraviolet, visible or infra-red is used to illuminate the sample. A Raman spectrum recorded for graphene is shown in the bottom part of Fig. 2.15. More than 99% of the incident photons produce elastic Rayleigh scattering. And less than 1% of the photons undergo inelastic Raman scattering which are useful for sample characterization. To reduce the Rayleigh scattering and to enhance the Raman signal, notch filters and laser stop apertures are used. The Raman signals are detected by the photomultiplier tube (PMT) or charge-coupled devices (CCD).

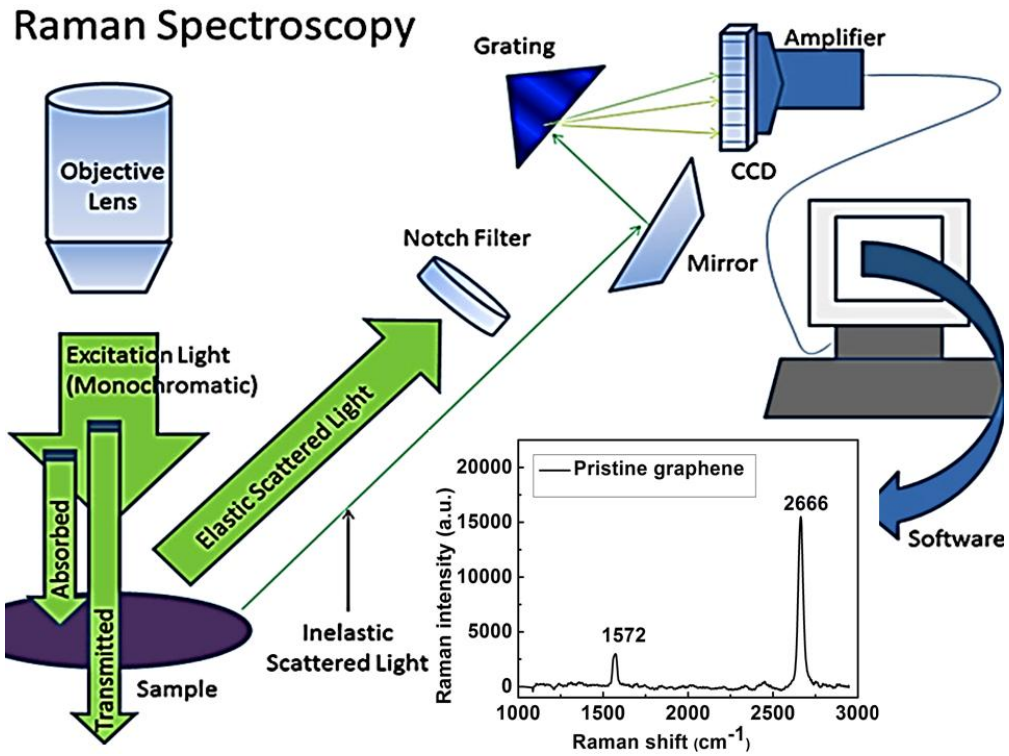

Fig. 2.15: Schematic of a Raman spectrometer. Figure from: www.chem.umd.edu.

Raman spectroscopy has played a crucial role in characterization of carbon-based materials. Especially, after 2004 with the discovery of graphene, it has emerged as a powerful tool for structural characterization of graphene [36]. With this tool, we can observe variation in Raman signal for different graphene layers. It implies that there is change in electronic bands of different graphene layers. In addition to that, it also determines the number of the graphene layers such as single layer, bi-layer and few layers in a stack [37]. Raman spectroscopy can also be used to determine the doping in graphene.

2.6 Materials

2.6.1 Graphene

Graphene was first isolated in 2004 from graphite using adhesive tape by A. K. Geim and and K. S. Novoselov from the University of Manchester [2, 3]. In 2010, they were awarded Nobal prize for their ground-breaking experiments on graphene. Graphene is an atomically thin layer of carbon atoms arranged in a hexagonal network. The carbon-carbon bond length is ~ 0.142 nm. It is a unique material with excellent mechanical, optical and electronic properties.

A stack of graphene layers that are coupled by weak van-der Waals forces form graphite (a 3D allotrope of carbon) as shown in Fig. 2.16. Carbon nanotubes may be interpreted as rolled graphene along a given direction and reconnecting carbon bonds. Fullerenes can be seen as wrapped-up graphene. However, before graphene discovery it was not clear whether 2D crystals can exist in free state [3, 38]. The reason for non-existence of free standing atomic layers was that they become thermodynamically unstable below a certain thickness. Thermal fluctuations lead to the displacement of atoms at any finite temperature. Individual atomic layers can decompose or segregate below a thickness of many dozens layers [39]. Moreover, there were no tools to observe for one atom thick graphite flakes on macroscopic level. Eventually, graphene was detected on SiO_2 due to optical contrast with substrate [40] and will be discussed in detail in Section 2.6.3 of this Chapter. Isolation of graphene from a stack of layers has shown that 2D crystals exhibit high crystalline quality and are thermodynamic stable.

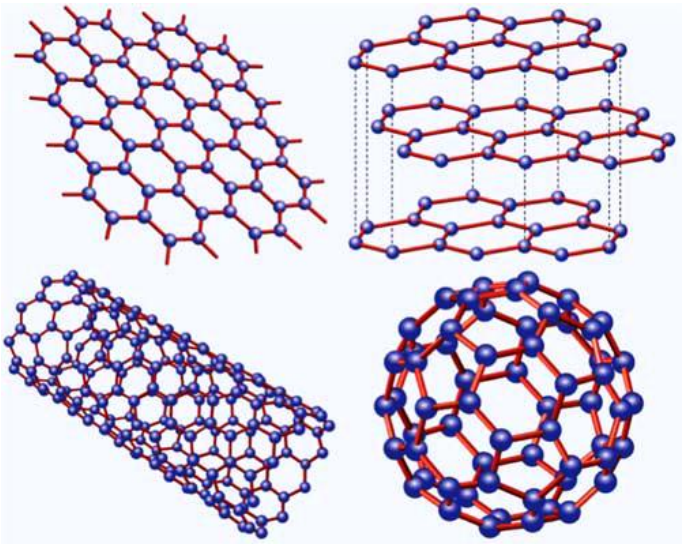

Fig. 2.16: Graphene is a network of carbon atoms arranged in a honeycomb lattice (top left). Graphite (top right) is a stack of graphene layers. Graphene can be rolled up in cylindrical form to make carbon nanotubes (bottom left). Pentagons are introduced on hexagonal lattice to wrap graphene which are viewed as fullernes (C_{60}) (bottom right). Figure is taken from Ref. [2].

2.6.1.1 Properties of graphene

Honeycomb lattice of graphene is composed of two equivalent carbon atoms A and B as shown in Fig. 2.17. Its structure can be seen as triangular lattice with a basis of two atoms per unit cell. The lattice vectors $\vec{a}_1$ and $\vec{a}_2$ can be written as [2]:

$$\vec{a}_1 = \frac{a}{2}(3, \sqrt{3}), \qquad \vec{a}_2 = \frac{a}{2}(3, -\sqrt{3}) \tag{2.21}$$

where a = 1.42 Å is the interatomic distance of carbon atoms. Primitive vectors in reciprocal space are given by,

$$\vec{b}_1 = \frac{2\pi}{3a}(1, \sqrt{3}), \qquad \vec{b}_1 = \frac{2\pi}{3a}(1, -\sqrt{3}) \tag{2.22}$$

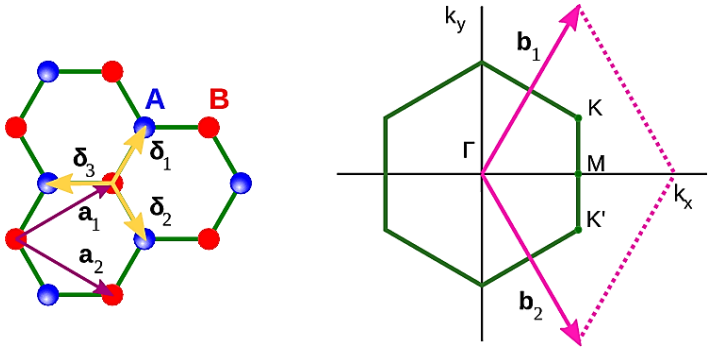

Fig. 2.17: Honeycomb lattice and the first Brillouin zone of graphene. Figure from: oer.physics.manchester.ac.uk.

Of particular importance are the K and K´(Dirac points) at the corner of graphene Brillouin zone (BZ) (Fig. 2.17). Their position in momentum space is given by:

$$K = \left(\frac{2\pi}{3a}, \frac{2\pi}{3\sqrt{3}a}\right), \qquad K' = \left(\frac{2\pi}{3a}, -\frac{2\pi}{3\sqrt{3}a}\right) \tag{2.23}$$

The three nearest–neighbour vectors in real space are written as:

$$\vec{\delta}_1 = \frac{a}{2}(1, \sqrt{3}), \qquad \vec{\delta}_2 = \frac{a}{2}(1, -\sqrt{3}), \qquad \vec{\delta}_3 = -a(1,0) \tag{2.24}$$

Also, graphene has sp^2 hybridization between one s and two p orbitals which forms trigonal planar symmetry of the unit cell. The s, p_x and p_y orbitals lead to formation of σ bonds with neighbouring carbon atoms. π electrons from p_z orbital form bonding π and anti-bonding π* of graphene. Bands form a deep valence band due to filled shell. π orbitals are covalently bonded to neighbouring carbon atoms and form π bands which are half filled. Quantum mechanical hopping between two sublattices leads to

formation of two energy bands and their intersection near the edges of the BZ yields conical energy spectrum near the K and K′ points (Fig. 2.18). Energy-momentum relation is given by $E_{dis} = \hbar\vec{k}\upsilon_F$. $\vec{k}$ is wave vector and υ_F is Fermi velocity (10^6 m/s). Due to linear dispersion relation, energy spectrum can be approximated by a parabolic dispersion relation. The gap in graphene can be opened either by 1) applying strain to graphene, 2) by doping, 3) by reducing one of the lateral dimension and, 4) applying bias to bilayer graphene.

An important aspect of graphene is linear energy-momentum relation with conduction band and valance band intersecting at Dirac point with no energy gap. The interaction of electrons with a periodic potential of graphene's honeycomb lattice gives rise to an electronic energy band structure, which exhibits a linear energy-momentum relation at low energies. Interaction of graphene with electron gives rise to complex electronic excitations called as quasiparticles. Quasiparticles are described by the (2+1)–dimensional Dirac equations with an effective speed of light (10^6 m/s) [41].

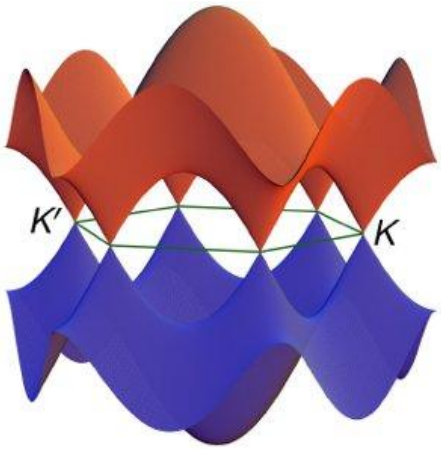

Fig. 2.18: Electronic band structure of graphene. Figure from: www.fkf.mpg.de/538305/70_Quantum-Transport

These quasiparticles which transport charge are referred as massless Dirac fermions. At low energies, graphene has linear dispersion relation near the six corners of 2D hexagonal Brillouin zone as shown in the Fig. 2.18. This gives zero effective mass for electrons and holes. Electrons travel on its 2D network as thousand interatomic distances without scattering. This results in high electrical mobility and leads a way to the development of high performance graphene-based electronic devices. Another important property of graphene is its thermal conductivity. Graphene has very high thermal conductivity as compared to any other carbon based system such as carbon nanotubes, graphite or diamond (> 5000 W/m/K). Due to its 2D structure, its thermal

conductivity is 5 times higher than that of graphite (1000 W/m/K). Also, it absorbs 2.3 % of light and transmits the rest 97% of light. Graphene is usually transferred onto silicon-dioxide to enhance the visibility of graphene flakes. Graphene also has good mechanical properties. Young's modulus of graphene reported is 1.0 TPa which is similar to that of bulk plane of graphite. It can be stretched to 20 % of its initial length [42]. It makes graphene a strong candidate for flexible displays (touch screens). Graphene electrodes due to high optical transparency and mechanical strength are superior to the transparent conducting electrodes such as indium tin oxides. Graphene has excellent chemical properties. Several molecules such as NO_2, NH_3 and OH act as dopant of graphene upon adsorption to its surface. These adsorbates can act as donors or acceptors and can change the carrier concentration. Graphene can be functionalized by various chemical groups (such as OH- and F-) to form graphene oxide and fluorinated graphene [43]. This makes graphene to be used in chemical sensing applications.

Several methods have been developed to grow a single layer of graphene. Graphene can be prepared by mechanical exfoliation of graphite [3, 44, 45], chemical exfoliation of graphite [46, 47], epitaxial growth by thermal decomposition of SiC [48, 49]. The largest area of graphene films can be obtained by CVD method [50, 51].

2.6.2 Chemical vapor deposition of graphene

Chemical vapour deposition is one of the most promising methods to produce single and few layer wafer-scale graphene. A schematic of graphene synthesis is shown in Fig. 2.19.

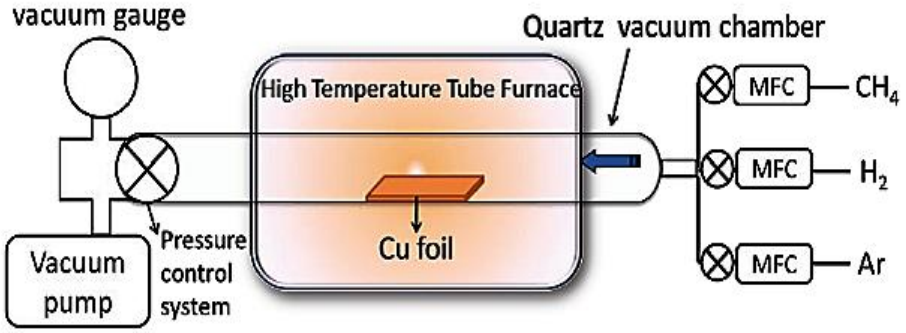

Fig. 2.19: A schematic for growth of graphene by chemical vapor deposition. Figure is taken from Ref. [52].

Graphene can be grown through thermal decomposition of hydrocarbons on the surface or by segregation of carbon atoms. Initially, B. C. Banerjee et al. [53] have found that when surface of Ni is exposed to a source of carbon gas, layers of graphite on Ni surface are observed. Growing popularity of graphene led to modify their methods to grow a single graphene layer on transition metals. Graphene has been successfully grown on Ni, Pd, Ru, Ir and Cu transition metals but Ni and Cu has been choice due to being relatively inexpensive than others. The limitation to use Ni as a substrate is that it is difficult to control the number of graphene layers [54]. This is due to the rapid segregation of carbon from the metal carbide upon cooling within the Ni grains and non-uniformly at the grain boundaries. The solubility of carbon in Ni is high (~0.9 atom % at 1000 °C) and growth of single and few layers of graphene are limited to tens of microns region and is not uniform all over the surface. Hence, Cu seems to be the most suitable choice due to low solubility of carbon in Cu (< 0.001 atom % at 1000 °C) [55]. It restricts the growth of graphene to the metal substrate. The schematic shows a tube furnace for high temperature heating, a vacuum chamber, vacuum and pressure controller and mass flow controllers (MFC) as a source of gas flow and other reactants.

Before growth of graphene, Cu is annealed in H_2 and Ar at 1000 °C for 30 minutes. The purpose of annealing is to remove the native Cu oxide by H_2 reduction and to increase the grain size of Cu foil as shown in Fig. 2.20. Graphene tends to grow on the grain boundaries of Cu, which can lead to multilayer growth. Large grain size of Cu reduces the effect of grain boundaries on graphene growth and graphene with large domains of different orientation can be obtained which coalescence to form continuous sheet. H_2 supply is switched off and methane is supplied. After growth, methane is closed and the sample is cooled down. Then methane is introduced with slow flow rate in the furnace (Fig. 2.19). The typical thickness of Cu is 25 μm. The substrate and the growth parameters have to be chosen carefully for growth of large, uniform graphene sheet.

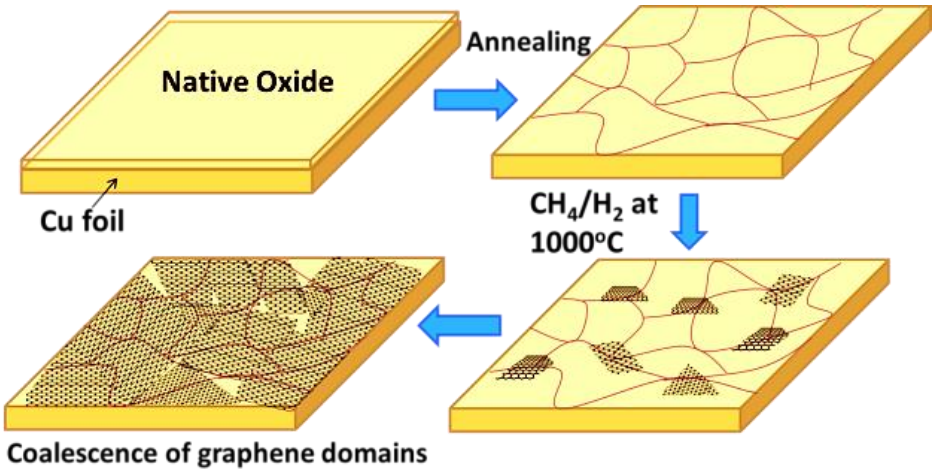

Fig. 2.20: Schematic showing the growth of graphene on Cu substrate by chemical vapor deposition. Cu is annealed at 1000 °C to remove native oxide and to enlarge the grain boundaries. Large graphene domains are formed and gradually coalescence to form continuous sheet. Figure is taken from Ref. [52].

A record 76 cm large graphene sheet has been grown by CVD growth method which makes it suitable for industrial applications [17]. The drawback of producing graphene by this method is that it needs vacuum chamber and high temperature processing for growth. Also, a complex procedure to transfer graphene from Cu to the desired substrate is required.

2.6.2.1 Graphene transfer onto substrates

Graphene from Cu foil is transferred to a desired substrate for practical applications. There are several methods to transfer graphene and are discussed below as:

1) **Wet chemical route:**

   In this method, PMMA is used to provide mechanical support to the graphene/Cu stack [56]. PMMA is spin-coated or drop-coated on the graphene. $FeCl_3$ in deionized water is used to etch Cu. $(NH_4)_2S_2O_8$ can also be used as Cu etchant. After etching is complete, PMMA/graphene stack is kept on cleaned substrate and left to dry. PMMA is removed in acetone and left PMMA residues can be cleaned by annealing in Ar/H_2 or vacuum. This method is widely used due to its reliability. Using this method, inch-size graphene sheets can be successfully transferred onto substrates. However, it is hard to avoid cracks and tearing in graphene film during the wet transfer.

2) **Dry transfer method:** Polydimythylsiloxane (PDMS) is used as a mechanical support to graphene/Cu stack for transferring to the desired substrate. Process of transfer is similar to the above mentioned wet transfer route. PDMS is attached to the graphene that was grown on Cu. After Cu etching is completed, PDMS/graphene stack is rinsed in deionized water and then transferred to the desired substrate. PDMS has a low adhesion force with graphene, and when graphene comes into contact with the substrate, it is more adhered to the underlying substrate than to PDMS. Hence, graphene is released from PDMS and remained attached to the substrate [51].

3) **Thermal tape method:** In this method, a thermal release tape is attached to graphene/Cu surface by applying a soft pressure (~ 0.2 MPa) [17]. After etching Cu in $FeCl_3$, graphene is cleaned with deionized water to remove the etchant residues. Subsequently, graphene with thermal tape on top is transferred to the clean substrate. Tape is released from graphene when the sample is heated at ~ 120 ˚C. Heating helps removing the tape and graphene adheres to the substrate. Tape residues on graphene surface can be removed in acetone.

4) **Direct transfer:** Graphene can also be transferred directly to a desired substrate. Graphene grown on Cu is directly kept in $FeCl_3$ solution to etch Cu without putting any support of PMMA on graphene. After Cu is etched, graphene sheet is cleaned in acetone, isopropanol and subsequently in deionized water. Thereafter, graphene is scooped with target substrate. Then sample is kept in HCl solution for half an hour to remove iron chloride residues. Advantage of this method is that graphene samples are much cleaner than standard PMMA supported method. However, cracks are difficult to avoid and generally flakes of millimeter size are obtained [57].

2.6.3 Exfoliated graphene

Graphene was first produced by micromechanical exfoliation method. In this method, a piece of thick graphite flake is put on tape and exfoliated many times spreading the flakes over the tape until a desired thickness is achieved. Atom-thick layers can be obtained. The tape prepared with graphene flakes is put against SiO_2 to transfer

graphene flakes. Graphene layers in graphite are weakly coupled by van-der Waals forces. Hence, it is easy to peel off graphene from bulk. The adhesion energy of graphene in bulk graphite is 0.45 Jm^{-2} and that for few layers of graphene is 0.30 Jm^{-2} [58]. This procedure produces the highest quality of graphene flakes. The force required to exfoliate graphene is 300 $nN/\mu m^2$ which is easily achievable with a Scotch tape. Graphene is visible due to enhanced optical path and due to its opacity. It makes easier to locate graphene on SiO_2 through optical microscope. Therefore, Si wafer with 90 nm or 300 nm thickness of SiO_2 is widely used for transferring of graphene flakes. Thickness of SiO_2 on Si is very important. A 5 % change in the thickness can make graphene invisible. Color of graphite flakes changes from yellow to bluish as thickness decreases to 10 nm.

The origin of the contrast of graphene layers can be explained using Fresnel's equations. Assuming that light is incident from air (n_0 = 1) onto a system consisting of graphene, SiO_2 and Si. Thickness of SiO_2 is d_2, is 300 nm and refractive index is denoted by n_2 which is wavelength dependent. Si layer is considered as semi-infinite and its refractive index $n_3$is also wavelength dependent. Graphene sheet has thickness $d_1 = \aleph\Delta d$, where $\aleph$ is the number of graphene layers and Δd(Δd=0.34 nm) is the thickness of single graphene layer and refractive index n_1. Intensity of the reflected light from the trilayer structure can be written as [59]:

$$I(n_1) = \left|(r_1 e^{i(\Phi_1+\Phi_2)} + r_2 e^{-i(\Phi_1-\Phi_2)} + r_3 e^{-i(\Phi_1+\Phi_2)} + r_1 r_2 r_3 e^{i(\Phi_1-\Phi_2)}) \times (e^{i(\Phi_1+\Phi_2)} + r_1 r_2 e^{-i(\Phi_1-\Phi_2)} + r_1 r_3 e^{-i(\Phi_1+\Phi_2)} + r_2 r_3 e^{i(\Phi_1-\Phi_2)})^{-1}\right|^2 \quad (2.25)$$

Where relative indices of refraction are defined as:

$$r_1 = \frac{n_0 - n_1}{n_0 + n_1}, \qquad r_2 = \frac{n_1 - n_2}{n_1 + n_2}, \quad r_3 = \frac{n_2 - n_3}{n_2 + n_3} \quad (2.26)$$

$$\Phi_1 = \frac{2\pi n_1 d_1}{\lambda}, \ \Phi_2 = \frac{2\pi n_2 d_2}{\lambda} \quad (2.27)$$

are phase differences due to the change in optical path at interface. λ is the wavelength of the incident light.

The contrast (C) is defined as intensity of reflected light in presence of the material and in the absence of the material:

$$C = \frac{I(n_1 = 1) - I(n_1)}{I(n_1)} \tag{2.28}$$

If the value of contrast is 0, graphene layer cannot be observed. If C has values between 0 and -1, then the layer appears darker than the substrate. On the other hand, if C has a value between 0 and 1, the graphene layer becomes brighter and is visible on SiO_2. Reflected intensity from substrate SiO_2 is calculated by using $n_1 = n_0 = 1$ and $d_1 = 0$.

Blake et al. [60] have done a quantitative analysis of contrast of graphene on three different thicknesses of SiO_2. They have simulated the results using refractive index of graphite, n_1 (λ) = 2.6-1.3i.

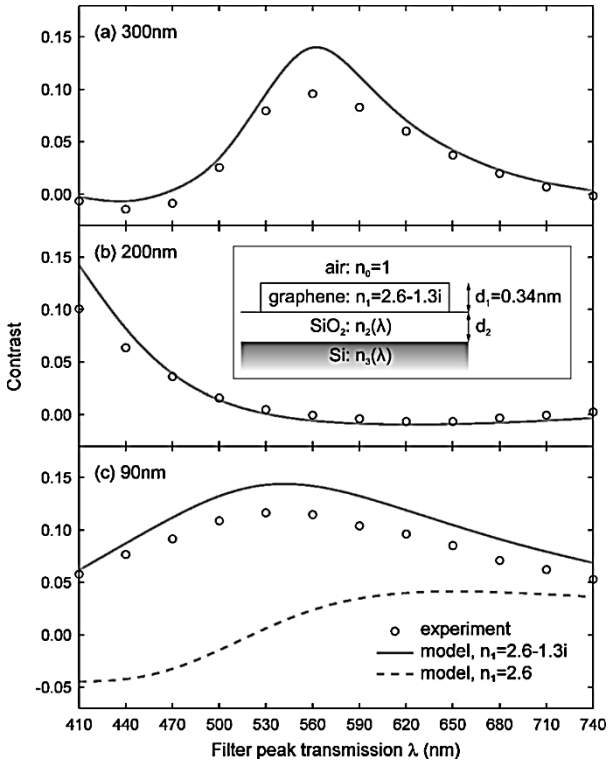

Fig. 2.21: Contrast spectrum obtained for three different thicknesses of SiO_2. Circles represent the experimental values and solid lines represent the calculations. Inset: geometry used for the analysis. Figure is taken from Ref. [60].

Fig. 2.21a shows that maximum contrast of graphene appears at ~550 nm for 300 nm thick SiO_2 layer. A SiO_2 layer of ~ 90 nm thickness can be even a better choice for graphene detection as seen from Fig. 2.21c. The contrast peak position remains

unchanged for 10 graphene layers [61]. The same graphene sample deposited on top of 200 nm thick SiO_2 is invisible (Fig. 2.21b). However, by using filters graphene can be visible on any thickness of SiO_2. Hence, contrast spectra can be used to determine the number of graphene layers in a stack. Ni et al. [60] have suggested that refractive index of graphene may be different than that of graphite. They have observed that refractive index of up to 10 graphene layers is $n_1 = 2.0\text{-}1.i$ for 300 nm thick SiO_2. Peak of the position moves toward the higher wavelengths. Contrast is negative for thick samples.

Graphene prepared by this method produces highest quality of electrical and structural properties. On the other hand, graphene obtained by this method have limited applications due to uncontrollable size, thickness, and location.

2.6.4 Epitaxial growth of graphene on SiC

Graphene can be epitaxially grown on SiC. It has already been known that graphite layers can be grown by thermal decomposition of SiC [48, 62]. Since discovery of graphene, researchers have been successful in growing thin layers of graphite by controlling the content of carbon in SiC [16, 63]. This method results in homogeneous, single crystalline graphene epitaxial films. A schematic of growth of graphene is shown in Fig. 2.22. In this process, SiC substrate is heated at ~ 1400 °C in ultra-high vacuum (UHV) under pressure of ~ 10^{-9} Torr. At this temperature, Si atoms start to desorb and remaining carbon atoms arrange to form a continuous graphene sheet. The quality and thickness of graphene layers depends whether the surface is Si-terminated or C-terminated. Graphene growth process is much slower on Si-terminated face than on C-terminated face. Uniformity of graphene layers is limited on both faces of SiC. However, it is more difficult to control growth of number of graphene layers on C- terminated face. Layer grown on C-face is called multilayer epitaxial graphene (MEG). MEG is ordered in a particular way with alternating 0° and 30° rotations relative to SiC. This is called non-Bernal stacking of multiple layers of monolayer graphene. On this face, de Heer et al. initially have grown graphene in a furnace at a very high temperature with an inert gas flow, but number of graphene layers was not homogeneous [49]. The electron mobility reported till now for

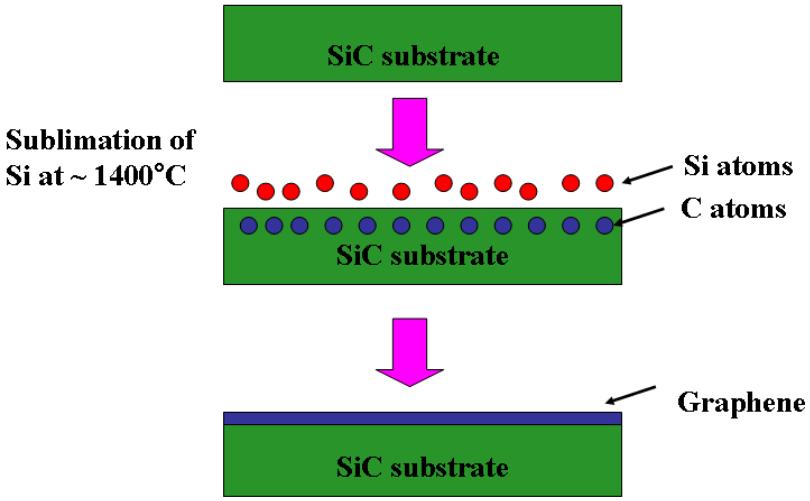

Fig. 2.22: Schematic showing formation of epitaxial graphene on SiC.

graphene grown on C-face is 10,000-30,000 cm^2/Vs while that on Si-face is 500-2,000 cm^2/Vs [64]. However, there is a large lattice mismatch of 20% between SiC (3.073Å) and graphene (2.46Å) and carbon arranges itself into hexagonal structure. It is possible that there exists areas of different thickness of graphene. The disadvantage of this method is that it is expensive to obtain graphene due to requirement of high vacuum and high temperature.

2.6.5 Reduction from graphene oxide (GO)

Graphene can be obtained by chemical reduction of graphene oxide (GO) and this is done via modified Hummers' method [65, 66]. This method involves exfoliation of graphite through oxidation in strong chemical oxidants such as HNO_3, $KMnO_4$ and H_2SO_4 [67] . A schematic is shown in Fig. 2.23. Resulting GO is separated by centrifugation and washed in HCl aqueous solution and deionized water to remove the acids. Thus prepared GO is filtered and dried in vacuum. These layers have oxygen containing groups such as epoxy, carbonyl, quinone, ketone and hydroxyl groups which reveals that graphite is oxidized [68, 69]. These functional groups act as reactive sites for nucleation of nanoparticles and give rise to graphene based composite materials [70].

Graphene from GO can be prepared by hydrazine treatment. GO is treated with hydrazine hydrate mixed in water and maintain the reaction mixture at 100 °C for 24 hours. Graphene synthesized using this method is called as reduced graphene oxide (rGO). Also, rGO can be created by directly heating GO in furnace at very high temperature (~ 1000 °C). Other methods to reduce GO is by microwave [71], electrochemical [72], photocatalytic [73] reduction methods. These methods help in partial restoring the sp^2 hybridized network by reducing the functional groups. Large scale production of rGO is possible by this method. On the other hand, graphene produced by this method contains large number of structural defects. Also, attached functional groups degrade the quality of rGO.

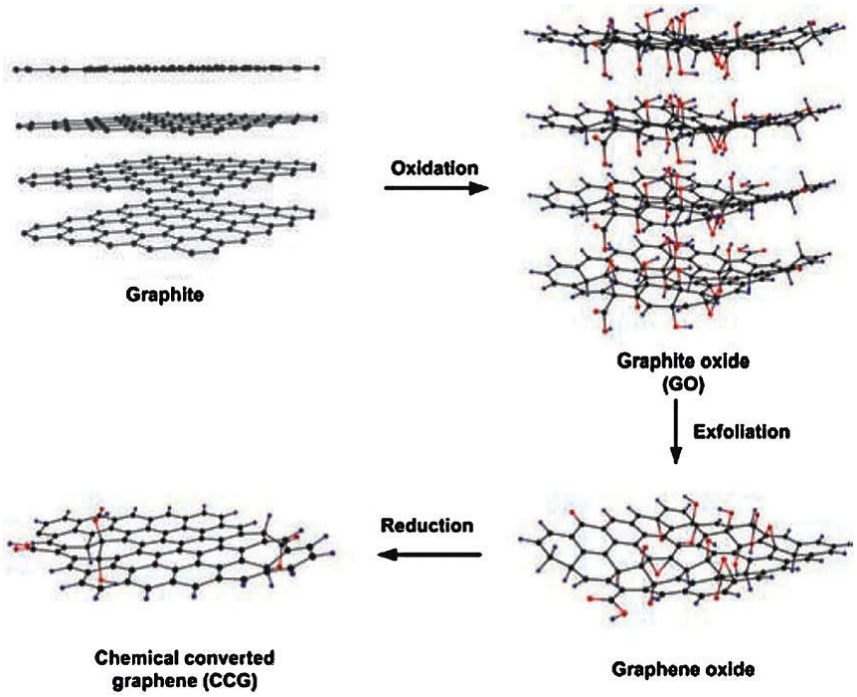

Fig. 2.23: Synthesis of graphene by chemical reduction of graphene oxide through oxidation of graphite. Figure is taken from Ref. [74].

2.6.6 Pentacene

Pentacene ($C_{22}H_{14}$) due to its relatively high charge carrier mobility of ~ 1 cm^2 /Vs is an excellent candidate for electronic applications [75]. It is a p-type organic semiconductor which forms well-ordered crystalline films on metals and insulators. Pentacene is a linear molecule with dimensions of 14 Å × 5 Å (Fig. 2.24). The C-C bond length ranges from 1.38 Å to 1.46 Å. Space group of pentacene is $\bar{P}1$. Pentacene

molecules are arranged in a herringbone structure. It has triclinic crystal structure and was first determined by Campbell and co-workers in 1961.

Fig. 2.24: Structure of pentacene crystal. It consists of five-fused benzene rings. Figure from: imgur.com

Three kinds of polymorphic structures have been reported as bulk, thin-film and single crystal phases. The thin-film phase is considered crucial for the electronic devices as charge transport occurs within the first few layers of pentacene on substrate. Thin layers of pentacene have four different crystalline phases depending on the growth conditions where pentacene molecules orient themselves in a direction perpendicular to the substrate surface [76, 77]. The d-spacing for these faces is found to be 14.1 Å, 14.5 Å, 15.0 Å and 15.5Å [78].

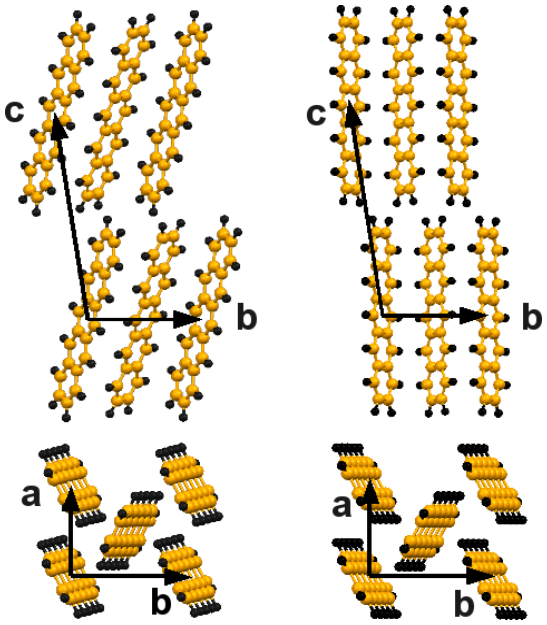

Fig. 2.25: Crystal structure for a) bulk, b) thin film phase. Figure is adopted from Ref. [79].

The difference between the bulk phase or Campbell phase and the thin-film phase is the interlayer distance which is 14.5 Å for the bulk phase and 15.4 Å for the thin-film phase. This results in change in a tilt angle between the long molecular axis and the perpendicular to a-b plane. The tilt angle for the bulk phase is ~ 22° while for the thin-film phase is less than 3° [79]. The surface energy is larger in (001) plane for the thin-film than for the bulk phase. Pentacene grown on SiO_2 is oriented with crystallographic (001) plane parallel to the substrate surface. Morphology of monolayer of pentacene is characterized by the two-dimensional islands, which have height of 15.4 Å. After a critical thickness, another crystalline phase, "bulk phase" is observed. Its morphology is characterised by lamellar-like structures. Table shows the crystal parameters for bulk and thin-films of pentacene [40, 80].

Reported in	a [Å]	b[Å]	c[Å]	α[°]	β[°]	γ[°]	D_{001}[nm]
[Thin film]	5.92	7.54	15.6	81.5	87.2	89.9	1.54
[Bulk]	6.06	7.90	15.01	81.6	77.2	85.8	1.45

Table 2.1: Unit cell parameters of the two crystal structures of pentacene.

3 Theory

3.1 Nucleation and growth models of thin layers

Scanning probe microscope and other high-resolution surface techniques have been used to study the growth of thin organic layers [81, 82]. Considerable efforts have been put to develop and analyse the models for epitaxial growth and related process [25, 83]. The aim of this Chapter is to provide detailed information about the underlying atomistic processes, which lead to the thin layer growth. The initial stages of growth are of particular importance, as growth of first layers influences the growth of the subsequent layers. During the deposition, atoms or molecules strike the surface of the substrate can adsorb or form chemical bonds at the periodic arrays of adsorption sites. Adsorbed molecules diffuse on the substrate and arrange themselves to form islands. Homoepitaxial growth comprised of the simplest class of the processes where atoms are deposited on the substrates of the same crystalline material [81]. This kind of growth leads to strain-free thin layers. In case of heteroepitaxial growth, a lattice mismatch occurs between the bulk crystalline lattice constant for the substrate and the deposited layer [84]. For small lattice mismatch, growth proceeds in the same manner as that for homoepitaxial growth. However, there are qualitative differences due to the interactions between adsorbate and the surface atoms and, due to the strain buildup in the deposited layer. For example, a three-dimensional growth of islands can be observed rather than two-dimensional islands. In this Chapter, we will discuss about the fundamental processes in growth of thin-films which can be deposited by deposition techniques such as molecular beam epitaxy (MBE) [85]. The fundamental processes involved during the growth are nucleation, aggregation, and coalescence of islands on a two-dimensional substrate. There are several approaches to analyse and understand these growth and aggregation process such as Smoluchowski rate equations, dynamic scaling and molecular dynamics. Before describing these two approaches, rate equations and scaling theory, we will first discuss the process of growth of islands on a substrate for atomistic lattice-gas models.

The following assumptions are made in physical quantities for growth models:

1) Deposition: adatoms (atoms) are deposited at random positions on the substrate with flux F per site per unit time.
2) Diffusion: atoms can move on the surface in random directions.
3) Aggregation: when two atoms meet on the surface, they form a stable island. Only irreversible aggregation is considered.
4) Desorption: atoms which are not incorporated into the lattice can reevaporate from the surface at a constant rate. It is also assumed that these desorbed atoms do not hit the surface again.

We will discuss briefly here lattice-gas models for submonolayer deposition to explain the fundamental aspects of nucleation theory. There are two kinds of models developed to study the submonolayer growth:

1) Point-island model: This is a computational approach for irreversible island formation. In this model, islands occupy a single site, but carry a label to indicate their size [86]. When an atom reaches a site adjacent to a point-island, size label is increased by unity each time which results in growth of that island. Size of the island is the number of atoms which belong to the island. Scaling behaviour for nucleation and growth process at low coverage of islands is elucidated in scaling theory and rate equations.
2) Generic lattice-gas models: In these models there is no prescribed critical size. Islands occupy more than one site on lattice and their shape is not trivial. Reversibility can be introduced by allowing dissociation of dimers of large cluster for $i > 2$. The critical size of islands is denoted as i above which islands are stable and immobile. One such model is Clarke-Vvedensky Bond-Counting model [87]. In this model, atoms can hop to the neighboring empty sites with activation barrier, $E_{act.}$ According to simple bond-counting algorithm, these deviate from the terrace diffusion barrier, E_d, $E_{act} = E_d + n_{ini} E_{NN.}$ E_{act} depends on the (n_{ini}) initial number of interlayer nearest-neighbor (NN) atoms before hopping. E_{NN} ($E_{NN} > 0$) is a measure of strength of intralayer NN atom interactions. There is no prior prescription of island size or critical size in this model. Therefore, this model is useful for providing natural testing ground for ideas of critical sizes.

Based on the above assumptions, to study the atomistic film growth, there are lattice - gas models which describe the growth of submonolayers. In these models, incoming

atoms with flux F are targeted onto a substrate [88]. Substrate is considered as a regular lattice with adsorption sites. Atoms are deposited randomly on the substrate and diffuse with nearest-neighbors with hopping rate $h = \upsilon \exp(-\beta E_d)$, where E_d is the activation barrier for diffusion, υ is the hopping frequency and $\beta = 1/K_B T$. When an atom encounter another atom, both atoms are frozen and form a stable island of size a. Similarly, when an atom is encountered to the existing island of size $a \geq 2$, it is irreversibly attached to that island upon reaching at the edge of the island and increasing the size to a +1. In the simplest case, the critical size is assumed to be 1(i = 1). New 2D islands are nucleated once stable islands are formed. Existing 2D islands grow with diffusion-limited aggregation (DLA). There is no additional step-edge barrier for downward motion of atoms and atoms are instantaneously attached at the edge of existing 2D islands.

3.2 Dynamic scaling theory

Scaling theory introduces the exponents which describe the scaling behaviour of island density, island size distribution with respect to coverage [89-91]. Scaling is a linear transformation for describing the extent or size of a length or area of islands studied. Scaling theory is applicable for low coverage where islands cover only a small fraction of the surface of the substrate. In case where islands occupy a finite fraction on the surface, deposition of atoms on the top of islands and their aggregation at the edges of the islands should be taken into account. Scaling theory is developed for diffusion-limited aggregation of islands where atoms and islands stick irreversibly to the substrate and each other. Diffusion-limited regime consists of four regimes. First, a low coverage regime, where atoms diffuse on the substrate surface and form a stable island when critical number of atoms meets. Second regime is the intermediate regime, where atoms nucleate new islands and also attach to the existing islands. Third, aggregation regime, atoms only attach to the existing islands. Finally, islands coalesce at high coverage. $N_a(\theta)$ is a fundamental quantity which describes the kinetics of growth, and is called as island size distribution function. a is the number of atoms in an island. θ is coverage which is expressed in terms of monolayers (ML) and is denoted as $\theta = Ft$. F is defined as a number of atoms deposited per site per unit time. Fundamental parameters, such as island density and coverage can be expressed as [92]:

$$N = \sum_{a\geq 2} N_a(\theta), \quad \theta = \sum_{a\geq 1} aN_a \tag{3.1}$$

In accordance to dynamic scaling assumption [89, 90] , there is only one mean island size *A(θ*) which is a function of fractional island coverage. An average island size can be written as

$$A = \frac{\sum_{a\geq 2} aN_a(\theta)}{\sum_{a\geq 2} N_a(\theta)} = \frac{(\theta - N_1)}{N} \tag{3.2}$$

where $N_1$is the density of isolated atoms.

This implies that $N_a(\theta)$ scales with $A(\theta)$. Therefore, island size distribution consists of two parts: one part containing the dependence on coverage and average island size and, another is a scale-invariant distribution function. Hence, $N_a(\theta)$ can be expressed as:

$$N_a(\theta) = S(A,\theta)\, f(u) \tag{3.3}$$

where $f(u)$ is a dimensionless scaling function of island-size distribution [93]. For islands which have finite spatial extent, $f(u)$ is assumed to be independent of θ. A particular distribution is dependent on the critical island size i. Here, $u = a/A(\theta)$.

Using the definition of coverage from equation (3.1) and scaling form of island-size distribution, one can write,

$$\theta = \sum_{a\geq 1} aN_a(\theta) = S(A,\theta)A^2 \int_0^\infty f(u)u\, du \tag{3.5}$$

It leads to the relation $S(A,\theta) = \theta/A^2$, a general scaling form of the island size distribution function from the dynamic scaling assumption can be expressed as:

$$N_a(\theta) = \theta\, A^{-2} f(u) \qquad (a \geq 2) \tag{3.6}$$

and scaling function satisfies $\int_0^\infty f(u)u\, du = 1$.

Therefore, equation (3.6) can be used to test the dynamic scaling assumption as $N_a(\theta)$, θ and A can be directly measured.

At late time, in the regime where coverage is very high, mean island size A scales as:

$$A \sim R^{\chi}\theta^{z} \tag{3.7}$$

R is the ratio of diffusion rate D to the deposition rate F. Using relation (3.7), equation (3.6) can be written as:

$$N_a(\theta) \sim R^{-2\chi}\theta^{1-2z} g_1\left[\frac{a}{R^{\chi}\theta^{z}}\right] \tag{3.8}$$

where $g_1(u) = \left(\frac{1}{c^2}\right) f(u/c)$, c = A/ $R^{\chi}\theta^{z}$. Atom density is very small. Therefore, equation (3.2) yields $A \backsimeq \theta/N$. The quantities which are of prime interest in steady state regime are island density N, average island size $A(\theta)$. They are related as:

$$N \backsimeq \frac{\theta}{A} \sim R^{-\chi}\theta^{1-z} \tag{3.9}$$

Therefore, we have defined the scaling relations for $N(\theta)$, $A(\theta)$ and $N_a(\theta)$ as a function of R and θ with independent exponents χ and z. Scaling exponent χ can be determined by measuring the variations in N as a function of deposition rate at a fixed temperature.

Similarly, we can define scaling relation for the atom density N_1 as:

$$N_1 \sim R^{-\gamma}\theta^{-\vartheta} \tag{3.10}$$

γ and ϑ are the scaling exponents used to characterize the atom density and coverage. If we consider that scaling form for island density $N_a(\theta)$ is true for atom density N_1, then using equation (3.6) and (3.8), γ and ϑ can be extracted as:

$$\gamma = (\omega + 2)\chi, \qquad \vartheta = (\omega + 2)z - 1 \tag{3.11}$$

Equation (3.11) may not be valid for realistic models where atom density scales differently from island density for $a \geq 2$.

3.3 Rate equation theory

This approach is used to study the kinetics of island growth processes. Kinetic rate equations consist of a set of differential equations which describe the time or coverage dependence of atom density and island density. It is assumed that only monomers

(atoms) diffuse on the surface. Let N_1 denotes the density of atoms and $N_a(t)$ denotes the density of islands of size a at time t. One can write a set of equations as [88, 94]:

$$\frac{dN_1}{dt} = F - K_1 N_1^2 - N_1 \sum_{a \geq 2} K_a N_a \tag{3.12}$$

$$\frac{dN_a}{dt} = N_1 (K_{a-1} N_{a-1} - K_a N_a) \quad (a > 1) \tag{3.13}$$

K_a is the rate of attachment of atoms to the islands of size a. K_1 represents the rate of attachment for the point island ($i = 1$). Equation (3.12) and (3.13) can be solved to find the coverage dependence atom density and island density. The exponents are determined by using the scaling forms (3.8) and (3.10) in equations (3.12) and (3.13). We can express atom density and island density from equations (3.12) and (3.13) as a function of coverage using the relation $\theta = Ft$. It is also assumed that $K_a \sim D a^p$ which represents the dependence of the rate of attachment on the island size. D is the diffusion constant of a single atom. $K_1 \sim D(a = 1)$. Using $R = D/F$, we get $K_1 \sim R$. Similarly, we can obtain $K_a \sim RF a^p$ and $K_{a-1} \sim RF(a-1)^p$. If we ignore the proportionality factor since it does not influence the scaling behaviour, and dividing by flux F, equation (3.12) and (3.13) can be rewritten as:

$$\frac{dN_1}{d\theta} = 1 - R N_1^2 - R N_1 \sum_{a \geq 2} N_a \, a^p \tag{3.14}$$

$$\frac{dN_a}{d\theta} = N_1 R[((a-1)^p N_{a-1} - a^p N_a)] \quad (a > 1) \tag{3.15}$$

One can write equation (3.14) and (3.15) in scaling form using the scaled variables $\hat{\theta} = R^{1/2}\,\theta$ and $\hat{N}_a = R^{1/2} N_a$ as:

$$\frac{d\hat{N}_1}{d\hat{\theta}} = 1 - \hat{N}_1^2 - \hat{N}_1 \sum_{a \geq 2} \hat{N}_a \, a^p \tag{3.16}$$

$$\frac{d\hat{N}_a}{d\hat{\theta}} = \hat{N}_1 [\big((a-1)^p \hat{N}_{a-1} - a^p \hat{N}_a\big)] \quad (a > 1) \tag{3.17}$$

Applying these equations for a point-island model where size of island is zero, one can get $K_a \sim D$ $(p = 0)$. Quantity p is related to the size of the islands. Therefore, equation (3.16) and equation (3.17) becomes

$$\frac{d\hat{N}_1}{d\hat{\theta}} = 1 - \hat{N}_1^2 - \hat{N}_1 \sum_{a \geq 2} \hat{N}_a \tag{3.18}$$

$$\frac{d\hat{N}_a}{d\hat{\theta}} = \hat{N}_1[(\hat{N}_{a-1} - \hat{N}_a)] \quad (a > 1) \tag{3.19}$$

Total scaled island density can be written as $\hat{N} = \sum_{a \geq 2} \hat{N}_a$. Using this, one can write equation (3.18) as:

$$\frac{d\hat{N}_1}{d\hat{\theta}} = 1 - \hat{N}_1^2 - \hat{N}_1 \hat{N} \tag{3.20}$$

Adding equation (3.19) over size $a \geq 2$, rate equation for point-island model can be written as:

$$\frac{d\hat{N}}{d\hat{\theta}} = \hat{N}_1^2 \tag{3.21}$$

Solution of these equations is described as follows:

In early-stage (early time) of growth, where coverage is very low ($\hat{\theta} \ll 1 \; or \; \theta \ll R^{-1/2}$) islands are still formed. Atom density N_1 is much higher than island density N. Therefore, neglecting the last two terms in equation (3.20) one can get:

$$\hat{N}_1 = \theta, \hat{N} \sim \hat{\theta}^3 \tag{3.22}$$

This implies that $N_1 = \theta$ and $N \sim R\theta^3$.

At later time where coverage is very high ($\hat{\theta} \gg 1$), island density is much higher than atom density. Last two terms in equation become important and thus equation (3.20) can be rewritten as:

$$\hat{N}_1 \sim \theta^{-1/3}, \hat{N} \sim \hat{\theta}^{1/3} \tag{3.23}$$

Therefore, for $\theta \gg R^{-1/2}$, island density and atom density can be written as $N \sim R^{-1/3}\theta^{1/3}$ and $N_1 = R^{-2/3}\theta^{-1/3}$ respectively.

Also, $A \backsimeq \theta/N \sim R^{1/3}\theta^{2/3}$ and it implies that for a point-island model the values of exponents are , $\vartheta = \chi = \frac{1}{3}$ and $\gamma = z = \frac{2}{3}$. However, for realistic models where island size is finite one has $p \neq 0$. It is observed that rate of capture of atoms by an island of size a is proportional to the linear dimensions of the island as well as to the diffusion constant. Scaled rate equation for island density N is also modified. For $p \neq 0$, the rate of attachment of atoms to the existing islands is written as $R_{att} \sim DN_1 \sum_{a\geq 2} N_a\, a^p$. In scaling regime, this can be expressed as $R_{att} \sim DN_1 NA^p$.

Therefore, rate equation (3.11) can be written as $dN_1/dt \backsimeq F - DN_1^2 - DN_1 NA^p$. Here, we are interested in the late-time regime where island density is very high ($N_1 \ll \theta$) so that

$$A = \frac{\theta - N_1}{N} \backsimeq \frac{\theta}{N} \tag{3.24}$$

Therefore, rate equations in this regime are written as:

$$\frac{dN_1}{dt} = F - DN_1^2 - DN_1\theta^p N^{1-p} \tag{3.25}$$

$$\frac{dN}{dt} = DN_1^2 \tag{3.26}$$

After dividing by F and rewriting these equations in terms of scaled variables $\hat{\theta} = (D/F)^{1/2}\,\theta$ and $\hat{N} = (D/F)^{1/2}N$, and $\hat{N}_1 = (D/F)^{1/2}N_1$, one can get

$$\frac{d\hat{N}_1}{d\hat{\theta}} = 1 - \hat{N}_1^2 - \hat{N}_1\hat{N}^{1-p}\theta^p \tag{3.27}$$

$$\frac{d\hat{N}}{d\hat{\theta}} = \hat{N}_1^2 \tag{3.28}$$

Power-law solutions can be obtained in the form $\hat{N} \sim \hat{\theta}^{1-z}$ and $\hat{N}_1 \sim \hat{\theta}^{-\vartheta}$ for $p \leq \frac{1}{2}$. In the scaling regime where $\hat{N} \gg \hat{N}_1$, $\hat{N}_1 << 1$ and $d\widehat{\hat{N}_1}/d\hat{\theta} \ll 1$, second term on right hand side in equation (3.27) can be ignored. Hence, equating first and third term of equation (3.27) we get $1 = \hat{N}_1\hat{N}^{1-p}\theta^p$. Using the latter equality and replacing the scaled variables, the exponents can be written as:

$$z = \frac{2}{(3-2p)}, \qquad \vartheta = \frac{z}{2}, \qquad \chi = \frac{z}{2}, \qquad \gamma = \frac{1}{2} + \frac{z}{4}, \qquad \left(p < \frac{1}{2}\right) \tag{3.29}$$

Therefore for $p < \frac{1}{2}$,

$$N \sim R^{-z/2}\theta^{1-z},\ N_1 \sim R^{-(1/2+z/4)}\theta^{-z/2} \tag{3.30}$$

In special case where $p = \frac{1}{2}$, we can extract the values of exponents as:

$$z = 1, \qquad \vartheta = \frac{1}{2}, \qquad \chi = \frac{1}{2}, \qquad \gamma = \frac{3}{4}, \tag{3.31}$$

For $p > \frac{1}{2}$, the value of exponents is:

$$z = 1, \qquad q = 2p - 1, \qquad \vartheta = p, \chi = \frac{1}{2}, \qquad \gamma = (1+p)/2 \tag{3.32}$$

For compact islands in two-dimensions, $p = \frac{1}{2}$ while for islands having fractal shape, $p = \frac{1}{d_f}$. d_f is the fractal dimension of the islands. Therefore, for fractal islands d_f = 1.7, we get $p = \frac{1}{d_f} \backsimeq 0.58$. This implies that $\vartheta \backsimeq 0.58$, $\gamma \backsimeq 0.79$ and q $\backsimeq$ 0.16.

Fig. 3.1 shows an example of the plot for atoms density (N_1) and island density (N) as a function of coverage at a fixed value of *R = D/F*. N is the density of islands of two or more atoms whereas N_1 is the density of isolated atoms.

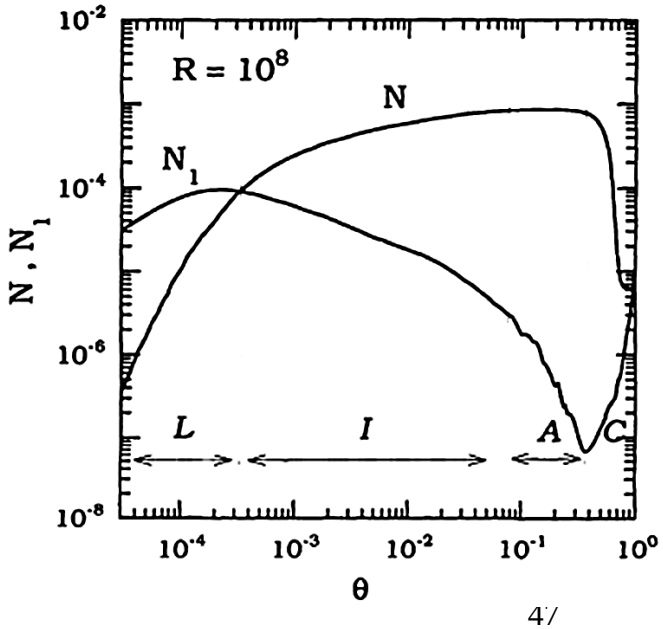

Fig. 3.1: Unscaled atom density (N_1) and island density (N) as a function of coverage θ. R = 10^8. Figure is taken from Ref. [90].

The variation of atom density and island density can be divided into four scaling regimes as discussed above. A low coverage regime (L), an intermediate coverage regime (I), aggregation regime (A) and coalescence and percolation regime (C). In the low coverage regime, atom density is very high [92]. N_1 is increasing due to deposition of new atoms. In the intermediate regime, as coverage increases, island density (N) also increases. Atom density (N_1) decreases in accordance with the relation predicted by equation (3.23) for the intermediate regime which implies that $N_1 \sim R^{2/3}\,\theta^{-1/3}$.

Subsequently, in aggregation regime, atoms are deposited either on top of the island or on the edges. Therefore, size of the islands is increased. Island density remains constant as atoms are attached only to the existing islands. Island density saturates at a coverage $\theta \geq 0.1$. Atom density drastically decreases as no new islands are formed. In coalescence regime, island starts to merge. The density of islands decreases due to the coalescence with the increase of number of atoms in the islands.

Amar et al. [92] have simulated the results for growth of islands which proceeds in a layer-by-layer growth mode. Fig. 3.2 provides an overview of the island morphology for three different values of deposition rate, $R = D/F$ =10^5, 10^7, 10^9. Coverage is also selected from aggregation regime to coalescence regime (θ = 0.1, 0.3, 0.7). Simulations were obtained for a system size (L×L) and L = 400 to 1024 lattice sites to obtain the morphology represented in Figs. 3.2(a-i). R was kept constant and morphology of islands was obtained by varying the coverage. Islands grow as fractal at very low coverages (Fig. 3.2a, Fig. 3.2d, and Fig. 3.2g). Probability of nucleation is higher than the probability of growth of the islands at very low θ. At low coverage regime, equation (3.22) for point-island is applicable which implies $N_1 = \theta$, $N \backsimeq R\theta^3$ and $\theta \ll R^{-1/2}$. However, as coverage increases islands start to become compact in shape. As coverage increases in intermediate regime, it follows $\theta \gg R^{-1/2}$. Rate equations $N_1 \sim R^{2/3}\theta^{-1/3}$ and $N \sim R^{1/3}\theta^{1/3}$ are applicable. This implies that $N_1 \ll N$. Therefore, $A \approx \theta/N \gg 1$. In aggregation regime ($\theta \geq 0.1$), atom density is very small and $A \backsimeq \theta/N$. Islands occupy a fraction of surface of substrate as represented in morphology of Fig. 3.2b, Fig. 3.2e, and Fig. 3.2h) respectively. Fig. 3.2c, Fig. 3.2f and Fig. 3.2i represents the morphology which corresponds to the coalescence regime.

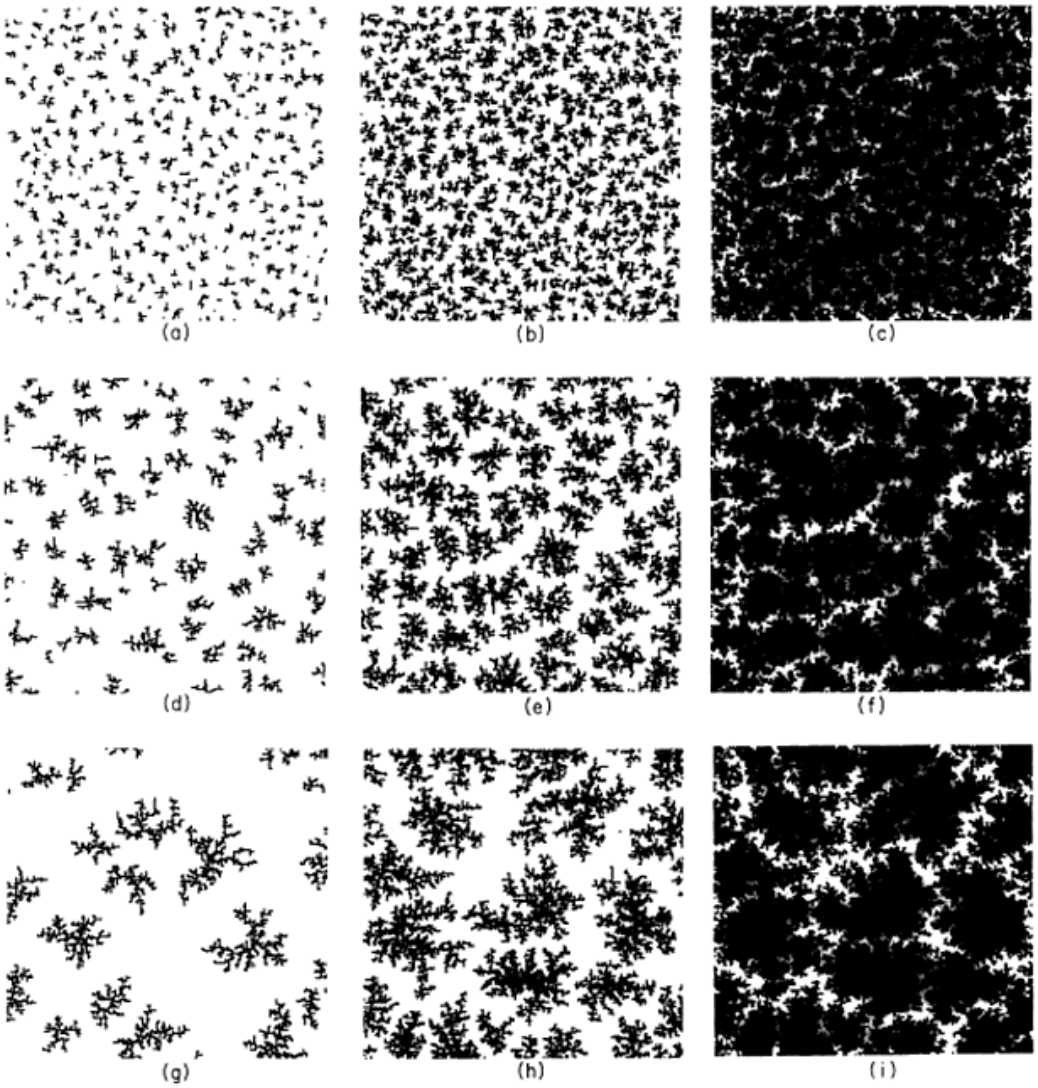

Fig. 3.2: Images of island morphology a) $R = 10^5$ at $\theta = 0.1$, b) $R = 10^5$ at $\theta = 0.3$, c) $R = 10^5$ at $\theta = 0.7$, d) $R = 10^7$ at $\theta = 0.1$, e) $R = 10^7$ at $\theta = 0.3$, f) $R = 10^7$ at $\theta = 0.7$, g) $R = 10^9$ at $\theta = 0.1$, h) $R = 10^9$ at $\theta = 0.3$ and i) $R = 10^9$ at $\theta = 0.7$. Figure is taken from Ref. [92].

Scaling theory and rate equation theory have been applied on a variety of islands growth system. Some of the studied homoepitaxial systems are Fe/Fe(100), Ni/Ni(100) Si/Si(100) and Cu/Cu(100) [95-98] Pb/Cu(001), Au/Ru(0001) and Ag/Si(111) [99-101] are studied as heteroepitaxial systems. Fig. 3.3 shows the example of the heteroepitaxial growth of Au on Ru(0001). Hwang et al. [98] have studied 2D growth of Au on Ru(0001) at room temperature (Fig. 3.3). Au islands on Ru form dendritic pattern as studied using scanning tunnelling microscope (STM) [100].

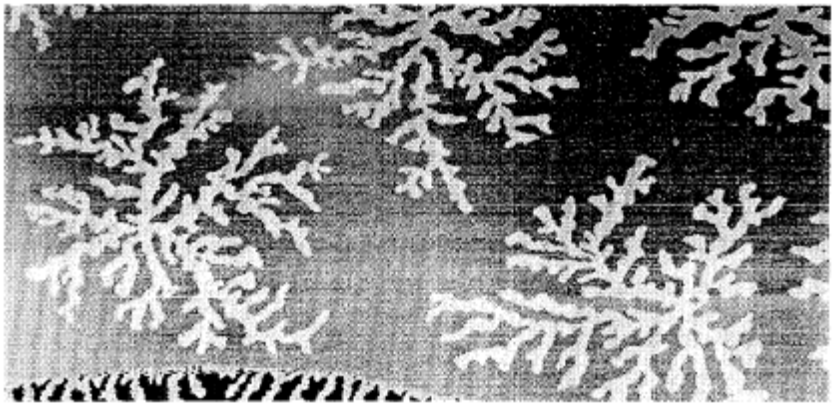

Fig. 3.3: STM image of Au islands on Ru(0001). Image size is 1.00μm × 0.65 μm. Figure has been taken from Ref. [100].

They have found that islands of submonolayers have fractal dimension, $d_f \backsimeq 1.7$ at $\theta \leq 0.3$ which corresponds to DLA regime. However, with increasing coverage islands exhibit compact shape. Dendritic growth has also been observed on Pt/Pt(111) at substrate temperature of 200K at $\theta = 0.2$[102]. Al on Al(111) exhibits fractal islands temperature range $25K < T < 150K$ [103].

3.4 A review on pentacene growth

Growth of organic molecule like pentacene has been studied extensively on metals, SiO_2 and on polymers. Morphology of pentacene layers depends on the interplay between intermolecular interaction and molecule – substrate interaction. Kinetic Monte Carlo (KMC) simulations have been used to model the growth of submonolayers on different substrates by taking into account all possible orientations of pentacene molecules [104]. KMC simulation is a computational method and has potential to explore the growth mechanism and optimize the deposition conditions.

Fig. 3.4 shows different scenarios for morphology of pentacene on various substrates which depends on the nature of binding to the surface and is calculated by KMC simulations [102]. Two deposition parameters, flux and substrate temperature were taken in framework of KMC simulations. Fig. 3.4a shows the morphology as a result when molecule – substrate interaction favors parallel (red) from vertical orientation (blue). Fig. 3.4b shows the case when molecule – substrate interaction in

both the orientations are comparable while Fig. 3.4c is for molecule – substrate interaction which is weaker in parallel than in perpendicular orientation. Color coded representation of different growth modes is shown in Figs. 3.4(e-h). Fig. 3.4d represents the morphology map when all the molecules parallel to the substrate form dendritic islands (gray). Compact islands (black) are formed when all the molecules lie parallel to the substrate (Fig. 3.4e). Formation of compact islands (light gray dots) when all the molecules are in perpendicular orientation is shown in Fig. 3.4f. Dendritic islands (dark gray lines) when most of molecules have perpendicular orientation and intermediate structures (light gray lines) which do not belong to any particular group are represented in Fig. 3.4g and Fig. 3.4h respectively.

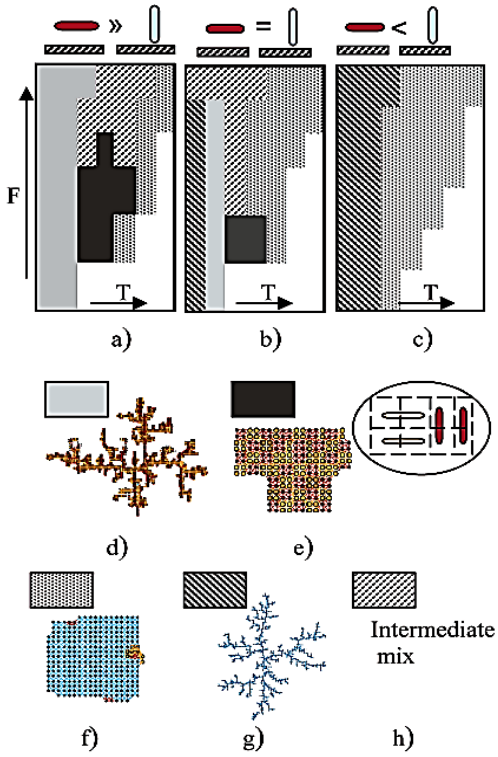

Fig. 3.4: A schematic showing morphology maps of pentacene molecules on different substrates. Figure has been taken from Ref. [104].

Pentacene morphology is significantly influenced even if there is slight change in the molecule – substrate interaction. For instance, low deposition rate and high temperature can result in a high degree of alignment of molecules and form compact islands. By tuning these parameters, a desirable morphology can be obtained.

Pentacene growth has been studied also on a number of inert substrates (Si, SiO_2, Al_2O_3). The most common inert substrate is SiO_2 because it is used as a gate dielectric in thin-film transistors [105-109]. Pentacene molecules on SiO_2 grow with their long

molecular axis perpendicular to the substrate. The morphology obtained by evaporation corresponds to the thin-film phase with interplanar spacing d_{001} = 1.54 nm [9]. The interplanar spacing in case of bulk is 1.45 nm. Fritz et al. [110] have done the grazing incidence x-ray diffraction (GIXRD) study on single layer of pentacene on SiO_2. They have reported the unit cell vectors in pentacene thin-films as, a = 5.916 Å, b = 7.588 Å, and γ = 89.95° with space group $P\bar{1}$. Pratontep et al. [12, 27] have studied the effect of the deposition rate and substrate temperature on the morphology of submonolayer coverages of pentacene on SiO_2. By controlling these two parameters the island size and island density can be tuned. Island density decreases and island size increases with temperature. Furthermore, their selected area diffraction (SAED) on pentacene islands reveals the crystalline nature of pentacene [12]. They observed that, for most of the islands, the arms of the dendrites have same in-plane orientation.

Treatment of the substrate also significantly affects pentacene morphology. For example, passivation of SiO_2 with self-assembled monolayers (SAMs) changes its wetting properties and makes the surface hydrophobic [111]. It completely changes the nature of interactions between pentacene molecules and the substrate. Shtein et al. [109] have found that pentacene islands on SiO_2 treated by SAMs have smaller size than on clean SiO_2. In addition, pentacene on SiO_2 treated by HMDS and treated by octadecyltrichlorosilane (OTS) has spontaneous aggregation in contrast to that on bare SiO_2 [14]. During spontaneous aggregation, molecules aggregate and form thicker grains. Aggregation on SiO_2 treated with OTS is significantly higher than SiO_2 treated with HMDS. The reported surface energy for SiO_2, HMDS and OTS are 61.4, 43.6 and 28.1 mJ/m^2 respectively. Low surface energy on SiO_2 treated by HMDS and treated by OTS is the origin of aggregation which is negligible on bare SiO_2. Since surface energy on OTS surfaces is lower than HMDS, this type of morphology on OTS is more thermodynamically stable.

Fig. 3.5 shows the morphology of submonolayer and 1.5 ML of pentacene on HMDS - treated and OTS – treated SiO_2 substrates [112]. Smooth OTS reveals a dendritic island growth while faceted islands on HMDS are signature of single crystal-like morphology of pentacene. Surface roughness also plays crucial role in morphology determination. HMDS (roughness~ 0.5 nm) surface is more rough than OTS (roughness~ 0.1 nm). Since the first layer is most influenced by the surface treatment, 1.5 ML thick pentacene or higher layer growth shows dendritic islands on

both the surfaces. Therefore, surface roughness is also an important parameter for the growth of layers.

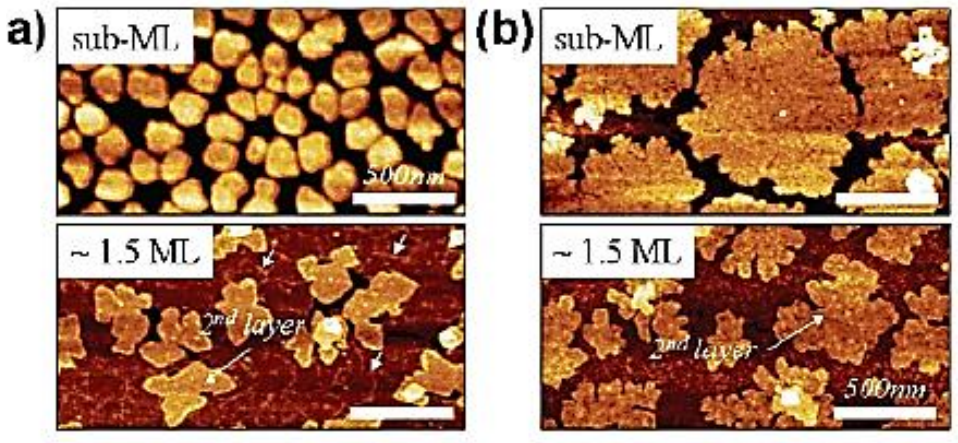

Fig. 3.5: AFM images of submonolayer and 1.5ML pentacene on a) HMDS treated and b) OTS treated SiO_2. Figure has been taken from Ref. [112].

Stadlober et al. [13] have done a quantitative analysis of the submonolayer growth of pentacene on inorganic and organic dielectric substrates using rate equation and scaling theory. They have compared the growth of pentacene on three organic substrates (PMMA, polyvinylphenol (PVP) and polyvinylcinnamate (PVCi)) to that on SiO_2. It was observed that pentacene growth on organic substrates is highly correlated and corresponds to DLA regime. Critical island size is $3 \leq i \leq 4$ at all substrates in the temperature range 25 °C to 70 °C. However, pentacene islands on PMMA have high probability to diffuse at the edges of islands that leads to round shape of islands. Rebernik Ribič et al. [113] have done similar study where a detailed analysis of growth of pentacene islands on polymeric substrates (polystyrene (PS), poly α-methyl-styrene (PαMS), PMMA) with respect to substrate temperature was carried out. It was observed that pentacene on polar substrates (PMMA) grows as 2D islands while on apolar substrates (PS, PαMS) a fraction of 3D nucleation is observed at higher temperature. Due to high activation energy for diffusion on PMMA, island density was much higher than apolar substrates (PS, PαMS).

On the other hand, pentacene growth on metals shows that intermolecular interaction is stronger than the interaction between pentacene molecules and the substrate. Molecules of the first layer align themselves parallel to the substrate. Pentacene has been grown on metal such as Ag, Au and Cu [114-116]. Pentacene

molecules can have standing-up orientation or lying-down orientation. Lukas et al. [114] have shown that pentacene molecules on Cu(110) prefer a closed pack lying-down orientation.

Harada et al. [117] have reported that pentacene molecules are weakly adsorbed on the graphite plane at low coverage. Molecules are aligned with their long molecular axis parallel to the graphite plane. Later, it was observed that arrangement of pentacene molecules on graphene is similar to that of graphite as top most layer of graphite is similar to graphene. They have used density functional theory (DFT) and dynamic vibrational coupling simulation to model the electronic and vibronic interactions at the interface. Carbon-carbon potential of pentacene – graphene interactions is computed as:

$$U_{cc} = 34\left(45.8\ \ exp^{-(3.3\ r_{cc})} - \frac{1}{r_{cc}^{6}}\right) \qquad [eV] \qquad (3.33)$$

where r_{cc} is the separation between carbon atoms. Electronic coupling between pentacene and graphene is stronger (40 meV) than among pentacene molecules (11 meV) for a monolayer of pentacene. It leads to parallel molecular alignment at low temperatures.

Fig. 3.6 shows the geometry of pentacene unit cell on graphene. It is observed that pentacene molecules are shifted with respect to each other to form a close packed structure. The rectangle shows the projection of pentacene molecules on graphene lattice and is reminiscent to the AB-AB stacking of graphene layers in graphite. Such a molecular arrangement was also predicted for other aromatic compounds such as benzene and naphthalene on graphene [118].

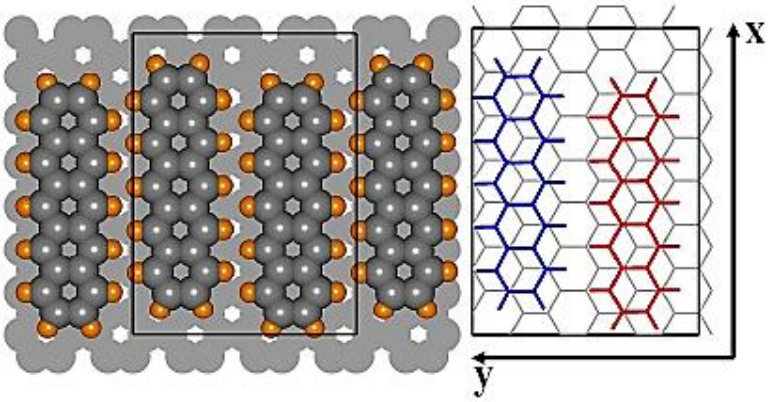

Fig. 3.6: Schematic of pentacene molecules adsorbed on the graphene sheet. Carbon atoms are shown in gray color and hydrogen atoms are shown in yellow color. Figure is taken from Ref. [119]

Gotzen et al. [120] have demonstrated using x-ray diffraction and near edge x-ray absorption fine structure spectroscopy (NEXAFS) that pentacene forms elongated islands on graphite with long molecular axis parallel to the graphite plane. It was also observed that on rough graphite surface, dendritic islands are formed with upright molecular orientation. However, with increasing coverage molecules are tilted at the interface. Evaporated submonolayers of pentacene have compact shape with up-right orientation and height of ~1.5 nm. Recent study of pentacene on graphene reveals the lying-down orientation. Lee et al. [7] have demonstrated that pentacene molecules on a clean graphene surface have lying-down orientation, while with polymer residues on its top led to upright orientation of pentacene molecules. The molecular arrangement and the morphology not only depends on the graphene surface, but can be strongly influenced by the underlying substrates. Recently, morphology of pentacene molecules deposited on epitaxially grown graphene on Ru(0001) was investigated by STM and DFT. It was observed that pentacene molecules prefer selective sites for adsorption at low coverage (< 0.1 ML). Graphene on underlying Ru(0001) exhibits Moire pattern and pentacene growth is strongly modulated by Moire structures at graphene/Ru(0001) interface [15]. We will also demonstrate in our work that pentacene morphology on graphene is strongly affected by the underlying substrate.

4 Grafold-driven nucleation of pentacene on graphene

4.1 Introduction

Graphene's in-plane Young modulus may reach TPa values 1 [42], nevertheless graphene foils can be easily folded in the out-of plane directions. Such folds—grafolds [121] form as strain-relieving features as graphene temperature is lowered after chemical vapor deposition of graphene onto copper foils, as described in detail in Ref. [122]. Grafolds are frequently encountered also after transferring of copper-free graphene sheets onto substrates such as SiO_2. In addition to increasing surface roughness of graphene, grafolds alter, locally its chemical reactivity and its electronic structure, and change the total energy of graphene lattice [123]. For graphene-based electronics that is likely to be based on CVD-fabricated graphene, it is therefore important to understand the influence of grafolds on the morphology of subsequent layers on graphene [124]. On SiO_2, for example, pentacene molecules nucleate in islands whose height does not exceed a length of a single molecule, and that at least two complete monolayers are formed before the third starts to nucleate [91]. Reports of pentacene growth on HOPG [20] and graphene [7] indicate less ordered growth exhibiting a three-dimensional morphology.

In this Chapter, we have focused on the nucleation phase of growth of pentacene on CVD-grown graphene transferred onto SiO_2 substrates. Special care has been devoted to the preparation of the substrates in order to remove almost completely the residues of PMMA that is used as a protective cover of graphene during etching of Cu foil, since Lee et al. [7] reported that PMMA islands may act as nucleation sites for pentacene. Our results show that on graphene surface that has as little as 0.2% of the area covered by PMMA residues, grafolds act as main attractors of pentacene molecules. Also, PMMA molecules are immobile at the substrate temperatures, at which pentacene growth is performed and therefore are less likely to act as nucleation centres. In particular, we found that the sites of intersection of several grafold lines become decorated with pentacene islands that exceed by far the amount of pentacene

contained in all other islands. We interpret this phenomenon in terms of enhanced reactivity of graphene at the location of grafolds [125].

4.2 Results and discussion

The as-received samples of CVD-grown graphene (Graphene Supermarket) comprised 25 μm-thick Cu foil, coated by a single layer graphene on both sides. A schematic of transfer of graphene onto SiO_2 substrate is shown in Fig. 4.1. A 400 nm thick layer of PMMA, Mw= 996 g/mol by GPC was dissolved in chlorobenzene and deposited on graphene/Cu/graphene structure at 80 °C. Cu foil was removed by floating the samples in iron chloride solution. As graphene is covered on both sides of Cu, we changed the solution after 1 hour when graphene film on backside of Cu was etched and float separately. After 3 hours, when Cu was completely etched, the PMMA/graphene film was washed with deionized water several times and dried. The target SiO_2 substrate having 300 nm thickness on Si wafer was cleaned in acetone and isopropanol for 10 minute each, and subsequently in piranha bath (a mixture of H_2SO_4 and H_2O_2 in 3:1 ratio) for 10 minutes. The dried PMMA/graphene film was put carefully on cleaned SiO_2 substrate at 90 °C and a drop of PMMA solution in chlorobenzene was coated on PMMA/graphene film to dissolve the PMMA layer. The procedure to transfer graphene using PMMA was adopted from Ref. [48]. When PMMA/graphene/SiO_2 film cooled down to room temperature, it was put in acetone

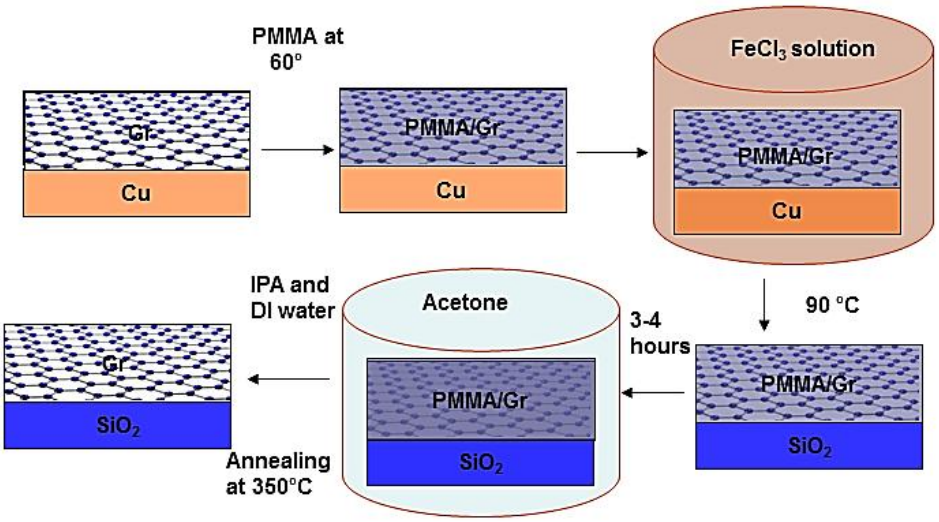

Fig. 4.1: Transfer process of graphene onto SiO_2 substrate via wet transfer method as described in Chapter 2 (Section 2.6.2.1).

for 1 hour to remove the PMMA. After that it was washed several times in hot acetone and subsequently in isopropanol and deionized water. The graphene/SiO_2 was treated in H_2/Ar at 500 °C for 1 h to remove the PMMA residues on graphene. To remove PMMA we have adopted the procedure described in details in Ref. [50].

Fig. 4.2 shows an optical microscopy image, a scanning electron microscopy (SEM) image and an AFM image of graphene transferred onto SiO_2 with PMMA support. Optical microscopy image (top) shows the regions of SLG, BLG and SiO_2 substrate. A continuous SLG covering mm of size is obtained. We have not observed any contamination on SLG from the optical image. However, there is some contamination (green color) on BLG sheet. SEM image (middle) represents the single layer (bright areas) as indicated with SLG and also shows the growth of second layer (dark circles). Graphene surface is characterized by folds as seen from SEM image. A 3×3 μm^2 AFM image shows the surface morphology of the transferred graphene film. An AFM operating in non-contact mode and recording the topography and the phase signal was used to check the degree of removal of PMMA on representative samples.The bright (white islands) islands show the left PMMA residues after transfer. The surface is characterized by grafolds whose height ranges from 1 nm (single-folded graphene) to 3 nm (multiply-folded graphene). In addition to grafolds we observe residues of PMMA as 8 nm high oval features covering less than 0.2% of the surface.

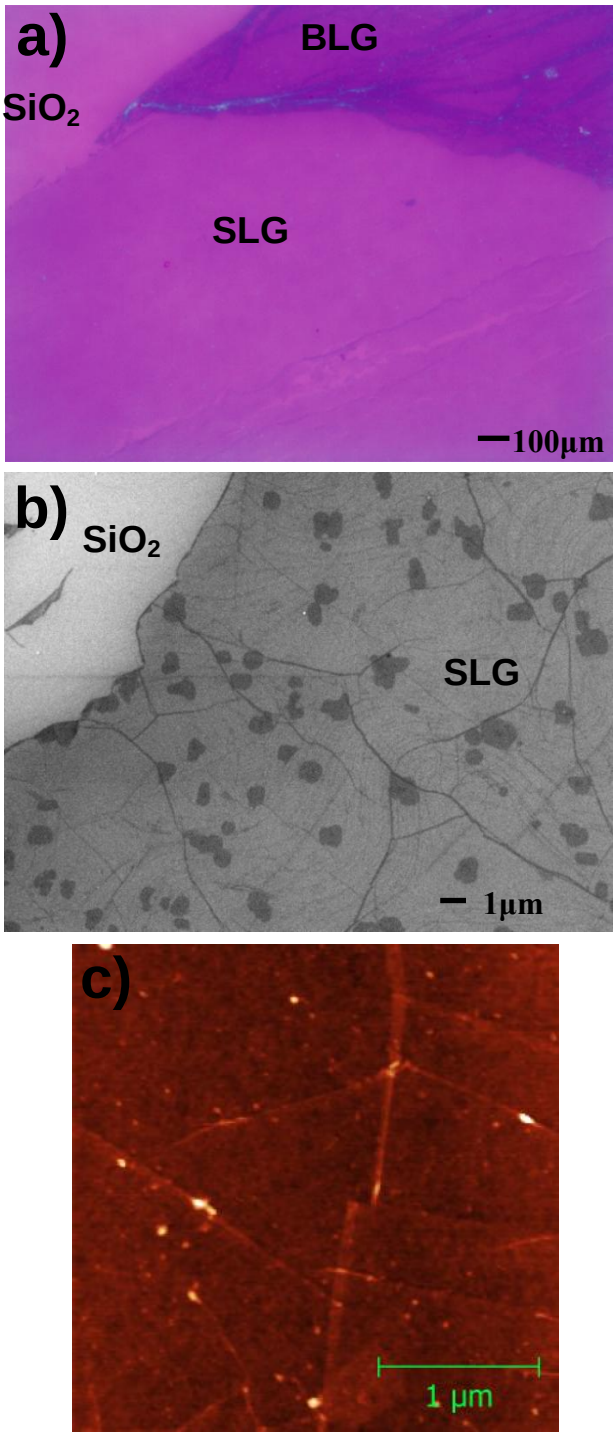

Fig. 4.2: a) shows Optical microscopy, b) scanning electron microscopy image and c) AFM image of graphene transferred onto 300 nm thick SiO_2 using wet transfer method. An AFM height scan is of a clean single-layer graphene sheet after transfer onto SiO_2 surface. The size of the scan is 3 µm×3 µm. The straight features are folds in graphene sheet. The lowest grafolds are 1 nm high, and the highest are 3 nm high. Upon transfer of graphene onto the substrate the samples were heat-cleaned at 500 °C for 1 h to remove most of PMMA. Oval features with typical height of 8 nm are residues of PMMA and represent a coverage of less than 0.2% of the graphene surface.

However, later we modified the cleaning procedure to that reported in Ref. [126] where acetic acid has been used for cleaning of PMMA residues. Firstly, most of the PMMA is removed in acetone. Secondly, graphene has been kept in acetic acid for one day. After that, graphene is scooped from acetic acid and rinsed in a mixture of methanol and deionized water several times and heated in vacuum for half an hour. This yields a clean graphene surface and free from contaminants. A 3×3 μm^2 AFM image of graphene transferred on SiO_2 is shown in Fig. 4.3.

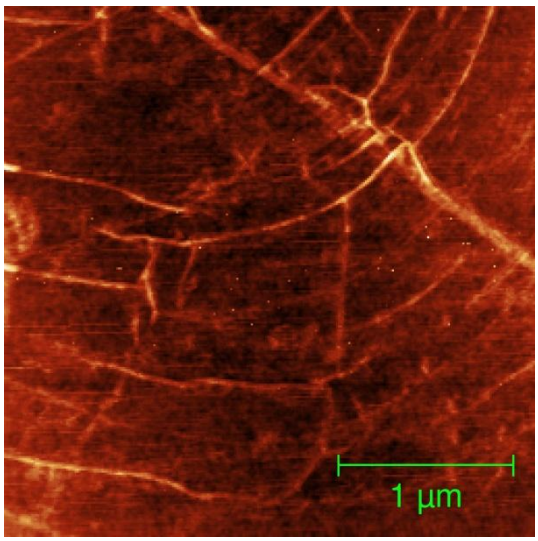

Fig. 4.3: A 3 ×3 μm^2 AFM image of CVD-graphene transferred by modifying the transfer procedure as in Ref. [32].

The pentacene layers were evaporated in a vacuum chamber (see Fig. 2.5) with a base pressure of 1×10^{-8} Torr onto the substrates at room temperature. Typical deposition rate was 1 nm/min. The topography of a pristine graphene surface prior to the deposition of pentacene is presented in a 3×3 μm^2 AFM scan in Fig. 4.2. On such surfaces a pentacene layer was deposited and exhibited morphology in its nucleation phase as demonstrated in Fig. 4.4, where we show a representative 3×3 μm^2 AFM height scan of a graphene surface covered by a pentacene layer with a nominal thickness of 0.9 nm. The image shows lines that correspond to grafolds of typical height of about 2 nm. Bright ovals are pentacene islands, and small dots are the PMMA residues. Since the false-color scale was adjusted so that grafolds are visible, the highest islands appear white. The majority of the islands are located near the grafolds, and in particular, at the points of intersection of several grafolds. Also, the

islands in these spots are higher than average and exhibit larger projected area than the islands that nucleate either on the flat areas of a graphene surface or at the straight sections of the grafolds.

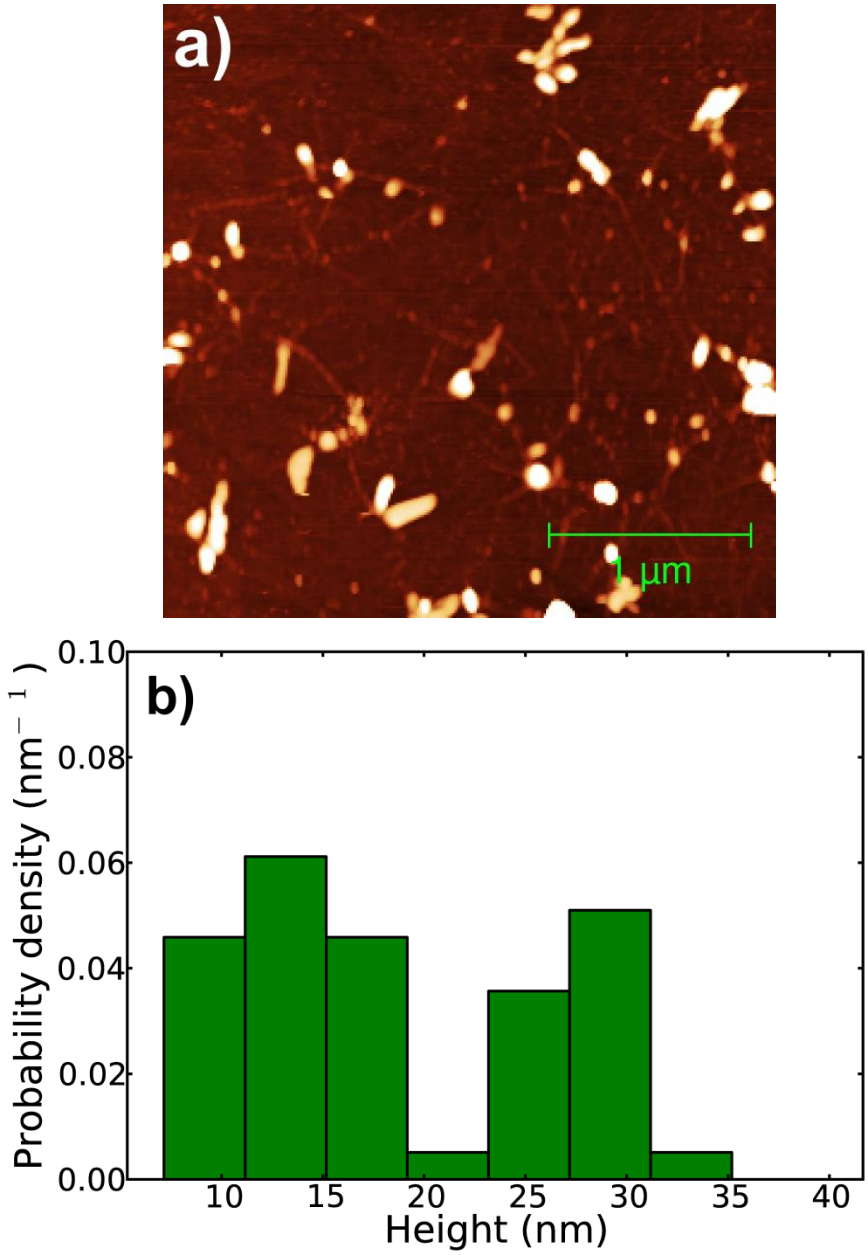

Fig. 4.4: a) 3×3 µm^2 atomic force micrograph of graphene surface covered by nominal thickness of 0.9 nm of pentacene at room temperature. Bright tones correspond to higher elevations. Thin lines are grafolds with typical height of 2 nm. Bright oval shapes are pentacene islands with the average height of about 27 nm. The false color scale was intentionally shifted so that the grafolds are apparent. The highest islands therefore appear white. b) A histogram showing the probability density for the island height of panel a). The histogram is the result of data obtained from 75 islands.

This is further evidenced in Fig. 4.4b, where we show the probability density histogram of island height. We see that, in addition to the leftmost peak corresponding to the lowest islands, an additional peak is observed at around 27 nm, and corresponds to the islands located at the intersections of grafolds. To measure the island height a polynomial background plane subtraction has been performed and zero of the height was set to the resulting background plane. The height of the islands was recorded relative to this reference. However, since graphene layer delamination off the SiO_2 surface may occur this procedure could lead to an overestimation of the island height. Therefore, the height of each island has also been checked, by measuring its height close to the island. In addition, the histogram shows a bimodal distribution that is likely a consequence of two different growth rates. The higher growth rate, resulting in higher islands, could stem from an increased chemical reactivity of the intersection of several grafolds, as discussed below. We see that the growth of pentacene on wrinkled graphene is of Vollmer–Weber type. The work of such heterogeneous nucleation of 3D islands is proportional to the supersaturation, i.e. the difference of the chemical potentials of the pentacene vapour and pentacene crystal at a given pressure, and the size of a critical nucleus [26].

Increasing the pentacene coverage to nominally 3 nm, pentacene islands enter into the coalescence phase. As shown in Fig. 4.5a, the islands continue their elongated morphology already observed in some of the islands in Fig. 4.4a. They appear as assembled by coalescence of the islands of the type shown in Fig. 4.4a. Assuming that pentacene molecules attach to the graphene surface with flat face on the surface [20, 127] the in-plane lattice mismatch amounts to 0.84 and 0.59 in the c and b directions of the unit cell, respectively (see Fig. 2.25). As demonstrated, for example, by Tersoff and Tromp [128] islands undergo a shape-transition phase as their size increases beyond the critical size. In order to compensate the elastic strain resulting from the lattice misfit they adopt a long, thin shape. The islands are also higher at the intersection of grafolds (rightmost peak in Fig. 4.4b). The island height decreases as the island extends away from the grafold intersection.

In Fig. 4.5b we show the height distribution of the islands. The histogram indicates that with increasing coverage the maximum island height does not increase significantly beyond that observed in the nucleation phase (Fig. 4.4). The incoming pentacene molecules become attached to the sides of the existing islands that propagate along the grafolds or perpendicular to the grafolds. The maximum

attainable height is likely a consequence of the lattice mismatch between the pentacene and graphene unit cells, and the associated strain present in the highest islands [128].

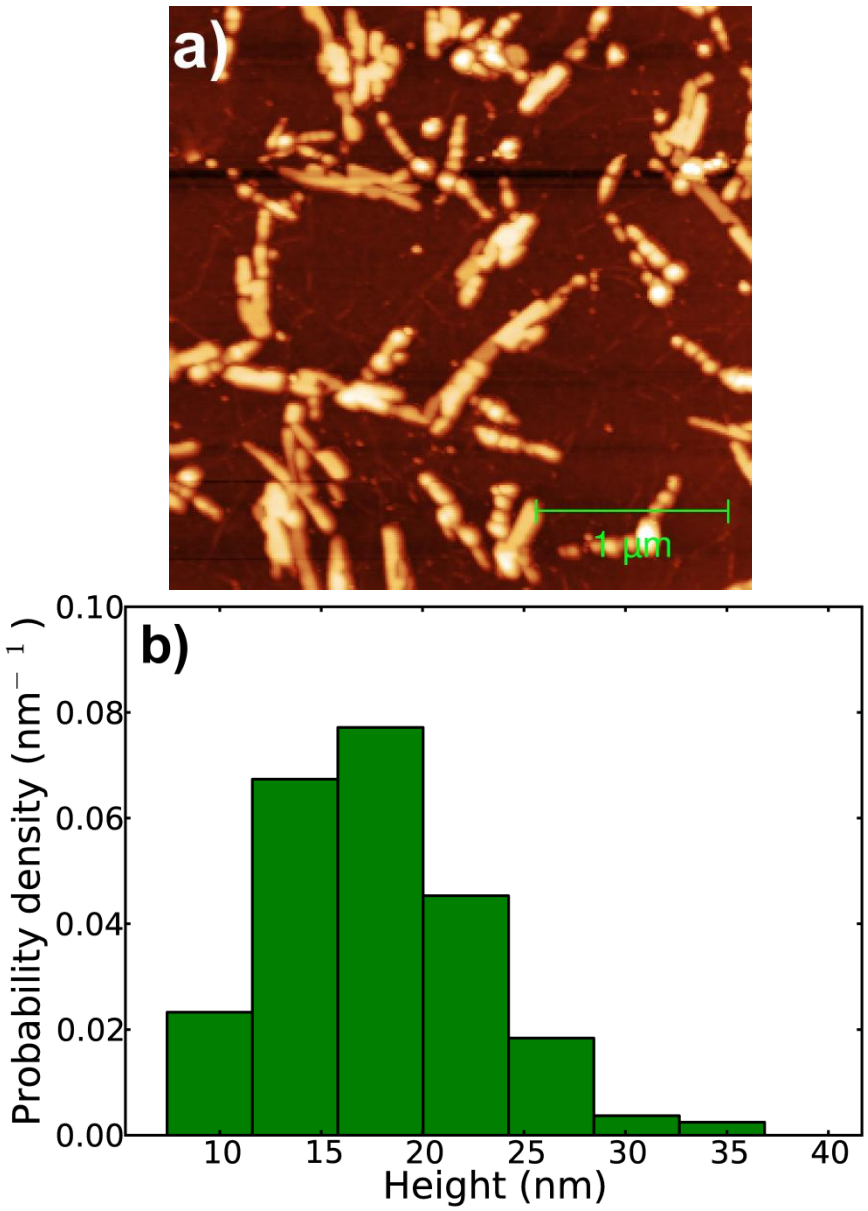

Fig. 4.5: a) 3×3 µm^2 AFM image of nominally 3 nm thick pentacene evaporated on graphene at room temperature. The shape of the pentacene islands reflects the coalescence phase of the layer growth. b) A histogram showing the probability density for the island height of panel a. The histogram is the result of data obtained from 192 islands.

We can, therefore consider grafolds as sites, where the interaction with pentacene molecules is increased, relative to the flat regions of a graphene surface. Such enhanced chemical reactivity has already been predicted in the case of mechanically

bent carbon nanotubes [129]. The chemical reactivity is likely to be further enhanced at the point of intersection of grafolds, where the structural deformation is even higher than along a single grafold. In our case, the influence of grafolds on attracting pentacene molecules may be even stronger, especially in the case of the multiply folded grafolds, where the graphene lattice is strongly bent [18]. These sites act as attractors of the pentacene molecules, leaving the flat regions of graphene nearly depleted of the pentacene molecules.

As suggested by Refs. [20] and [10], pentacene molecules on a flat graphene surface orient themselves with their longitudinal axis parallel to the surface forming the so-called lying-down phase. Such molecular orientation at a grafold could manifest itself as the thin-film phase relative to the inclined surface of the grafold. Since the thin-film-phase with a (001) face of the unit cell parallel to the surface is the one with the smallest surface energy [130], this further enhances nucleation rate at the grafolds (Fig. 4.6).

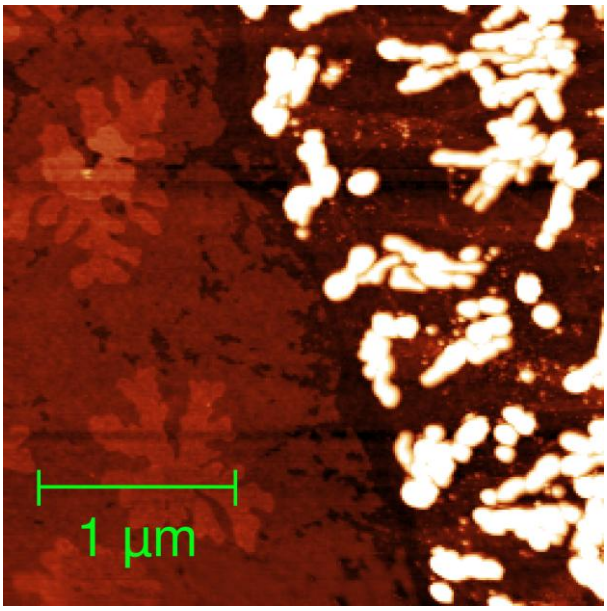

Fig. 4.6: A 3x3 μm^2 atomic force micrograph of the interface region between SiO_2 (leftmost region) and graphene (rightmost region) covered by nominally 3 nm thick pentacene layer. Pentacene on SiO_2 grows in a layer-by-layer mode, as seen from the dendritic islands of an average height of 1.5 ±0.2 nm. On graphene we see that pentacene grown as three-dimensional islands with height distribution illustrated by the histogram in Figure 4.4b.

As discussed in the previous Chapter, the driving force for nucleation is supersaturation. We have to understand the unusually high density of pentacene molecules at the intersection of the grafolds. To address this issue, we have transferred SLG on SiO_2. Sample was transferred in a way that there is significant amount of PMMA residues on graphene surface. Sample was not given any thermal treatment. We have evaporated pentacene on graphene with PMMA as can be seen from a 5×5 μm^2 AFM image of Fig. 4.7a. Small dots represent PMMA islands with an average size 60 nm and average height 2 nm. We observe that despite the presence of PMMA, pentacene islands still nucleate on grafolds. Average height of pentacene islands is 15 nm. The same sample was annealed in vacuum at 350 °C for 30 min to remove the PMMA off the graphene surface [7, 50]. This annealing condition was also effective in removal of pentacene from graphene surface. Surface morphology of clean graphene surface after annealing is shown in Fig. 4.7b. The topography shows almost no PMMA residues. Height of the grafolds ranges from 1 to 1.5 nm. Pentacene was deposited on clean graphene surface under the same conditions as for Fig. 4.5a. Fig. 4.7c shows pentacene islands on graphene surface comprised of grafolds. We observe again that pentacene islands preferentially nucleate on the grafolds sites.

At the outset, we note that the observed pentacene layer morphology on our graphene substrates can not be reconciled with the presence of PMMA residues [7]. Instead, we propose that the observed island growth is likely to be driven by the presence of grafolds. The driving force for attracting pentacene molecules to the grafolds is of a chemical and a morphological type. Triply-folded grafolds have been treated theoretically by Kim et al. in the framework of pseudopotential density-functional theory [18]. Their results suggest that the electronic structure of graphene is altered at the location of grafolds, and exhibits semimetallic behavior, with the π states having an indirect overlap near the K point. In addition, Kim et al. demonstrated that molecules of C_{60}, although randomly deposited onto the graphene surface, preferentially intercalated within a grafold.

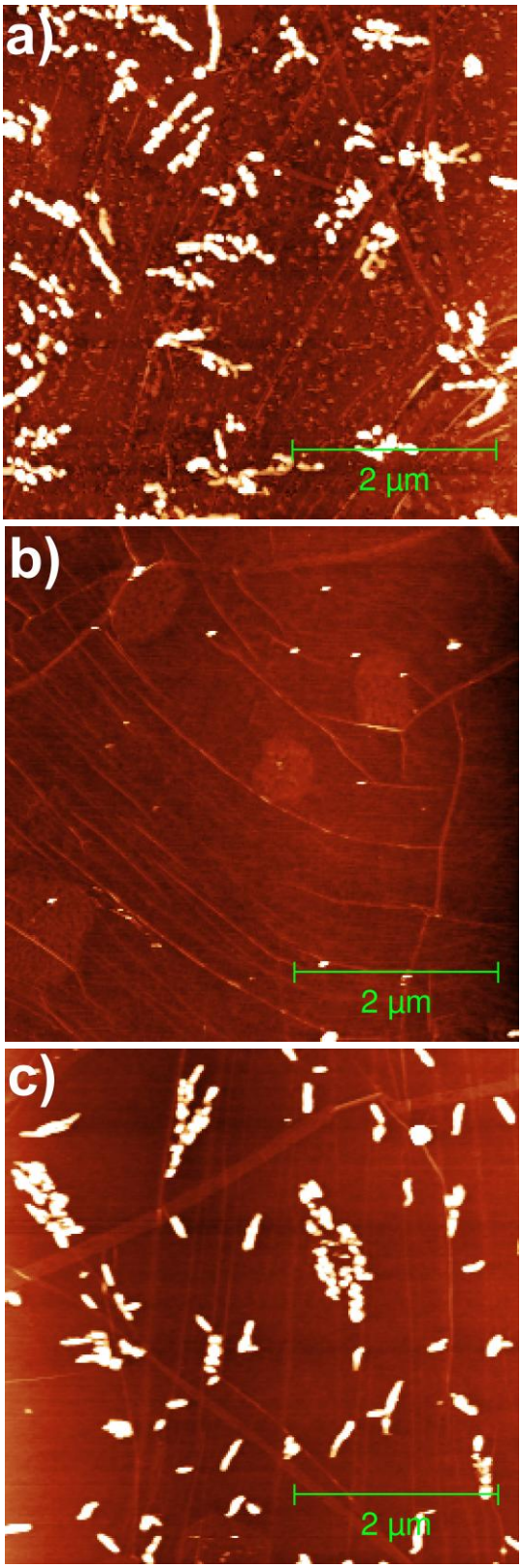

Fig. 4.7: 5×5 µm^2 AFM images of a) pentacene on single layer graphene transferred onto 300 nm thick SiO_2. Small dots are the PMMA residues, b) graphene cleaned by thermal treatment, c) pentacene evaporated on clean graphene under same conditions as done in case of Fig. 4.5a.

We have also investigated the surface energy of graphene on SiO_2 substrate by measuring the contact angle of deionized water, diiodomethane, and ethylene glycol. A schematic of the contact angle measurement is shown in Fig. 4.8. A μm-size liquid drop was released from a microsyringe onto the substrate surface. Images of liquid drop were obtained using CCD camera. The liquid contact angle was determined by measuring the angle between tangent line and the droplet-substrate interface line. Rebernik Ribic et al. [113] have examined the morphology of sub-monolayer thick pentacene films on several substrates that exhibited different contributions of the

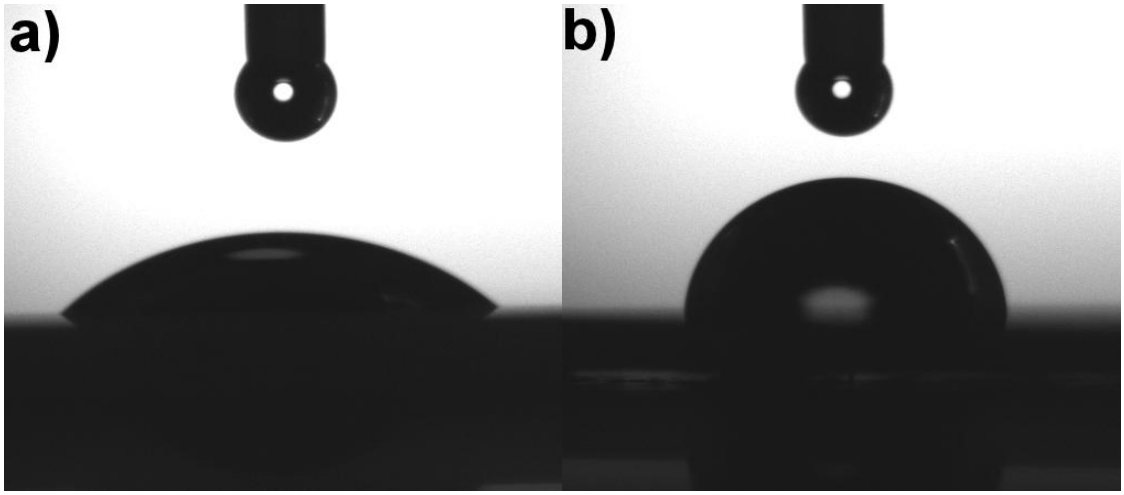

Fig. 4.8: Contact angle measurement of liquids on a) SiO_2 and on b) graphene.

polar and the dispersive component of the surface energy. There, it was observed that the pentacene-substrate interaction is weaker on nonpolar surfaces. On strongly polar substrates such as SiO_2, the pentacene nucleates in a layer-by-layer mode, forming strongly dendritic islands (Fig. 4.6, and Refs. [27, 91, 113]). On polymeric substrates with lower polar contribution to the surface energy, pentacene islands appeared more compact and exhibited a strong tendency towards the 3D growth. We have therefore examined the graphene surface from the standpoint of polar contribution to the surface energy and employed Owens-Wendt approach [131]. By measuring contact angle of deionized water, diiodomethane, and ethyleneglycol and using the values for the polar and the dispersive energy of the liquids from Ref. [113], we have obtained

the values for polar and dispersive energy for SiO_2, graphite and graphene, as reported them in Table 4.1. The errors quoted arise from the fitting procedure to the linear function [113, 131]. While total surface energy of all three substrates is similar, the magnitude of the polar component differs considerably, and was found to be 43.53 ± 6.9 mJ/m^2, 3.64 ± 1.7 mJ/m^2 and 0.47 ± 1.4 mJ/m^2 for SiO_2, graphene and graphite, respectively. The observed 3D growth mode of pentacene on graphene is therefore driven by a reduced interaction between pentacene molecules and the graphene surface, relative to the interactions between pentacene molecules and the SiO_2 surface.

Substrate	Polar component of surface energy (mJ/m^2)	Dispersive component of surface energy (mJ/m^2)	Total surface energy (mJ/m^2)
SiO_2	43.53±6.9	22.85±7.5	66.39±15.4
Graphene	3.64±1.7	38.74±6.3	42.38±8.0
HOPG	0.47±1.4	43.29±9.2	43.77±10.6

Table 4.1: The values for polar, dispersive and total surface energy for SiO_2 and graphene obtained from measurements of the contact angle of deionized water, diiodomethane, and ethyleneglycol and using the values for polar and dispersive energies of the liquids from Ref. [111]. The errors quoted arise from the fitting procedure to the linear function.

We have also monitored the effect of substrate temperature on pentacene morphology on graphene at low coverage. Fig. 4.9 shows the pentacene morphology on graphene at three different substrate temperatures (T_s = 29 °C, 37 °C, 53 °C), when the coverage is very low and thickness of pentacene was 0.6 nm for all three measurements. At T_s = 29 °C, pentacene starts to nucleate at grafolds as discussed before. With increasing temperature to 37 °C, the probability of nucleation decreases and islands only reside at the intersection of grafolds. Island density also decreases and island area is enlarged as observed from AFM micrograph. Further increasing temperature to T_s = 53 °C, island density decreases drastically. Grafolds at this temperature do not support the nucleation of pentacene at such low thickness. The nominal height of islands is 20 nm.

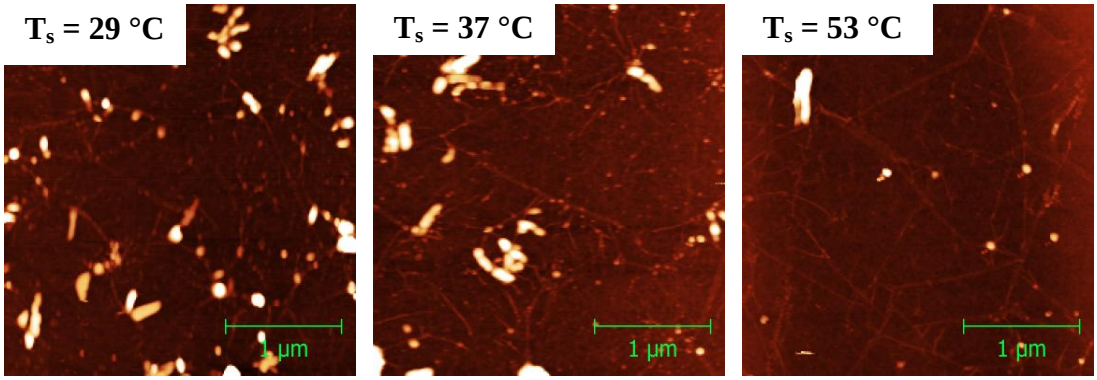

Fig. 4.9: AFM images of pentacene islands on graphene at substrate temperaturs , T_s = 29 °C, T_s = 37 °C, T_s = 53 °C respectively The typical height of pentacene islands is 20 nm. Small dots correspond to PMMA residues.

Fig. 4.10 shows a 3×3µm^2 AFM image of pentacene deposited on graphene at substrate temperature T_s = 60 °C. The nominal thickness of pentacene was 4 nm. We observe that there is a significant numer of pentacene islands at T_s = 60 °C at high coverage. The typical height of islands is 15 nm. The nominal length of islands becomes 0.6 µm. Mean size of islands is 73 nm. As observed already in Fig. 4.5, with increasing coverage islands tend to align themselves in close proximity of the grafolds. Also, surface diffusion is high at high substrate temperature. We have observed that with high coverage pentacene islands are elongated along the grafolds which allows a better relaxation from strain. Strain is defined as the change in dimension per unit the original dimension.

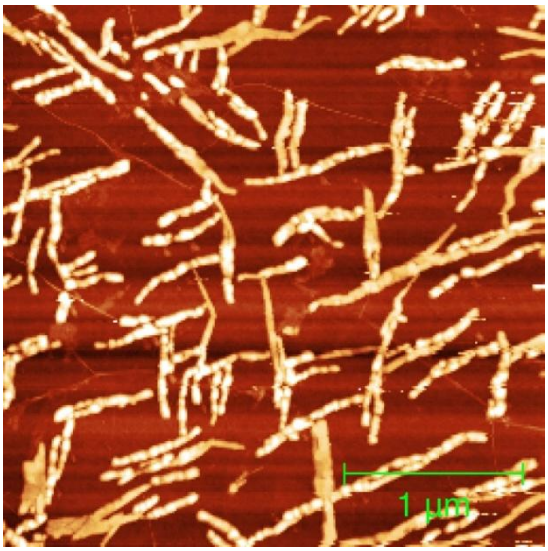

Fig. 4.10: AFM micrograph of pentacene evaporated at substrate temperature, T_s = 60 °C.

Graphene is strained due to lattice mismatch with the substrate and elongation occurs along the direction of smaller lattice mismatch [128]. Incoming pentacene molecues are attached to the existing islands enhancing the length of islands. Strain between the islands and the substrate significantly affect the shape of the islands. Relaxation from strain includes the shape transition of islands from compact islands to elongated islands during the growth process [125, 128]. The shape and size of the islands changes with the deposition parametrs. Therefore, strain can be considerd as a possible driving force for the movement and location of islands.

Selected graphene substrates were also examined by Kelvin force microscopy. The KFM measurements were made using the same AFM microscope equipped with a conductive tip working in a non-contact mode. Measurements were performed at room temperature and under ambient conditions with humidity level 36%. We have used Olympus platinum-coated silicon probes (spring constant = 2 N/m). Surface potential was measured by applying a 1 V ac voltage. Frequency of the surface potential modulation was 16 kHz. In order to examine the eventual differences in electronic energy structure at the location of the grafolds relative to the unfolded graphene, we have employed KFM on samples comprising graphene layers that exhibited a typical degree of folding. In Fig. 4.11 we show a comparison between a topographic map (Fig. 4.11a) and a KFM scan (Fig. 4.11b) of the 1x1 μm^2 region of the graphene sample. The topographic scan shows 1.5 nm high folds. We interpret the observed contrast based on the calculation reported in Ref. [18]. The electronic energy band structure of triply folded graphene exhibits a semimetalic character with a small indirect overlap between the conduction and valence band. The partially empty valence band and partially filled conduction band near the Fermi level of such energy band structure imply the presence of free charges that can efficiently screen the electric filed due to the electric charge of the biased tip. This gives rise to a measureable force detected by the KFM. We have measured the contact potential difference between the tip and the sample surface. Fig. 4.11c represents the distribution of contact potential on flat graphene region (black squares) and distribution of contact potential on grafolds (pink circles). Both the distributions are well fitted with Gaussian distributions. KFM image shows two main levels of contrast, whereas low surface potential corresponds to the folds on graphene and high potential areas are flat graphene. Dark structures in the KFM image correspond to low

potential difference. The contact potential difference measured between grafold and flat graphene regions is 42 meV. Observed grafolds are dark while the unfolded regions of graphene are brighter. This suggests that grafolds have lower potential than unfolded graphene regions. The difference in contact potential shows that grafolds and unfolded regions have different work functions. As discussed before, electronic structure is changed at grafolds, therefore, increase in chemical reactivity at the grafolds can be the cause of attraction of pentacene molecules.

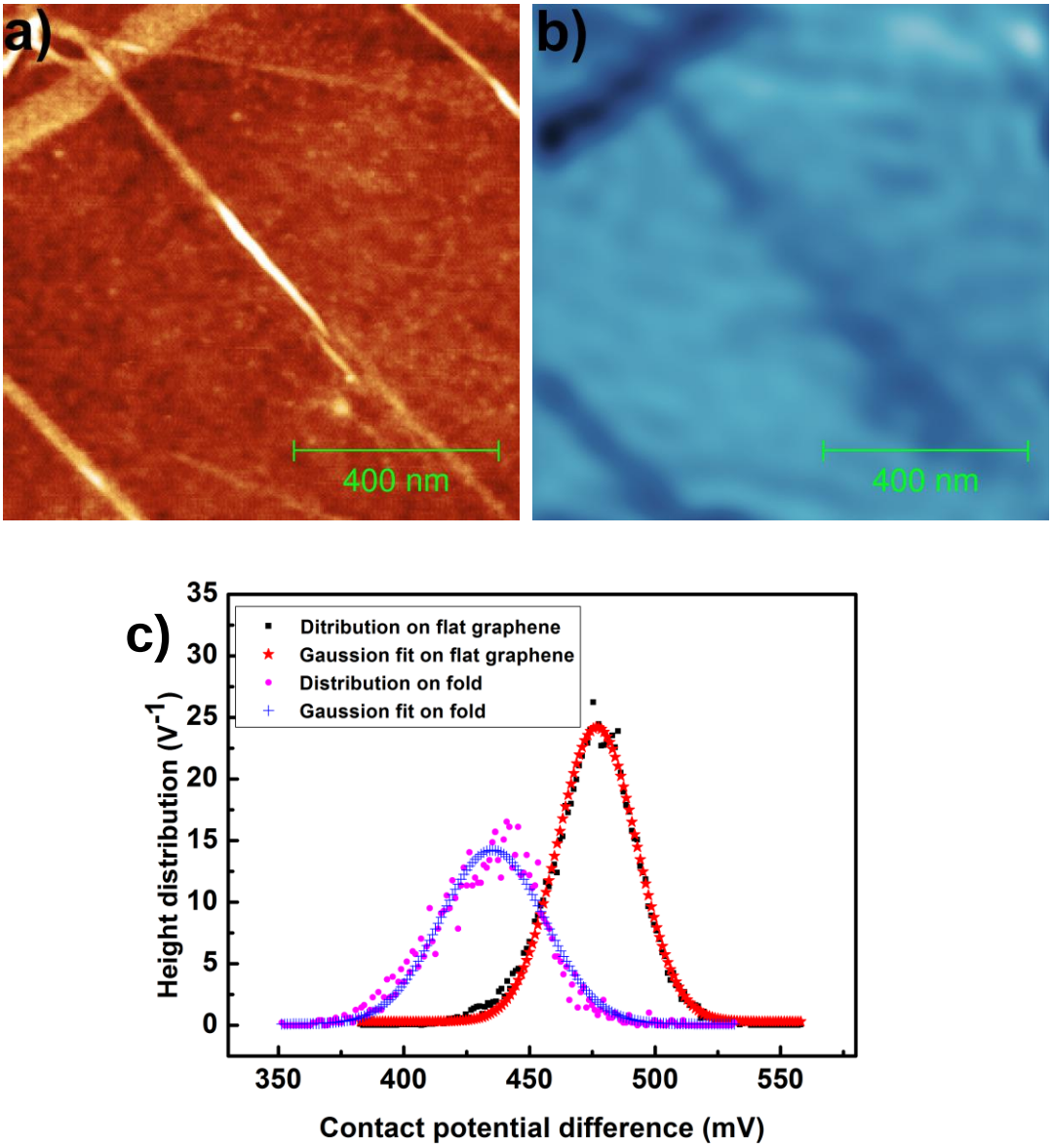

Fig. 4.11: a) A 1×1 μm^2 AFM image of graphene with grafolds height of 1.5 nm. b) shows 1×1 μm^2 KFM image of Fig. 4.11a. c) represents the plot for contact potential difference on flat graphene region (black squares) and is fitted with Gaussian function (red stars). Contact potential difference on folds is represented with pink circles and is fitted with Gaussian function (blue plus).

4.3 Conclusion

We have examined the nucleation phase of the growth of pentacene on a graphene surface that was characterized by grafolds, and compared the resulting morphology with the growth of pentacene under identical growth conditions on SiO_2. Our atomic force micrographs reveal a three-dimensional growth mode on the graphene surface, which is at variance with the two-dimensional growth on SiO_2. We have also found that at the intersection of grafolds the growth rate is substantially increased. We suggest that the grafolds attract the incoming pentacene molecules through the increased chemical reactivity and through the increased roughness of the graphene surface. This has been further proved by KFM measurements that grafolds have different contact potential than unfolded graphene. By measuring the contact angle of several liquids on graphene we have found that its surface exhibits a relatively small contribution of the polar energy. This is consistent with a weak interaction of the pentacene molecules with the graphene lattice increasing thereby the probability of three-dimensional growth mode.

5 Pentacene on graphene: differences between single layer and bilayer

5.1 Introduction

Interest in graphene, a single layer of hexagonally coordinated carbon atoms, stems from its unusual electronic properties that are a consequence of graphene's peculiar two-dimensional structure, comprising two identical carbon atoms per unit cell [1]. A second layer of graphene that is placed above the first one, exhibits an altered electronic structure, relative to a single-layer graphene. For example, such bilayer graphene exhibits a non-zero electron energy gap at the K point of the Brillouin zone. The variance of properties of BLG relative to SLG is a consequence of the interaction of graphene with the underlying substrate [132]. SiO_2 is a ubiquitous substrate for studying the properties of graphene. This is because its dielectric constant is suitable as a gate-dielectric in graphene-based thin-film transistor prototypes. Fabry-Perot interferences also allow direct observation of graphene flakes on 100 nm and 300 nm –thick SiO_2 layers. In addition, transfer of exfoliated graphene onto SiO_2 results in relatively flat and defect-free graphene layers.

Transfer of exfoliated graphene onto SiO_2 is frequently performed under ambient conditions, which implies that the surface of SiO_2 is characterized by one or more layers of water molecules that attach to the silanol (SiOH) groups, which are the most common form of bound hydrogen on thermally grown SiO_2 [133]. Morphological and electronic properties of graphene on such surfaces are therefore influenced by the dipole electric field that originates from water molecules. It has been shown both theoretically [133, 134] and experimentally [45] that dispersive forces dominate the interaction between a graphene sheet and SiO_2. Sabio et al. [134] published a detailed analysis of several possible electrostatic interactions between graphene layers and the underlying SiO_2. Their findings indicate the importance of the interaction energy between the graphene layers and a water layer on top of the substrate. Such interactions exhibit a z^{-3} dependence on the distance from the surface z, and the

magnitude of the interaction is on the order of 1 meV/Å^2. Such rapid decay of the interaction strength suggests that only the first graphene layer is significantly affected, while leaving the second and subsequent layers relatively intact [135]. Short-range interactions that are typical for SiO_2 surfaces are easily disrupted by SLG. As pointed out in the recent study of wetting transparency of graphene by Rafiee et al. [136], on such systems the behavior of a substrate relative to the adhesion of overlayers is not preserved if SLG is deposited onto it. Break-down of wetting transparency of SiO_2 upon deposition of graphene was further confirmed in Ref. [137] with measurements of water contact angle on graphene transferred onto SiO_2 that was subjected to various treatments, including as-grown SiO_2 such as ours. Li et al. [138], on the other hand argued that the observed wetting transparency may be a signature of graphene contamination by airborne hydrocarbons.

The interaction of graphene layers with the substrate alters their surface energy. Surface energy of graphene is reportedly 2.91 meV/Å^2, and was determined by measuring contact angles of various polar liquids on graphene on SiO_2 [139]. The experiments in Ref. [139] included chemically exfoliated graphene from reduced graphene oxide transferred onto SiO_2 in air by dropping a drop of aqueous solution of exfoliated graphene flakes. The flakes thickness ranged from 0.8-1.6 nm, suggesting that SLG and few-layer graphene was used in the experiment. Furthermore, the use of aqueous solution implies that the measured surface energy reflects the contribution of interfacial water molecules. Since the formation of the water-graphene interface costs energy, the surface energy of the graphene sheet on SiO_2 is lower than the surface energy of a freestanding graphene. Assuming the z^{-3} dependence of the electrostatic interaction with water molecules, the contribution of water molecules to the interaction energy at the surface of the second graphene layer that is separated from the first for 0.3 nm is only ~ 0.06 meV/Å^2. Moreover, surface energy of the second and subsequent graphene layers is completely dominated by the interlayer interactions that can reach values as high as 30 meV/Å^2 [123, 132, 140]. Based on these findings, we conclude that the surface energy of the first layer of graphene on SiO_2 is significantly *lower* than the surface energy of the second and subsequent layers.

Consequently, we expect that thermodynamic and kinetic conditions for nucleation and growth of overlayers on the first graphene layer are different from those at the second and subsequent layers. Indeed, as we are showing in this study, morphology of pentacene islands in the coverage range explored, exhibits important differences

between SLG and BLG. Pentacene has been in the focus of intense research in the past few years, mostly because of its promise in the high speed organic thin film transistors [141]. In the quest of improvement of charge carrier mobility, considerable effort to understand the initial stages of growth of pentacene has been invested. Most of the work focused on pentacene growth on SiO_2 or polymeric substrates, and extensive review of the matter may be found in Ref. [142]. It now well established that under suitable conditions pentacene forms two-dimensional islands on variety of substrates.

5.2 Experimental

We have used ex-situ non-contact AFM to examine the samples prepared by vacuum evaporation of pentacene on graphene at a base pressure of 10^{-8} Torr. The substrate temperature (T_s) was varied in the range from 10 °C to 60 °C. Nominal thickness and deposition rates were measured in situ by quartz crystal monitor, and the deposition rate was 0.5-0.7 nm/min. The substrates included SLG and BLG obtained by exfoliation of Kish graphite and transferred onto SiO_2 under ambient conditions. Measurements of the height difference between the first graphene layer and the substrate yielded a value of 0.9±0.1 nm, which is a typical value obtained, when a monolayer of water is present between graphene and SiO_2 [143-145]. Selected samples comprising SLG and BLG flakes were annealed at 350 ºC for 3 h in Ar atmosphere prior to pentacene deposition. Several SiO_2 substrates were also covered by HMDS that was deposited by spincoating. Onto these substrates graphene was transferred using the same protocol as on the non-treated SiO_2 substrates.

To obtain graphene, we have exfoliated graphene from KISH graphite (NGS Naturgraphit GmbH) using NITTO tape. Purchased Graphite flakes of few mm in size can be used to exfoliate graphene of hundreds of microns in size. Initially, first graphene was isolated with scotch tape. However later, NITTO tape is preferred because it leaves less residues on graphene flakes as compared to Scotch tape. Hence, graphene obtained with former is cleaner than with Scotch tape. The procedure of exfoliation has been followed as shown in Fig. 5.1. Before exfoliation, the substrate is cleaned in acetone, isopropanol and in (H_2SO_4: H_2O_2) for 10 minutes in each.

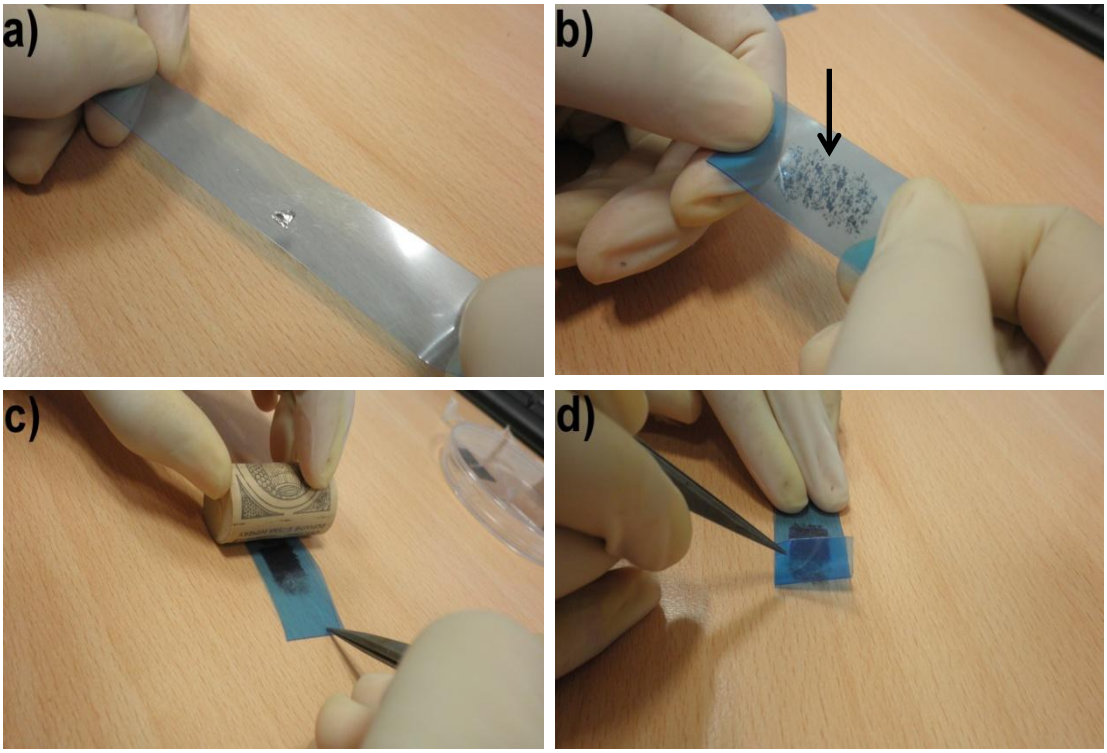

Fig. 5.1: Exfoliation of graphene using NITTO tape

A thick graphite flake is put in the middle of the tape as shown in image Fig. 5.1a. It is exfoliated several times so that we get thinner layers as shown in Fig. 5.1b). The Fig.5.1b shows the transparent region with some thin layers on the tape as indicated by an arrow. We use a roller to press the tape against the substrate uniformaly (Fig. 5.1c). Then, the tape is raised very slowly so that graphene is adhered to the substrate (Fig. 5.1d). With this procedure, exfoliated single-layer graphene flakes are accompanied by few-layer graphene (FLG) flakes. The obtained flakes are first observed with optical microscope.

Fig. 5.2 shows the optical microscopy image of SLG, BLG and tri-layer graphene (TLG) flakes. SLG, BLG and TLG flakes transferred onto SiO_2 substrate are indicated with arrows in Fig. 5.2a. Fig. 5.2b shows a 20×20 μm^2 AFM image of the same flakes as shown in Fig. 5.2a. The SLG, BLG and TLG regions are indicated in the AFM image.

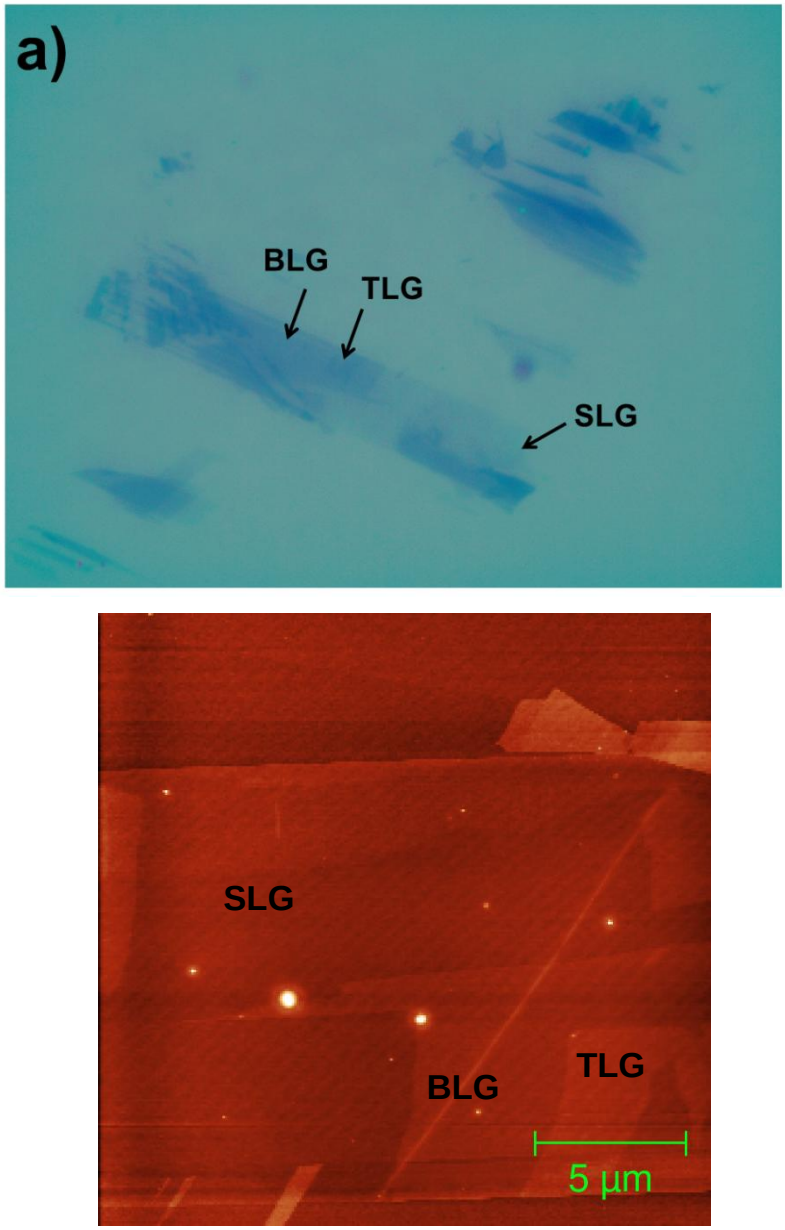

Fig. 5.2 Micromechanically exfoliated graphene transferred onto 300 nm-thick SiO_2. a) shows an optical microscopy image of single-layer, bilayer and trilayer graphene flakes marked with arrows. b) shows a 20×20 μm^2 AFM image of the same flakes as shown in optical image. Flake containing single layer, bilayer and trilayer graphene regions is indicated on the images.

5.3 Results and discussion

Fig. 5.3 exemplifies the topographic AFM image of a pentacene layer deposited at 10 ºC (Fig. 5.3a) and at 30 ºC (Fig. 5.3b) and at 60 ºC on SLG (Fig. 5.3c) and on BLG (Fig. 5.3d). Qualitative observation shows that the size of the islands on a SLG exceeds the size of the islands on BLG. In addition, we observe strong dependence of

the island size on the substrate temperature. Comparing Figs. 5.3(a-c), we see that the island size increases with increasing substrate temperature. Note also the onset of nucleation of the second and third layer. Here we will not discuss in depth the nucleation of the subsequent layers, but only mention that our recent experiments show that the onset of the nucleation of the second and subsequent layers is extremely sensitive to variations in molecular flux and T_s. Areal density of the second layer nuclei is more pronounced on BLG than on SLG, and decreases with increasing T_s. We also note, that morphology of pentacene layer on graphene is considerably different from the morphology on SiO_2 (also shown in Fig. 5.3). The islands on SiO_2 are considerably smaller for all T_s and exhibit more fractal shape, as already reported in several previous works [27, 91, 113]. Compactness of the islands is a signature of reversibility of the molecule aggregation process in the sense that individual molecules may detach from the island and diffuse along its perimeter (edge diffusion) resulting in smoother perimeter of the islands. From the height of the islands (1.5 nm) we conclude that the molecules are oriented almost perpendicular to the surface as in thin-film phase [23]. This puts graphene into the group of materials where molecule-substrate interaction is relatively weak and does not involve charge transfer that would result in flat-lying molecules on the surface. In order to initiate edge diffusion, pentacene molecules must break intermolecular bonds within the existing island and overcome the energy barrier for edge diffusion. The energy barrier for edge diffusion comprises the energy of bond formation with a given number of neighbors within the outer edge of the island, and the energy barrier for surface diffusion within the capture zone of the island, i.e. the area within which the molecules are preferentially attracted to the island. The latter depends on the molecule – substrate interaction energy. For stronger molecule – substrate interactions the edge mobility is reduced and the islands exhibit increasingly dendritic morphology. For a given molecular flux and a given substrate temperature, pentacene islands on weakly interacting substrates will therefore exhibit more compact shape. From the comparison of the shape of the islands on SiO_2 and graphene, we can conclude that the molecule – substrate interaction on graphene is weaker than on SiO_2.

On graphite the orientation of pentacene molecules is reportedly parallel to the surface, as determined by grazing-incidence x-ray diffraction and scanning tunnelling microscopy [120]. Growth proceeds in 2D elongated islands. An upright orientation of molecules was obtained on graphite that was Ar-sputtered prior to the pentacene

growth, suggesting that roughness has a role in determining the orientation of the molecules. Two-dimensional growth of an organic semiconductor has been observed also by Wang and Hersam [146], who used molecular-resolution STM to investigate submonolayer coverages of PTCDA on epitaxial graphene grown on the SiC(0001) surface. Their study focuses on the PTCDA-graphene interaction on the molecular level and shows that PTCDA molecules interact relatively weakly with the underlying graphene.

Considering the coverage of only first layer of pentacene, we observe that coverage increase with temperature from $\theta = 0.55$ at 10 ºC to $\theta = 0.68$ at 60 ºC.

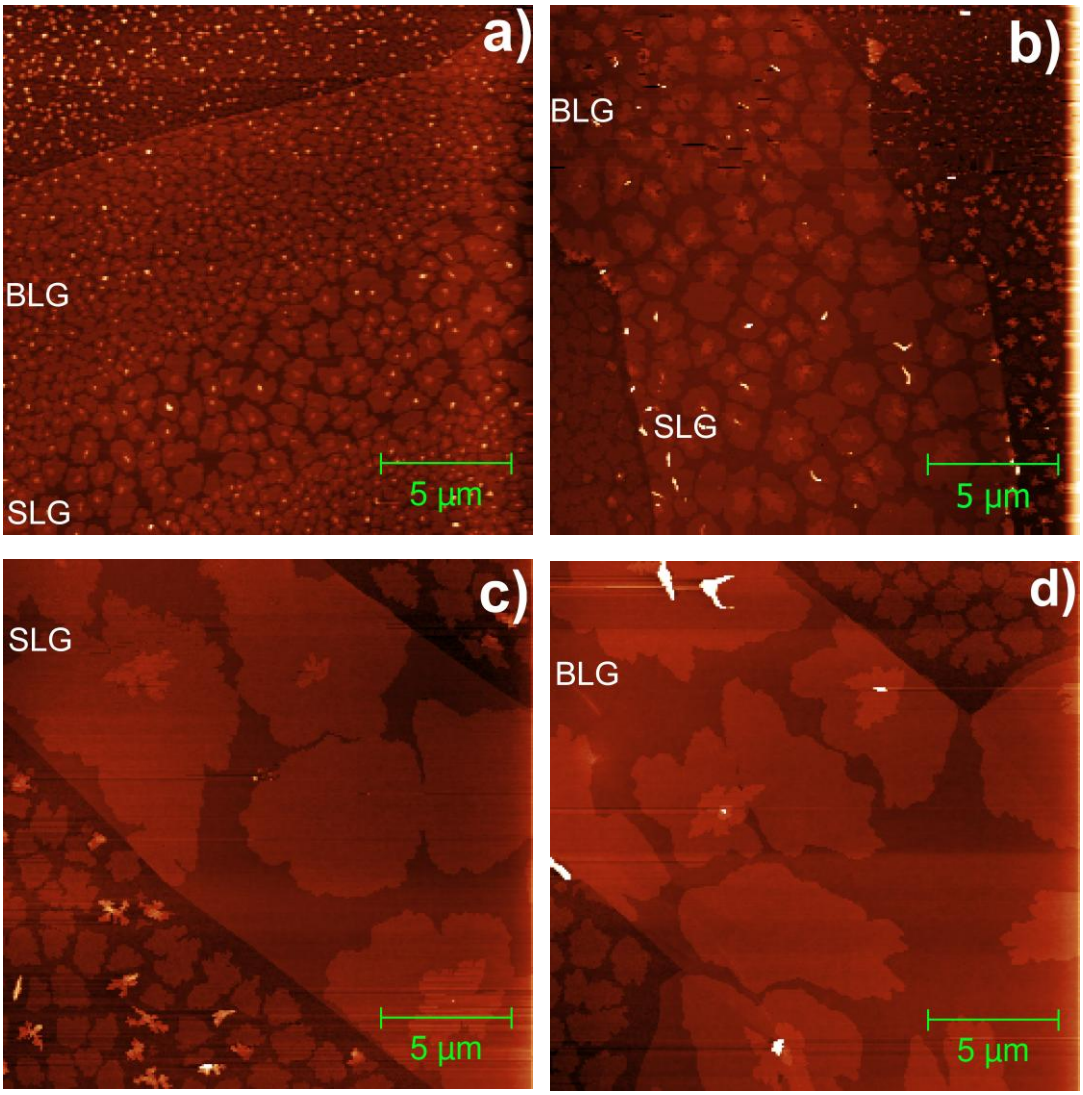

Fig. 5.3: Atomic force microscopy topography images of submonolayer coverage of pentacene on exfoliated graphene. Indicated are regions of a SLG, BLG and SiO_2. The images correspond to different substrate temperatures (T_s) during pentacene growth: (a) T_s =10 °C, (b) T_s = 30 °C, (c) T_s = 60 °C on SLG. (d) T_s = 60 °C on BLG. The pentacene molecular flux was the same in both cases.

We also note that by increasing the evaporation time it is possible to achieve full coverage. This is shown in Fig. 5.4, which shows pentacene grown on SLG (Fig. 5.4a) at 60 ºC under the same molecular flux as submonolayer coverages and with extended growth time. A full coverage can be obtained on FLG at the same substrate temperature (Fig. 5.4b). The deposition time was increased to get full monolayer at T_s = 60 °C as islands on BLG are smaller than on SLG (Fig. 5.3c and Fig. 5.3d.)

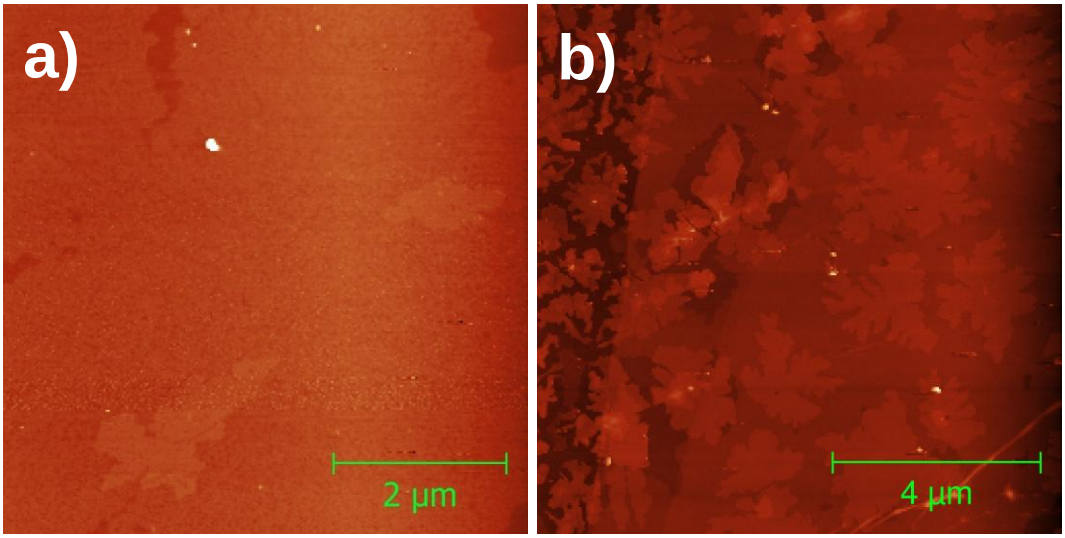

Fig. 5.4: Atomic force microscopy topography of a complete coverage of pentacene on a) exfoliated single layer graphene. The image size is 6x6 µm^2. The pentacene layer was grown at substrate temperature 60 ºC. The height of the pentacene layer (brighter tones) is 1.5 nm. Fig. 5.4b shows the full pentacene coverage at FLG at the same temperature. Image size is 10x10 µm^2.

Focusing on the temperature dependence of the size of the islands we observe two different regimes of island growth. On the high temperature side of the explored temperature interval, for T_s = 50 ºC and 60 ºC, the island size is comparable to dimensions of a graphene flake, their size is therefore equivalent to the system size. This regime is referred to by Amar and Family as a percolation regime [92]. For $T_s \leq$ 40 ºC, instead, most of the islands are considerably smaller that the system size, and certain (temperature-dependent) portion of the islands start coalescing. The contact area between some of the islands is still relatively small so that the original constituents are easily discernible. Such islands can be separated into sub-islands that can be considered as the signatures of the original nucleation sites [147]. No nucleation of new islands is expected in this regime, as the island capture zones are

almost of the same size as the pertinent islands. The arriving molecules can therefore land onto an existing island or become immediately aggregated to it at the suitable kink site. Depending on the ratio between the molecular surface diffusion (D) and deposition rate (F), this is the regime in which growth of the second or third layers is observed. This is a consequence of the diffusion length, approaching the average grain size. The temperature range explored in our work therefore spans the transition region between the two regimes.

Based on the monomer-deposition model [92], in this region the island density exhibits an abrupt change of dependence on coverage. The density of stable islands is significantly reduced and the density of monomers starts increasing. This behaviour importantly depends on D/F ratio. In our experiments the molecular flux was kept constant, i.e. F was fixed. Variation of the substrate temperature influences molecular surface diffusivity D, which also depends on the surface energy of graphene. As outlined in the second and third paragraph in Section 5.1, the surface energy of graphene varies with the number of graphene layers. We expect that the island density, as a function of temperature, i.e. D/F ratio, exhibits different behaviour on SLG and on BLG.

The evidence of different temperature dependence of island size distribution (ISD) on SLG and BLG is demonstrated in Fig. 5.5, where we show ISD for SLG (Fig. 5.5, top) and BLG (Fig. 5.5, bottom) for $T_s \leq 40$ ºC. We see that for both types of substrates ISD broadens with increasing temperature. This behaviour is consistent with the dependence of the island density distribution with coverage [91, 92, 147]. Indeed, as we show in the pertinent insets of Fig. 5.5, the coverage depends on the substrate temperature. Circles in both insets represent the coverage obtained by calculating the area of the first-layer-islands only, while the squares represent the coverage of the second layer only. We see that the coverage of the first layer increases with temperature, while the coverage of the second and subsequent layers decreases for both types of substrate. As the substrate temperature is increased, the probability of pentacene molecules to diffuse over the edge of the island increases. Since in the coverage range explored, the capture zones of the islands are of almost the same size as the islands, the molecules reaching the top edge of the islands become immediately aggregated to the islands. The probability for nucleation of the second layer therefore decreases, and the growth rate of the first layer increases.

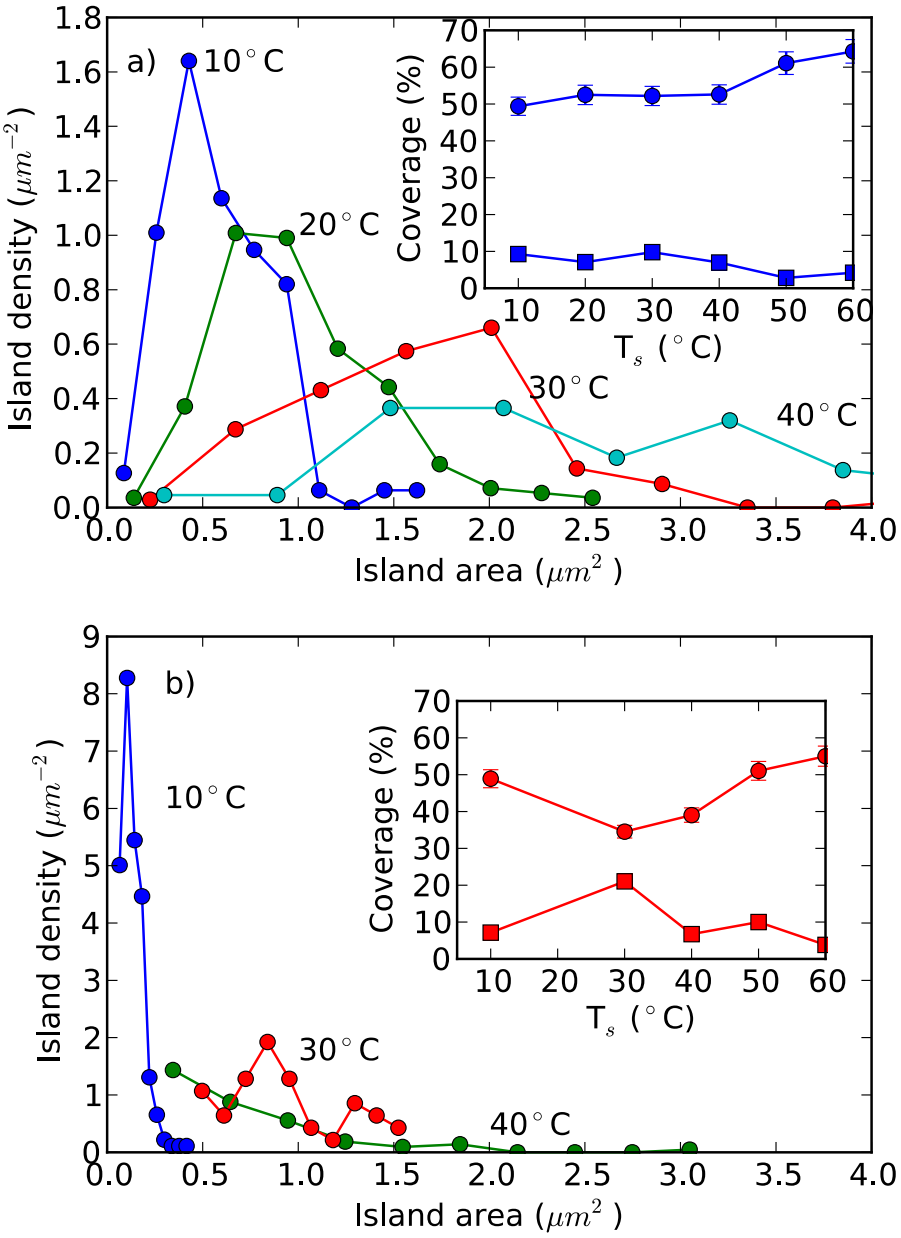

Fig. 5.5: Island size distributions of pentacene islands on exfoliated graphene transferred onto SiO_2. (a) Data for single layer graphene at different temperatures. (b) Data for bilayer graphene at different temperatures. Both insets show the coverage of pentacene layer obtained by taking into account only the island of the first molecular layer (circles) and only the second molecular layer (squares). The coverages are reported as percentage of covered areas of the individual graphene flake.

Shifting of the centroids of ISDs to larger average island areas, coupled to the distribution broadening observed in Fig. 5.5 suggest that dynamic scaling (DS)

principle could be applied. DS implies (see Section 3.2) that the island size distribution ($N_a(\theta)$) varies with coverage as [91, 92, 147]:

$$N_a(\theta) = \theta A^{-2}(\theta) f(u)$$

where θ is the coverage, a is the island area, A is the average island area and $f(u)$ is the scaling function. Plotting of $\frac{N_a(\theta)A^2(\theta)}{\theta}$ would therefore result in a series of curves superimposed one over the other. We have examined this possibility, and found out that the distributions for 10 ºC and 20 ºC scale well. Distributions obtained at higher temperatures, however, deviate considerably from the dynamic scaling behaviour. Within the growth regime explored in our experiments dynamic scaling of the island size distribution [89, 92, 148] no longer applies, due to the island coalescence and second layer nucleation and growth. Island size distributions presented in Fig. 5.5 clearly demonstrate that the molecular dynamics on the surface of SLG and of BLG is substantially different. On SLG we observe distributions that are consistently broader and centered at larger values of $A(\theta)$ for all temperatures than on BLG. The width of the island size distribution is an indication of the size of the stable clusters. Kinetic Monte-Carlo simulations as well as bond-scission model predict smaller stable clusters in the nucleation phase of the layer growth usually result in broader distributions [147]. We can therefore conclude that on SLG the initial stable cluster size is smaller than on BLG, which is a consequence of reduced surface energy on SLG relative to BLG.

The two substrates exhibit different behaviour also if we plot the island density (*N*) as a function of inverse temperature (Fig. 5.6). In this plot the island density is decreasing with increasing temperature mostly due to the island coalescence. The substrate temperatures are still too low for significant desorption. Two distinct regions in *N*(1/T) that are separated at temperatures around 50 ºC are observed. The transition between them indicates the onset of rapid coalescence, when the island size approaches the system size. The islands enter the percolation regime. Each impinging molecule is aggregated to a kink site at the edge of the islands and the rate of nucleation of the second layer is reduced, causing an increase in coverage of the first layer (see the insets in Fig. 5.5). While for temperatures higher or equal to 50 ºC only two data points preclude reliable data analysis, several data points obtained at lower

temperatures allow us to perform a least-squares fitting to extract the activation energy for island nucleation. Fitting to the exponential function above the transition region SLG and BLG exhibits markedly different behaviour. The activation energies resulting from the fits are 0.29 eV and 0.52 eV for SLG and BLG, respectively. We see that in the pre-percolation regime the surface energy plays an important role in island coalescence. On BLG the coalescence is facilitated, as the surface energy is higher than on SLG.

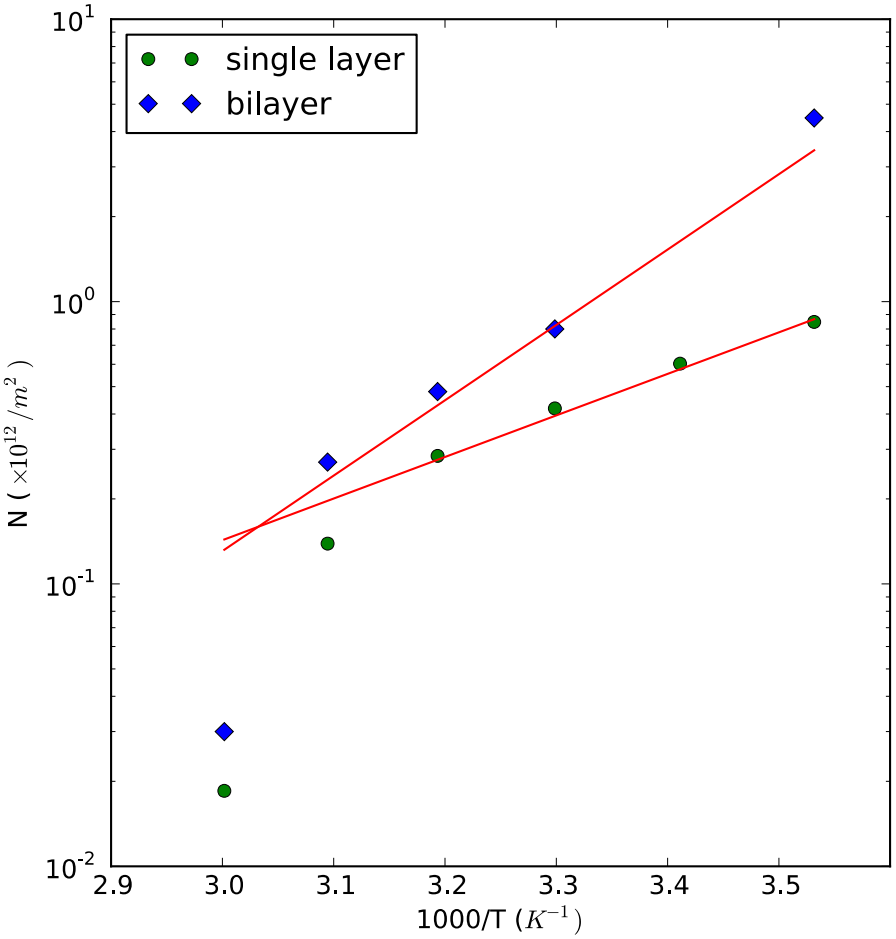

Fig. 5.6: Density of pentacene islands (N), grown on exfoliated graphene, as a function of inverse substrate temperature. Circles represent the data obtained on single-layer graphene. Diamonds represent the data obtained on bilayer graphene. Solid lines represent least-squares fits to an exponential function $N \propto e^{\frac{E_a}{kT}}$, where E_a is the activation energy for coalescence of the islands.

Focusing on the mean island area (⟨A⟩) presented in Arrhenius plot for SLG (circles) and BLG (squares) in Fig. 5.7, we can again see considerable difference between the

two types of substrates. Straight lines are least-square fits to and exponential function: $\langle A \rangle \propto e^{-\frac{E_a}{kT}}$, and yield activation energy for island growth. We have calculated activation energy as E_a= -427±25 meV for SLG, and E_a= -537±46 meV for BLG. Such difference in E_a again suggests more favourable kinetic conditions for island growth on SLG relative to BLG.

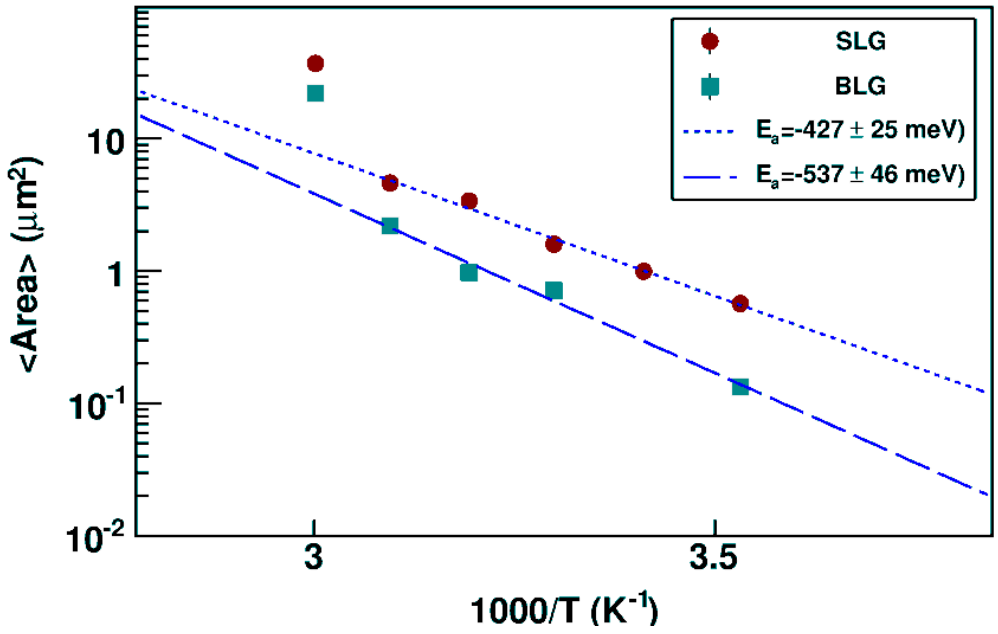

Fig. 5.7: Mean area of the pentacene islands on exfoliated graphene as a function of inverse substrate temperature. Dashed and solid lines represent least-squares fits to an exponential function $\langle A \rangle \propto e^{-\frac{E_a}{kT}}$, where E_a is the activation energy for the island growth.

Comparing Fig. 5.6 and Fig. 5.7, we note that they are closely related, and support the hypothesis of reduced molecular mobility at lower temperatures and that surface energy of BLG is higher than that of SLG. Firstly, from Fig. 5.6 we see that as the temperature is lowered the number of new nuclei increases, arguing for lower surface mobility of pentacene molecules. In addition, the difference in activation energy between SLG in BLG argues for higher nucleation rate of new islands on BLG. Secondly, Fig. 5.7 shows that the effect of lowering the substrate temperature is a reduction of average island area, which, under the absence of re-evaporation, is a consequence of increased number of nucleated islands. Further, larger activation

energy for growth of the islands on BLG argues for higher surface energy on BLG relative to that on SLG.

As we suggested in the Introduction the interface water layer with the associated dipole field may be responsible for altered growth conditions present on the surface of SLG and BLG. In order to examine further this hypothesis we have explored the morphology of pentacene layers on two types of substrates, which should contain no interfacial water layer. The first type of substrates included annealed graphene on SiO_2. The annealing temperature of 350 ºC and time (3 h) were chosen in order to maximize the evaporation of water molecules from the interfacial region. The second type of substrates included HMDS-covered SiO_2. HMDS self-assembled-monolayer is frequently used to render SiO_2 surface hydrophobic [149]. On the two types of substrates we have deposited pentacene whose nominal thickness was 1.3 nm and 1.7 nm, on annealed and on HMDS-treated samples, respectively. The topography scans of these samples are shown in Fig. 5.8. Fig. 5.8a shows the morphology of pentacene deposited on annealed graphene, and Fig. 5.8b shows the morphology of pentacene deposited on graphene that was transferred onto HMDS-treated SiO_2.

In the case of annealed substrate we see that initially pentacene grows in 2D mode, however before the first layer is completed, 3D islands start to grow. The final surface is characterized by 15 nm-high elongated islands that reside on the uncompleted first monolayer. Similarly, in Fig. 5.8b we observe almost exclusively 3D growth mode of pentacene on graphene with 25 nm-high elongated islands. In addition, we consistently observed preferential orientation of the islands on this type of samples. The preferential orientation might be a signature of underlying HMDS orientation, and needs further investigation. These experiments further support the hypothesis that the interfacial conditions strongly affect morphology of pentacene on graphene. In both cases the amount of water molecules prior to the deposition of pentacene is strongly reduced relative to the as-transferred graphene, and in both cases the pentacene layer is characterized by three-dimensional islands.

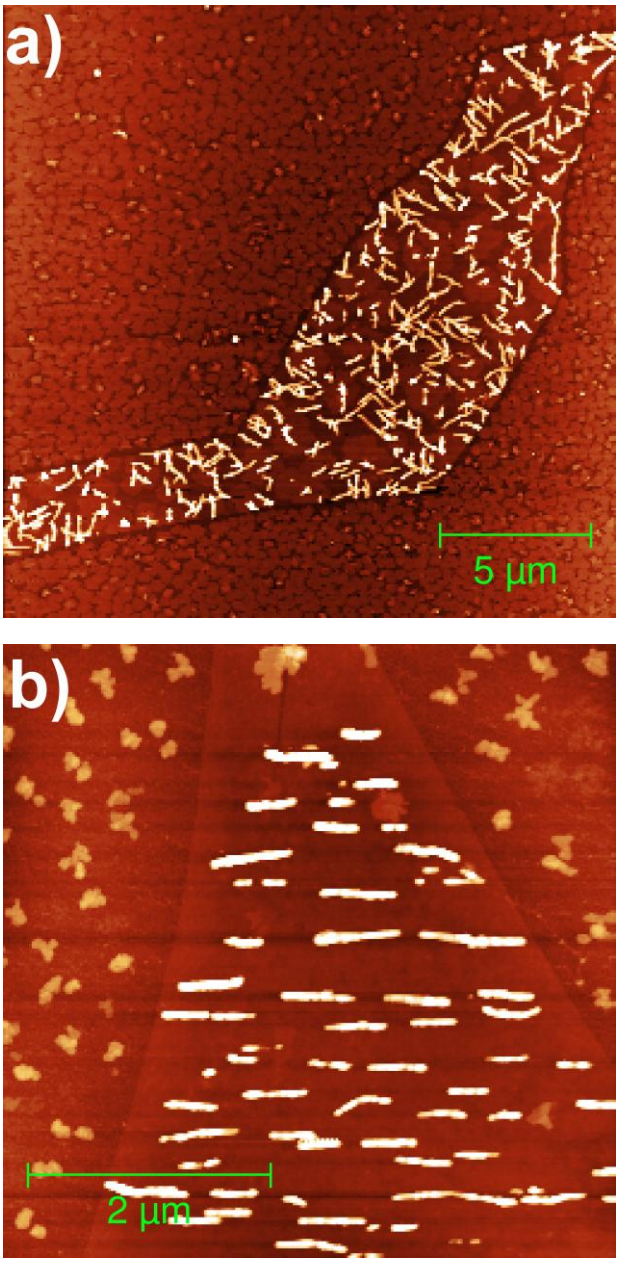

Fig. 5.8: a) 20×20 µm^2 AFM micrograph of pentacene on single layer graphene on SiO_2. The substrates were annealed at 350 ºC for 3 hours in Ar atmosphere prior to the pentacene deposition. b) 5×5 µm^2 AFM micrograph of pentacene on single layer graphene on SiO_2. SiO_2 substrate was treated with HMDS prior to graphene transfer.

Statistical quantities such as island density and island area are also dependent on the number of graphene layers. Fig. 5.9 shows the plot for mean area of islands and mean island density as a function of number of graphene layers. Substrate temperature was

kept constant (T_s = 60 °C) during pentacene growth. We have observed that mean island area decreases with number of graphene layers (Fig. 5.9a). It is highest for SLG (37±5 μm^2) and then decreases sharply on BLG (22±1 μm^2) and FLG (18±1 μm^2). The transition from SLG to BLG is exemplified by the AFM images shown in Fig. 5.3c and 5.3d). On the other hand, island density increases sharply from SLG to BLG and to FLG and is represented in Fig. 5.9b. Island density is lowest on SLG. Island density is reduced due to enlarged grain area in accordance with the Ref. [91, 92].

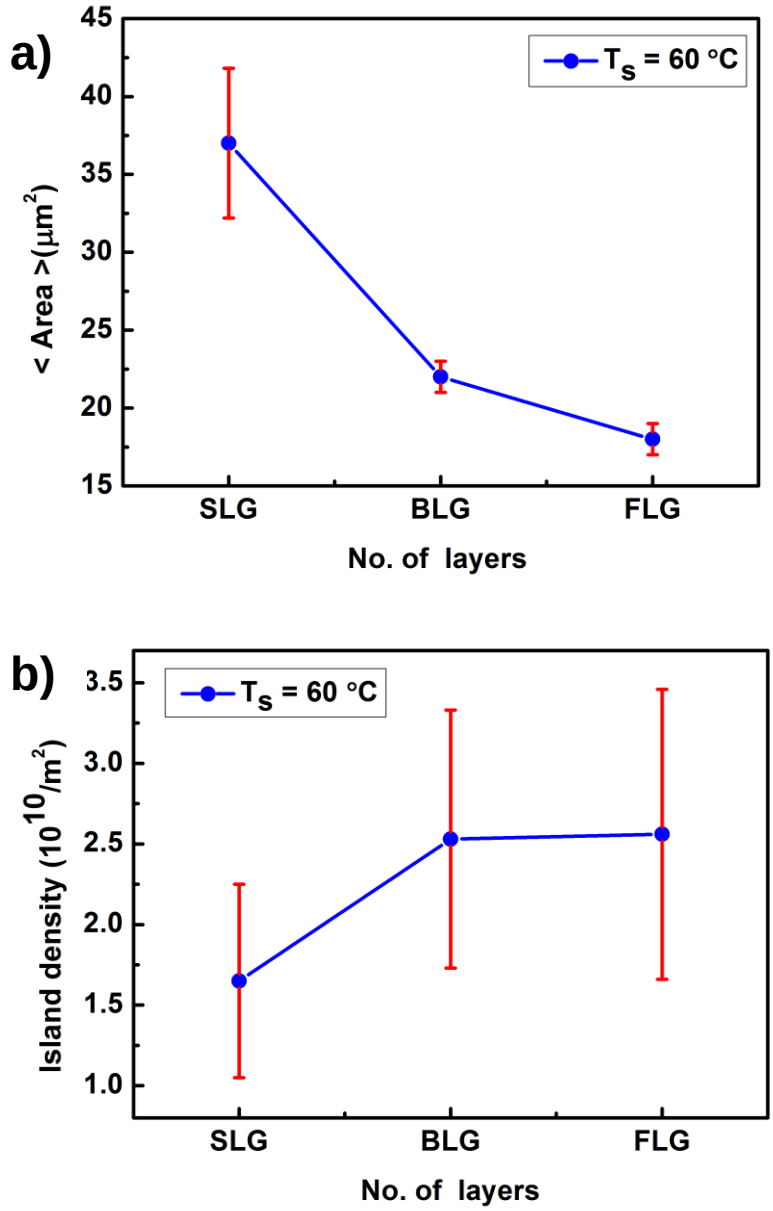

Fig. 5.9: a) shows the variation of mean grain area of pentacene islands on SLG, BLG and FLG at T_s = 60 °C. b) represents the plot for island density as a function of graphene layers at the same substrate temperature. Red line in Fig. 5.9a and 5.9b shows the error bar on the mean island area and mean island density respectively.

Island density and island area are related as $N = \theta/A(\theta)$. Since mean island area is smaller on BLG and FLG, islands density is higher. Mean island density is $(1.65\pm0.6)\times10^{10}$ m^{-2}, $(2.5\pm0.8)\times10^{10}$ m^{-2} and $(2.55\pm0.9)\times10^{10}$ m^{-2} on SLG, BLG and FLG respectively. Similar behaviour has been observed at other substrate temperatures (T_s= 10 °C, T_s= 30 °C, T_s= 50 °C). However, behaviour of metals (Au and Ag) on graphene layers is different than that of organic molecules. Liu et al. [150] have observed the behaviour of gold atoms on graphene layers and graphite. They have found that mean island area of gold nanoparticles increases with number of graphene layers. This is due to the fact that diffusion constant for SLG is smaller than that for multilayer graphene.

Fig. 5.10 shows the histogram for probability distribution of pentacene islands on SLG and BLG films at different substrate temperatures. The distributions are plotted at four different substrate temperatures (T_s = 10 °C, T_s = 30 °C, T_s = 50 °C and T_s = 60 °C) for SLG and BLG respectively in Figs. 5.10(a-d). We have applied three tests to compare the distributions on SLG and BLG flakes. First, quantile-quantile (q-q) plot, which is used to compare the two probability distributions by plotting them against each other. Quantiles refer to the points taken at regular intervals from a distribution function of a random variable. A point (x,y) on the plot corresponds to one of the quantile of the second distribution (y-coordinate) that is plotted against the same quantile of the first distribution (x-coordinate). If the data follows the distribution, then the points on the q-q plots falls on a straight line. Others tests are Anderson – Darling (A–D) test and Kolmogorov – Smirnov (K–S) test. These tests are employed to test weather two probability distributions belong to a specific distribution.

Fig. 5.10a shows the histogram of probability distribution at T_s = 10 °C on SLG and BLG which shows that pentacene on SLG has higher island area than BLG and its distribution is broader than on BLG. We have used q-q plots coupled with histograms to check whether the underlying data is normally distributed. The inset shows a q-q plot which is plotted by dividing by mean values (mean area of islands) and compared the probability distribution of area of islands on SLG and BLG. As seen from the plots, most of the data points (collected from SLG and BLG) fall on the linear curve (inset Fig. 5.10a). The linear behaviour of the data points in the q-q plot argues that the islands of pentacene belong to the same distributions on SLG and BLG at T_s = 10

°C. Probability (p) is ~ 50% as tested by A–D test and ~ 46% K–S test for data of SLG and BLG (inset Fig. 5.10a). Probability p in the inset is different than the probability distribution p(a) of island area in Fig. 5.10. This shows that there is ~50% probability that islands at two different graphene layers belong to same distribution. K–S test also show that there is 46% probability that they do not belong to the same distribution at T_s = 10 °C.

Similarly, Fig. 5.10b) shows the histogram for probability distribution at T_s = 30 °C for the islands on SLG and BLG respectively. With increasing substrate temperature, islands area also increases on SLG and BLG respectively in comparison to that at T_s = 10 °C. Island area is higher on SLG than on BLG at same temperature. Probability p is very high (p~98% and p~99%) as tested from A–D and K–S test at T_s = 30 °C. High p values are due to low number of pentacene islands. Fig. 5.10c and Fig. 5.10d represents the probability distribution for T_s = 50 °C and at T_s = 60 °C on SLG and BLG respectively. Hence, due to low number of islands statistics is relatively poor. It is difficult to predict the exact behaviour at these temperatures. However, q-q test shows that the probability distribution on SLG and BLG is identical. If the resulting plot is a linear curve from both samples, then the two samples have normal distribution. Any deviation from the straight line indicates the deviation from the normal distribution.

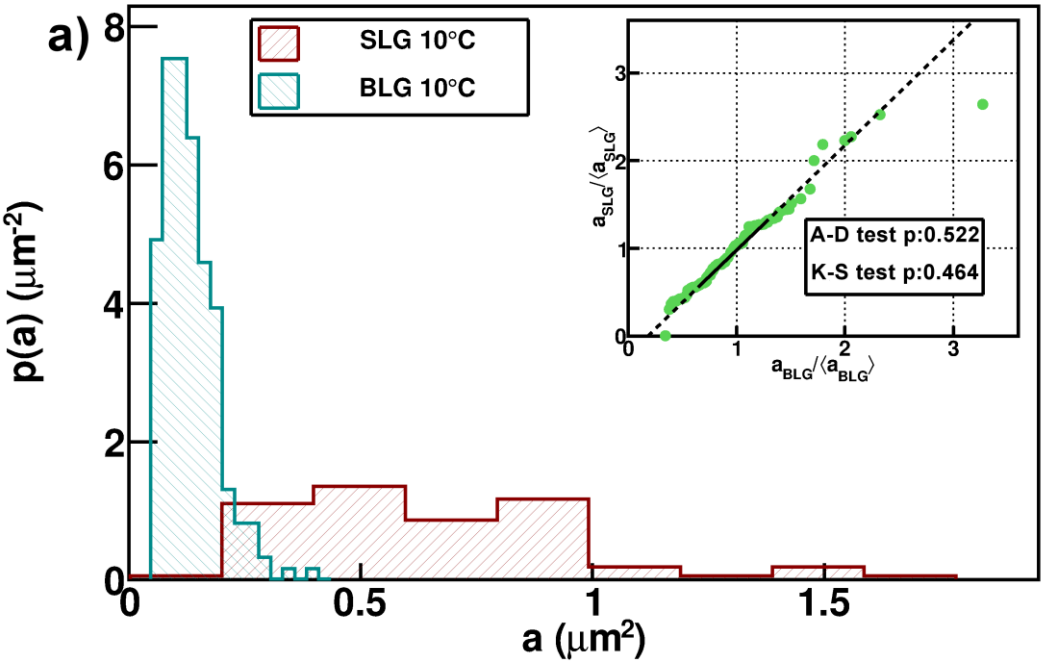
a)
SLG 10°C
BLG 10°C
A-D test p:0.522
K-S test p:0.464
p(a) (μm-2)
a (μm2)
aSLG/⟨aSLG⟩
aBLG/⟨aBLG⟩

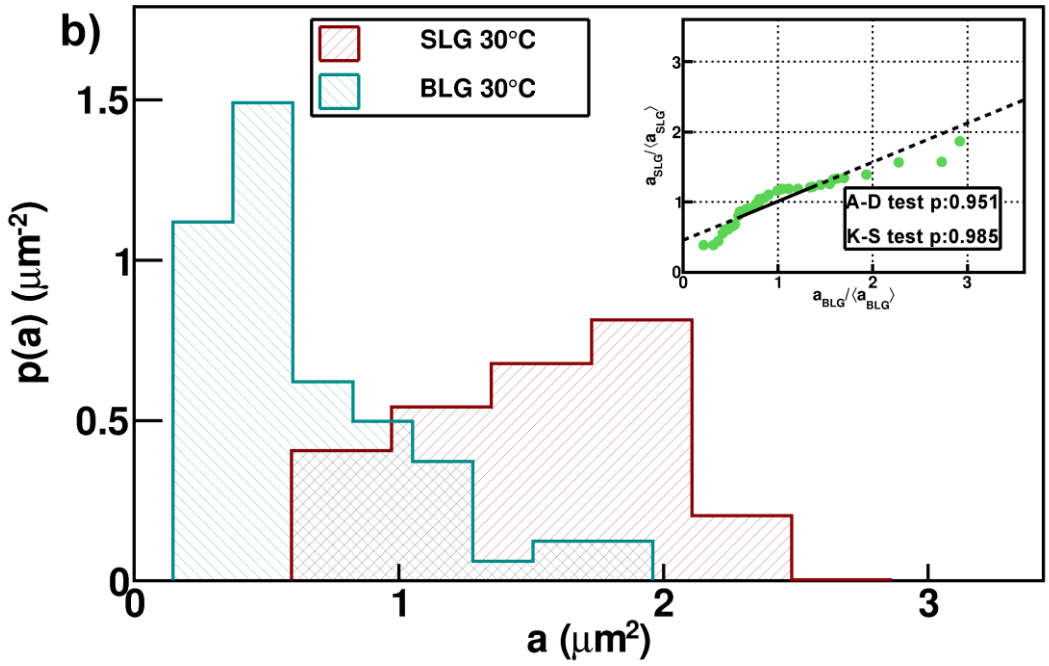
b)
SLG 30°C
BLG 30°C
A-D test p:0.951
K-S test p:0.985
p(a) (μm-2)
a (μm2)
aSLG/⟨aSLG⟩
aBLG/⟨aBLG⟩

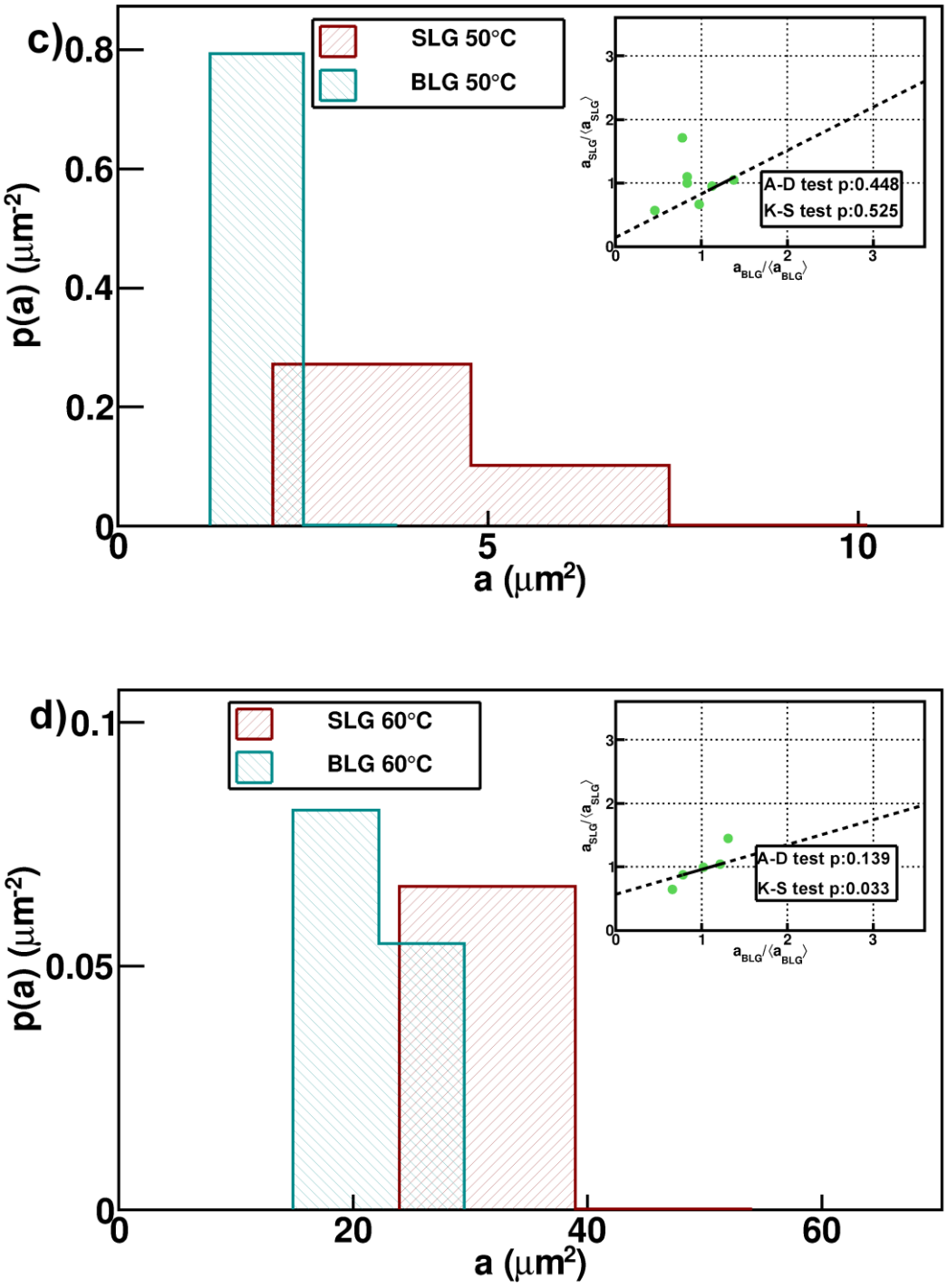

Fig. 5.10: Probability distributions of the area of pentacene islands on SLG and BLG at substrate temperatures a) T_s = 10 ˚C, b) T_s = 30 ˚C, c) T_s = 50 ˚C and T_s = 60 ˚C. Insets show the Anderson–Darling test and Kolmogorov–Smirnov) test for SLG and BLG. Data points corresponding to SLG and BLG are plotted against each other (green circles). a_{SLG} and a_{BLG} denotes the island area on SLG and BLG respectively.

We have also studied fractal dimensions of pentacene islands on SLG and BLG respectively. Shape of the islands is an interesting geometrical property. Fractal geometry (shape) is used to describe the characteristics of the ramified islands. One quantitative measure of the structure of islands is their fractal dimension. Fig. 5.11 shows the fractal dimensions (d_f) plotted as a function of substrate temperature on SLG and BLG respectively. Temperature range was from 10 °C to 60 °C.

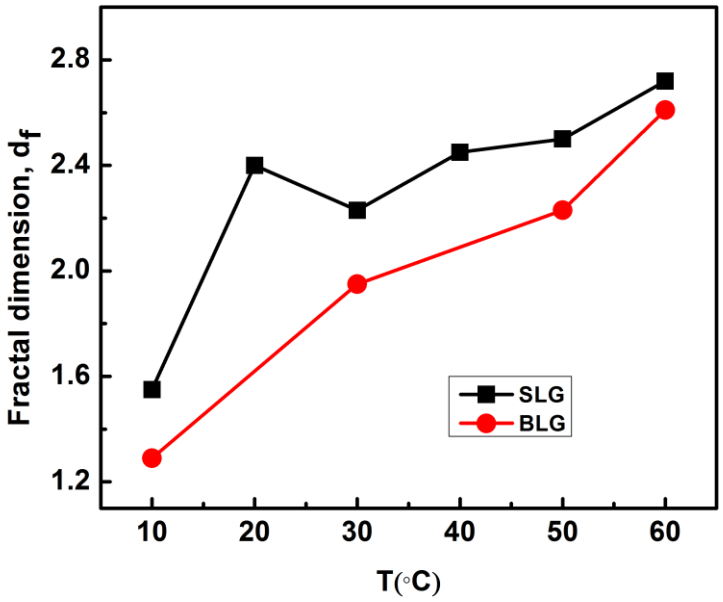

Fig. 5.11: Fractal dimensions of pentacene islands on SLG (black line and squares) and BLG (red line and circles).

In DLA regime [92], coverage (θ) is less than 0.5 and fractal dimension is in the range $1 \leq d_f \leq 2$. From Fig. 5.11, on SLG at T_s =10 ˚C, fractal dimension is 1.55 which is similar to the DLA regime. Fractal dimension on BLG is ~1.3 at the same substrate temperature. Coverage is also less than 0.5 at T_s =10 ˚C on both SLG and BLG. Hence, pentacene islands at relatively low temperature as T_s =10 ˚C have fractal dimensions that are similar to that of diffusion mediated growth [91]. Shape of the islands in DLA is controlled by the possibility of the molecules to reach to the islands via random motion. However, d_f increases with the increase in substrate temperature as observed from Fig. 5.11. New islands are not formed and molecules are attached to the edges of the existing islands.

5.4 Conclusion

Our AFM investigation of the initial stages of growth of pentacene on graphene indicates that on SLG and BLG pentacene grows in two dimensional islands that are considerably larger than those on SiO_2 deposited under the same conditions. There are considerable differences in morphology of pentacene on SLG and BLG, however. The island size distributions are broader and centered at bigger island areas on SLG than on BLG. The activation energy for molecular aggregation was found to be E_a= 427±25 meV for SLG, and E_a= 537±46 meV for BLG. We associate this behavior with the influence of the dipole electric field that stems from the interfacial water layer that is present between graphene and SiO_2, and reduces surface energy of SLG in comparison with BLG. Island area decreases and island density increases with number of graphene layers. The probability distribution for island area on SLG and BLG are identical. In addition, the fractal dimension at lower substrate temperature (10 °C) is similar to the DLA growth regime on SLG and BLG. However, fractal dimension no longer corresponds to DLA regime at higher temperatures.

6 Effect of water layer at SiO_2/graphene interface on pentacene morphology

6.1 Introduction

Graphene has demonstrated its potential in a variety of electronic and optoelectronic applications. It can be used as an electrode replacing to indium tin oxide (ITO) in organic solar cells [51] and its 2D network may serve as a template for growth of organic molecules [151-153]. Graphene can be used as a substrate to enhance the Raman signal of adsorbed organic molecules on its surface that are deposited by vacuum evaporation or by solution processing [154]. Study of growth of small organic molecules such as pentacene on graphene is not only interesting for fundamental research, but is also important for optimization of graphene-based devices [7]. Performance of these devices is significantly affected by overgrown thin layers which act as charge transporting layer. Pentacene growth has been studied thoroughly on dielectric substrates such as SiO_2, metals, PMMA [13, 155]. However, relatively few reports are available focusing growth of pentacene on graphene where pentacene exhibits a less ordered growth [120, 156]. Pentacene morphology on graphene surface may be sensitive to the underlying substrate [149]. Lafkioti et al. [148] observed that adsorbed molecules from the ambient air can cause a doping resulting in poor performance of graphene-based devices. P-type doping was observed due to adsorption of water molecules on underlying substrate. Treatment of the substrate with HMDS prior graphene transfer can screen the effect of water molecules. In addition, annealing the SiO_2/graphene can be effective in removing the water layer. However, annealing can modify its surface or electronic properties either by heavy doping or producing strain in graphene films depending on the annealing conditions [157]. In this chapter, we have studied the inital stages of growth of pentacene on exfoliated SLG flakes. Our results show that pentacene morphology is significantly different on as prepared graphene and annealed graphene surfaces. Also, a different morphology is observed when underlying substrate is treated with HMDS. Resulting morphology is a consequence of competition between intermolecular and

substrate–molecule interactions, which in turn are sensitive to the surface chemical and structural properties of underlying substrate [157]. Hence, we focused on studying the effect of the treatment of underlying substrate and the annealing impact on final morphology of pentacene.

6.2 Experimental

SLG samples were exfoliated from KISH graphite and transferred onto Si wafers with 300 nm thick SiO_2 layer as described in Chapter 5 in Fig. 5.1 [145]. The size of the exfoliated flakes was several hundreds of μm in size. The single-layer thickness of graphene was confirmed by Raman spectroscopy and by AFM. Selected samples were annealed in Ar atmosphere at 350 °C for 3 hours. The height of as-transferred (pristine) graphene flakes on SiO_2 was found to be 1±0.1 nm while the height of annealed samples was 0.5±0.05 nm. Raman spectra were recorded with Jobin Yvon T6400 Raman system in micro Raman configuration. The excitation wavelength from Ar^+/Kr^+ ion gas laser was 514.5 nm (2.41eV). Laser power was kept below 1mW with 50× microscope objective lens to avoid the sample degradation from laser induced heating. Spectra were recorded at room temperature.

Submonolayer coverages of pentacene layers (Sigma Aldrich, purity > 99.8%) were evaporated on graphene samples in a high vacuum chamber at a base pressure of 10^{-8} Torr. Deposition was performed systematically in the range of $0.7 < \theta < 0.40$ and pentacene growth was examined at substrate temperatures of 29 °C and 60 °C. Coverage was monitored by in-situ quartz crystal thickness monitor that was calibrated by ex-situ AFM measurements. The nominal deposition rate was 1 nm/min. Molecular flux was kept constant in all the experiments. AFM in non-contact mode was used to characterize the morphology of pentacene layers. Detailed statistical analysis of the AFM images was carried out using Gwyddion software (gwyddion.net).

6.3 Results and Discussion

The surface morphology of pentacene evaporated on SLG is shown in Fig. 6.1 at T_s = 29 °C (Fig. 6.1a) and T_s = 60 °C (Fig. 6.1b). We have observed two-dimensional pentacene islands with an average height of 1.5±0.2 nm, which corresponds to the

thin- film phase of pentacene exhibiting interplanar spacing of 1.55 nm [78]. Fig. 6.1a shows that before completion of the first monolayer, there is significant second and third layer growth. Three-dimensional islands observed on the top of the first monolayer are 20 nm high. Island density of first monolayer islands is 38×10^{10} m^{-2} and mean island size is 1.2 µm. Mean island area is 1.6 μm^2. Final morphology is the result of balance between intermolecular and molecule – substrate interactions [158].

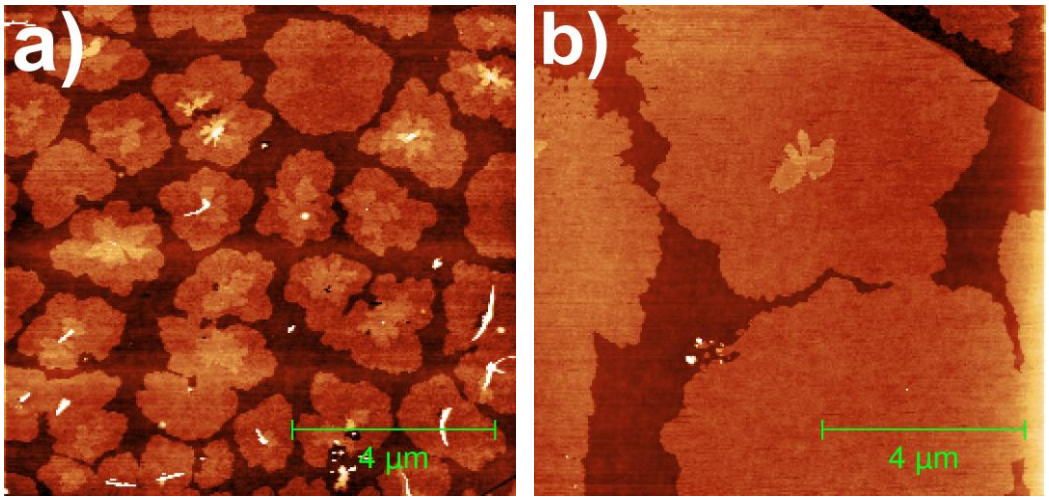

Fig. 6.1: A 10×10 μm^2 AFM image of pentacene islands on SLG flakes at substrate temperature a) 29 °C, b) 60 °C. Pentacene islands for first layer on pristine SLG sample have a typical height of 1.5±0.2 nm corresponding to thin film phase Fig. 6.1a. Increasing substrate temperature enlarges the islands form 1.6 µm to 6 µm in size as shown in Fig. 6.1b.

A 2D nucleation mode occurs when molecule – substrate interaction exceeds intermolecular interaction. In addition, morphology is likely to be influenced by the ambient species such as water layer present on the underlying substrate [45]. Since, graphene and SiO_2 have weak van-der Waals interactions, presence of water molecules between graphene and substrate may influence the interaction of pentacene molecules with graphene resulting in the morphology as shown in Fig. 6.1. Interaction energy of water molecules with the first graphene layer varies as z^{-3} and is of the order of ~ 1meV/$Å^2$ [132]. With increasing T_s to 60 °C (Fig. 6.1b), surface diffusion along the edges of islands is enhanced resulting in enlarged compact islands and reduced island density. Island density drastically decreases from 38×10^{10} m^{-2} (Fig. 6.1a) to 3×10^{10} m^{-2} (Fig. 6.1b) due to coalescence of islands. Mean island area increases from 1.6 μm^2 (Fig. 6.1a) to 37 μm^2 (Fig. 6.1b). Island density is minimum at T_s = 60 °C. Island size increases from 1.2 µm to 6 µm from substrate temperature 29 °C (Fig.

6.1a) to 60 °C (Fig. 6.1b) respectively. We did not observe any significant growth of the second layer at T_s = 60 °C.

We have deposited pentacene for 5 different coverages (θ) at T_s = 29 °C to study the statistics of islands of the type of Fig. 6.1a. AFM images in Fig. 6.2 corresponds to different coverages, θ = 0.07 (Fig. 6.2a), θ = 0.17 (Fig. 6.2b), θ = 0.37 (Fig. 6.2c), θ = 0.62 (Fig. 6.2d) and θ > 1 ML (Fig. 6.2e). Mean Island size is 300 nm at lowest coverage, θ = 0.07. With increasing coverage, incoming molecules are deposited on the existing islands. Islands are enlarged and mean island size is 500 nm (Fig.6.2b). Island size increases to 0.9 μm with a significant second layer growth of pentacene islands at coverage θ = 0.37 (Fig. 6.2c). Height of three-dimensional (3D) islands observed on top of the first pentacene layer is 20 nm. With increasing coverage, θ = 0.62, there is significant coalescence of the islands as shown in Fig. 6.2d. Island size increases to 1.2 μm.

Fig. 6.2e represents an AFM image with coverage higher than 1 monolayer (θ > 1ML). However, with increasing deposition time, there is no first full monolayer coverage. Before completing first monolayer, we observe significant second and third layer growth at T_s = 29 °C. There is also a significant growth of 3D islands. We also have observed that morphology of pentacene on graphene is substantially different than the islands on SiO_2 as indicated in Fig. 6.2c. Islands on graphene are considerably larger than the islands on SiO_2 for same θ and T_s. As we discussed in Section 4.2, graphene has lower surface energy (42 mJ/m^2) as compared to SiO_2 (66 mJ/m^2). Therefore, the difference in surface energy leads to the change in morphology. Moreover, pentacene islands on SiO_2 exhibit fractal shape (Fig. 6.2c). This type of fractal growth belongs to DLA regime. Ruiz et al. [90] have studied the dynamic scaling of pentacene islands on SiO_2. They suggested that pentacene on SiO_2 have diffusion mediated growth.

.

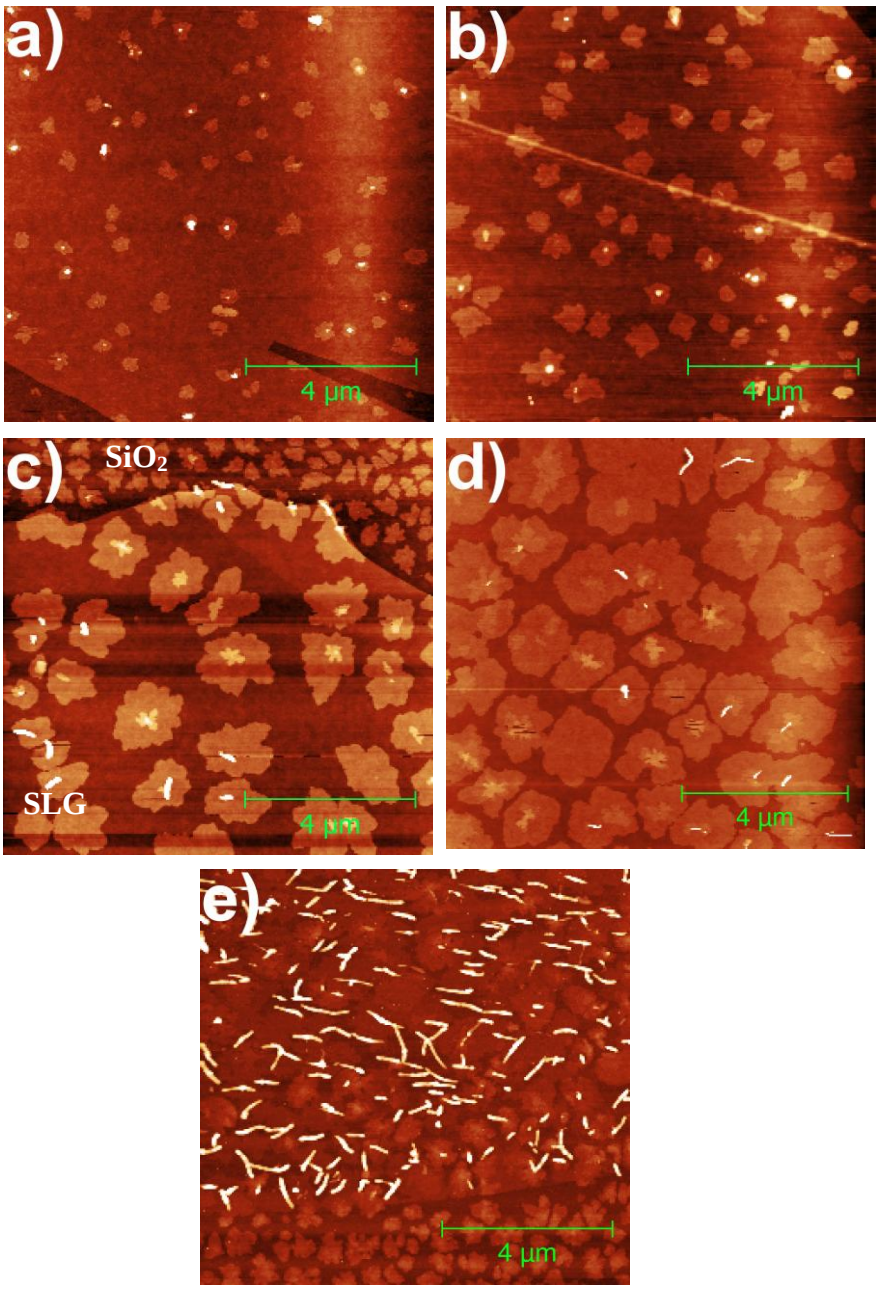

Fig. 6.2: AFM images of pentacene islands on single layer graphene for coverage a) θ = 7%, b) θ = 17%, c) θ = 37%, d) θ = 62% and e) θ > 1 ML (one monolayer) at substrate temperature T_s = 29 °C. Height of 2D islands is 1.5 nm and 3D islands are 20 nm high.

A plot in Fig. 6.3 shows the variation of island density, coverage, and island size with respect to deposition time for the morphology represented in Fig. 6.2. Fig. 6.3a shows that the islands density for the first monolayer of pentacene decreases exponentially with deposition time while increases for the second pentacene layer. Islands of first monolayer start to coalescence as deposition time increases and island density. At low coverage, it is in accordance with the relation, $\theta = Ft$. Coverage for the first

monolayer increases linearly with deposition time at constant flux (F) as can be seen from Fig. 6.3b. With increasing deposition time, islands occupy finite fraction of the substrate surface. On the other hand, coverage for higher layers does not show much increase with time except for deposition time of 150 sec. Fig. 6.3c shows a plot for grain size with respect to deposition time. We observe that grain size increases for first monolayer and 2nd layer pentacene islands with increasing deposition time. Incoming molecules are attached to the existing islands. That leads to increase in

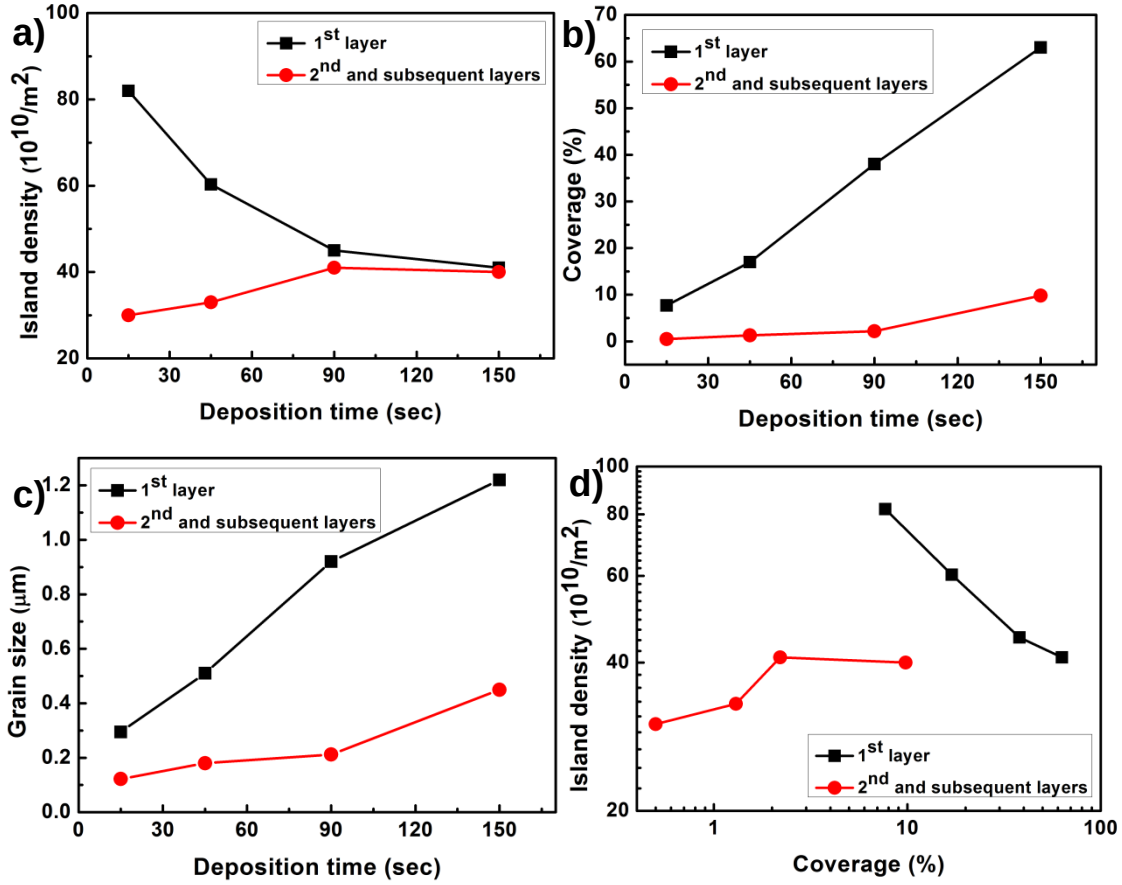

Fig. 6.3: Shows a) Islands density of pentacene islands on single layer graphene as a function of deposition time b) coverage and c) grain size as a function of deposition time respectively and, d) island density as a function of pentacene coverage.

grain size. Fig. 6.3d shows the plot for island density as a function of coverage. Island density decreases with increasing coverage. On the contrary, island density for second layer increases with coverage. At low coverage $\theta = 0.07$, island density is maximum (82×10^{10} m^{-2}). Island density decreases gradually to 60×10^{10} m^{-2} at $\theta = 0.17$, 44×10^{10} at $\theta = 0.37$ and 41×10^{10} m^{-2} at $\theta = 0.62$ respectively.

To study more quantitatively the growth dynamics of pentacene islands on graphene, we have analysed the scaling law of the pentacene ISD (see Section 3.2) in the coverage range $0.7< \theta < 0.40$. Statistical analysis of pentacene islands is represented in Fig. 6.4. Fig. 6.4a shows the island size distribution density ($N_a(\theta)$) for coverages of 0.07 (squares), 0.17 (circles), 0.37 (triangles). $N_a(\theta)$ is expressed in μm^{-4} and a in μm^{-2}. ISD was extracted from AFM images and plotted for different coverages. We observe from the distribution curve that position of the peak shifts towards higher values of island area. At the same time, height of the ISD decreases with increasing the coverage. Islands start to merge and island density decreases significantly. Average island size is small at low coverage ($\theta = 0.07$) and the distribution is narrow.

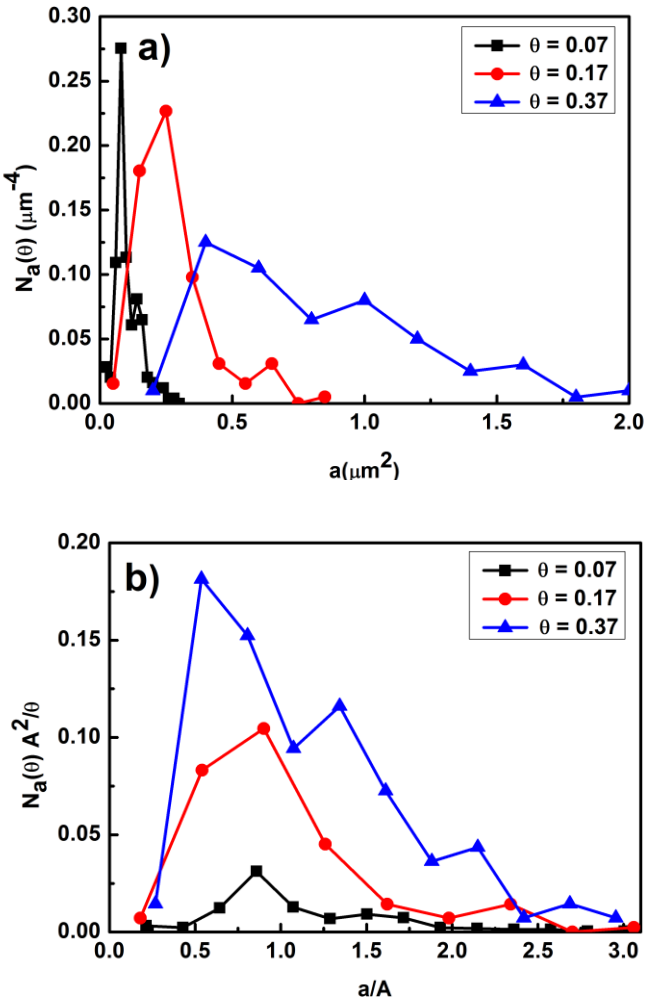

Fig. 6.4: a) Unscaled island size distribution N_a of pentacene islands for three different coverages of $\theta = 0.07$, $\theta = 0.17$ and $\theta = 0.37$. b) Scaled island size distribution, N_a for θ ranging from $0.07 < \theta < 0.37$.

With increasing θ to 0.37, ISD of the islands of size *a* broadens. Applying scaling law as expressed in equation (3.6), Fig. 6.4b represents the scaled island size distribution $\frac{N_a(\theta)A^2}{\theta}$ as a function normalized island size *a/A*. However, it does not follow the dynamic scaling theory [91]. Scaling theory is applicable for islands whose fractal dimensions are between $1 \leq d_f \leq 2$. Fractal dimensions observed for pentacene islands on graphene are greater than 2 as observed at room temperature.

Fig. 6.5 shows the AFM morphology of pentacene layer on annealed graphene at T_s = 29 °C (Fig. 6.5a) and 60 °C (Fig. 6.5b). The image obtained in Fig. 6.5a at T_s = 29 °C exhibits morphology of pentacene layers mostly as 3D islands. Average height of islands is 13 nm and average length is 0.8 μm. However, there is a significant growth of 2D islands. When pentacene is deposited at T_s = 60 °C, only 3D growth is observed (Fig. 6.5b). Hence, substrate temperature sets a limit to the growth of 2D islands as observed from the AFM micrographs. Observed height of 3D islands is 25 nm. Growth of first layer of pentacene can be strongly influenced by the underlying substrate. Graphene flakes exfoliated under ambient conditions have significant water layers between SiO_2 and graphene and/or on the graphene layer. Due to the presence of atmospheric species, thickness of graphene on SiO_2 is 1 nm and is in close agreement with the earlier reports [3, 45]. Therefore, this change in morphology can be attributed to the water layer that exists between SLG and SiO_2 due to weak van-der Waals interaction with SiO_2. Water molecules easily attach to the silanol group on SiO_2 and form a thin water layer. Annealing the graphene sample helps in depleting the water layer. Coupling between graphene and SiO_2 is stronger during annealing and graphene is adhered to the substrate. Thickness between graphene and SiO_2 reduces to 0.5 nm after annealing. Ishigami et al. [45] have estimated the interaction energy between graphene and SiO_2 of the order of 6 meV/Å^2 at the distance of 3.4 Å. This order of interaction energy is sufficient to overcome the energy barrier of corrugation that is required for graphene to adhere the SiO_2. This implies that there can be a change in surface energy of graphene that can lead to a 3D growth of pentacene islands on annealed graphene. Hence, water molecules underneath graphene film may be a significant cause for this change in morphology on as prepared graphene (Fig. 6.1a) and on annealed graphene (Fig. 6.5a). Also, a 2D morphology is governed by the strong molecule − substrate interactions. For the first

pentacene layer, molecules grow in standing-up orientation on graphene forming 2D monolayer islands as previously observed in Fig. 6.1.

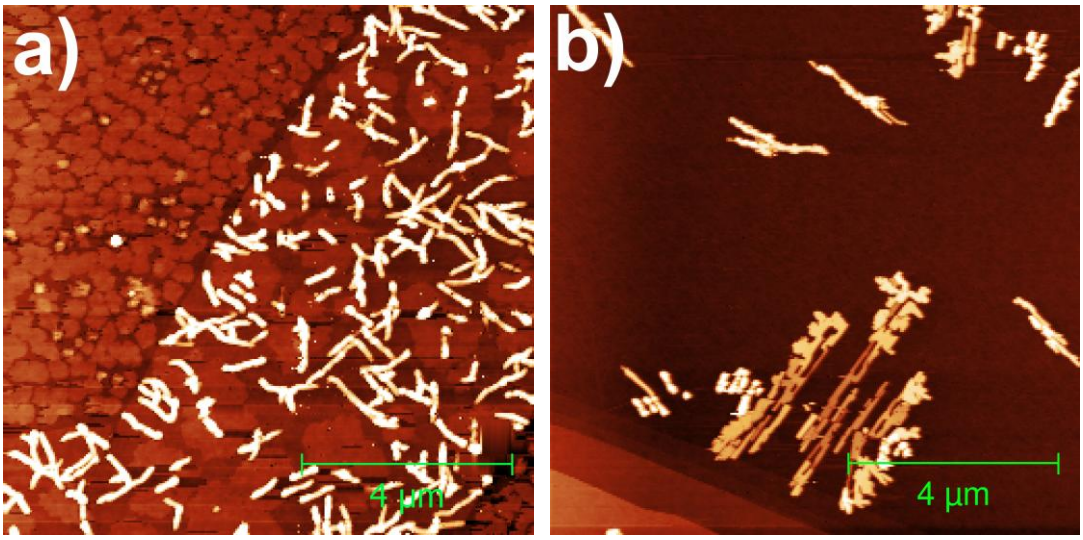

Fig. 6.5: 10×10 µm^2 AFM images of pentacene islands on SLG flakes annealed at 350 °C for 3 hours in Ar atmosphere at substrate temperature, T_s at a) 29 °C and b) 60 °C. Annealed graphene samples at 29 °C favor 2D pentacene islands than 3D in contrast with Fig.6.1a. Fig. 6.5b shows that at T_s = 60 °C pentacene has 3D islands with average island height of 25 nm.

To study the change in morphology of pentacene on annealed samples, we have compared the height distribution of as-prepared and annealed graphene samples prior pentacene. We have analysed the height histogram of the graphene layer on SiO_2 as represented in Fig. 6.6. Fig. 6.6 shows the height histogram over 250 nm ×250 nm regions of AFM images of as-prepared (black circles) and annealed samples (red circles). The distribution were fitted with Gaussian function with standard deviation (σ) of 0.13 nm and 0.17 nm for as-prepared graphene (red line) and annealed graphene samples (black line) respectively. The value of standard deviation describes the roughness of the surface. Therefore, a higher value of standard deviation on annealed graphene sample (0.17 nm) as compared to as-prepared graphene (0.13 nm) shows that graphene considerably follows the underlying SiO_2 substrate morphology after annealing. These values are in close agreement with those of the earlier reported in Ref. [159].

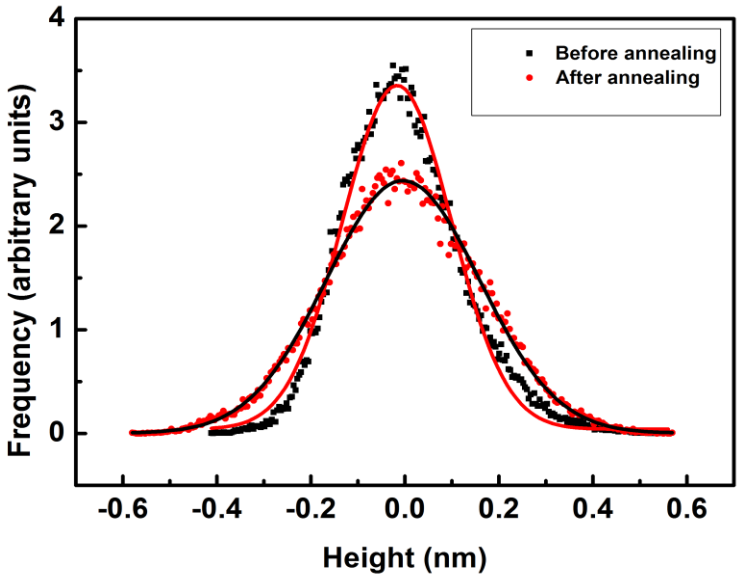

Fig. 6.6: Height distribution of as prepared graphene (black circles) and annealed graphene (red circles) prior to pentacene deposition. Both distributions were fitted with Gaussian function.

To illustrate further the impact of annealing on structural properties of graphene, we have carried out Raman spectroscopy of as prepared (pristine) and annealed graphene samples. Fig. 6.7a shows the Raman spectrum of the SLG before annealing (blue line) and after annealing (red line). Raman signatures, G and 2D bands were observed at 1583 cm^{-1} and 2677 cm^{-1} respectively for pristine graphene. G band originates from the bond stretching of all pairs of sp^2 atoms in both rings and chains [36]. 2D band is overtone of D band and is in a different in-plane vibration mode than G band [157]. The 2D band occurs due to the two phonons with opposite momentum in the highest optical branch near K point of the Brillouin zone. Absence of D peak in pristine graphene shows relatively ordered crystalline structure of graphene. We have not observed D peak even after annealing for 3 hours at 350 °C, which argues for stability of the crystal structure after annealing. Intensity of G and 2D bands decreases drastically and both the peaks broaden after annealing as shown in Fig. 6.7b and Fig. 6.7c respectively. Intensity ratio (2D/G) decreases from 3.0 to 2.0 after annealing. We have observed a blue shift of 7 cm^{-1} in G band and 11 cm^{-1} for 2D band after annealing as shown in Fig. 6.7b and Fig. 6.7c. Decrease in intensity and the shift in bands can be attributed to the doping of ambient O_2 molecules and compressive strain

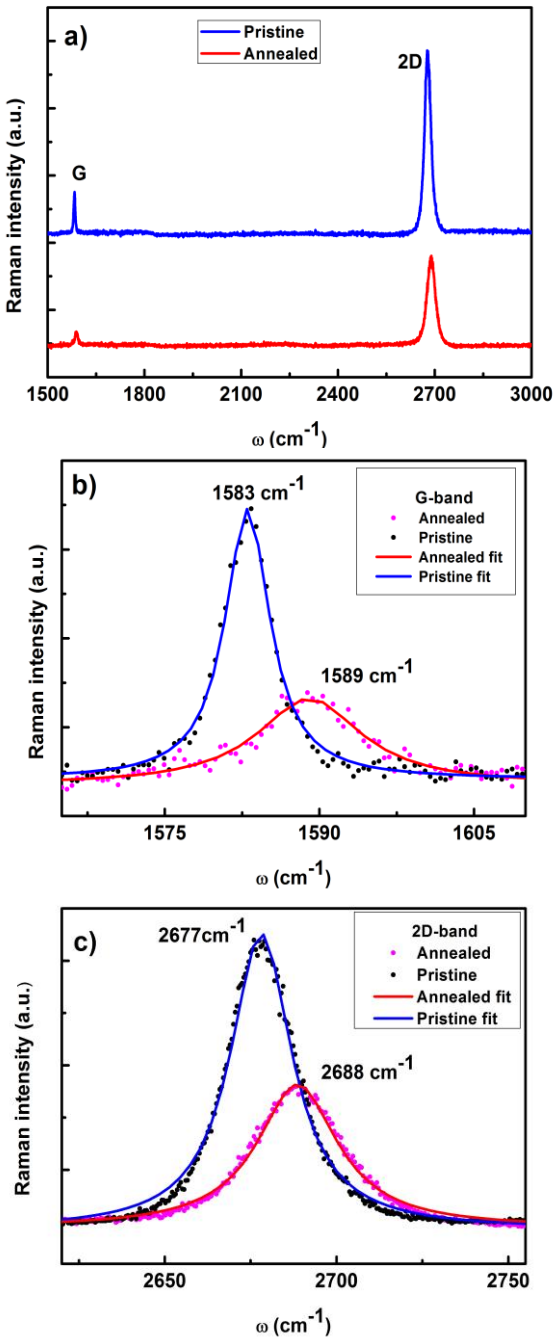

Fig. 6.7: Raman spectrum of SLG on 300 nm thick SiO_2 for a) pristine graphene (blue line) and annealed graphene (red line), b) shows the G band of pristine graphene (black circles) and annealed graphene (pink circles). Intensity of G band is fitted with Lorentzian function for pristine (blue line) and annealed graphene (red line). Fig. 6.7c) represents the intensity for 2D band on pristine (black circles) and annealed graphene (pink circles) fitted with Lorentzian distribution. Blue line is fit for pristine graphene and red line corresponds to fit for annealed graphene.

on graphene [160-162]. If shifts in G and 2D bands are close to each other, then shift is caused by doping of adsorption of NH_3, NO_2, H_2O, CO molecules causing charge transfer between graphene and adsorbed molecules [149]. Therefore, we can argue that doping and compressive strain exerted on graphene due to elimination of water layer at the interface can be a cause for shift and is in agreement with earlier reported papers [162, 163]. The G and 2D bands are well fitted with single peak Lorentzian function. G_{FWHM} (full width half maximum of G band) increases by $7cm^{-1}$ after annealing and $2D_{FWHM}$ (full width half maximum of 2D band) increases by 6 cm^{-1}. Ishigami et al. [45] suggest that van der Walls interaction energy of graphene strongly coupled to substrate is of the order of ~ 6 meV/Å^2 and is sufficient to produce a strain of few percent.

To further study the effect of underlying substrate, we have transferred the exfoliated graphene flakes on SiO_2 treated by HMDS prior to deposition of pentacene. Fig. 6.8 shows surface morphology of pentacene on SLG and graphene comprising many layers of graphene (many layers graphene-MLG). MLG flakes were also transferred on HMDS treated SiO_2 under same conditions as done for SLG. We have observed 3D growth on SLG (see Fig. 6.8a). Mean height of the islands is 25 nm and average island area is 0.026 μm^2. Island density on graphene surface is 4.4×10^{12} m^{-2} and coverage, θ is 0.11. HMDS eliminates the dipolar effect of water that exists between graphene and SiO_2 which results in 3D elongated pentacene islands on graphene [149]. HMDS apparently screens the graphene from the dipolar nature of water molecules. Therefore, graphene is transferred onto a Si-C-H system and is screened from influence of water molecules. However, this effect is negligible for pentacene deposited on thick MLG flakes under same conditions which have preferential 2D islands with height 1.5±0.2 nm and is same as that on untreated pristine graphene or graphite. This may be due to the change in surface energy of graphene due to interfacial layers.

Fig. 6.9a represents pentacene morphology on MLG. Island density is 4×10^{12} m^{-2} at $\theta = 0.08$. Mean island area is 0.75 μm^2. This shows that SLG is most sensitive to the substrate treatment while MLG surface remains unchanged. Fast-Fourier Transform (FFT) was employed on the images shown in Fig. 6.8a and Fig. 6.9a. Each of these grains was included in a two-dimensional Fourier transformation. Prior to calculation, a binary version of the AFM images was obtained where the region corresponding to

a selected pentacene island was set to value of 1 and the remaining region was set to zero to calculate mean background height of the image. Such mapping was then transformed into reciprocal space. FFT decomposes morphology data (information on position and height of individual points of the image) into its harmonic components, representing spectral frequencies present in the morphology data. A windowing function is used to suppress the data at the edges of the image.

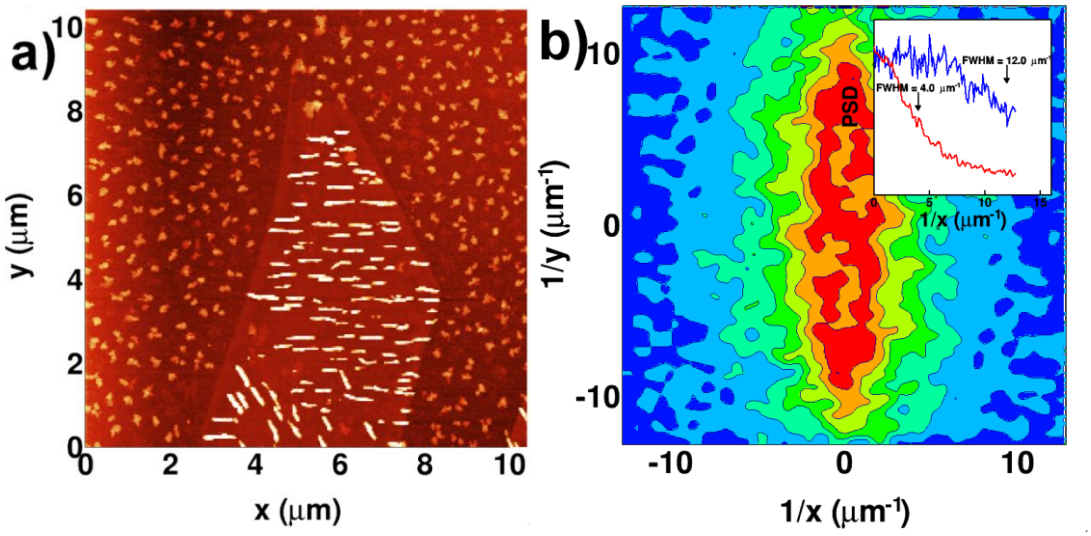

Fig 6.8: a) 5×5 μm^2 AFM image showing pentacene morphology on SLG/HMDS/SiO_2 at room temperature. The typical height of 3D islands is 25 nm. b) represents power spectral density function (PSDF) of pentacene islands on graphene. Inset shows the PSDF of pentacene as a function of radius along horizontal (red) and vertical (blue) direction.

Fig. 6.8b represents the results of FFT of Fig. 6.8a. The image presents the absolute value of the complex Fourier coefficient which is proportional to the square root of the power spectrum density function (PSDF). In an ideal case, when the islands are positioned on a regular grid and are oriented identically, the PSDF function can be devised as a product of PSDF of a single island and of PSDF of the grid. The fact is the consequence of the theorem that Fourier transform of a convolution is the product of Fourier transforms of the individual functions. Therefore, the PSDF of a single grain acts as an “envelope” to the final PSDF. In order to estimate the "envelope" of PSDF of Fig. 6.8a, we used Nadaraya-Watson kernel regression estimate to smooth the PSDF [164]. The resulting PSDF function (Fig. 6.8b) is highly anisotropic, reflecting the shape of pentacene grains. Based on this fact, PSDF in Fig. 6.8b is a

Fourier transform of an "average" single pentacene island. PSDF is elongated in vertical direction and rapidly decreases in horizontal direction. The vertical (horizontal) axis in reciprocal space corresponds to the horizontal (vertical) axis in the real space. The width and height of PSDF are calculated in the inset of Fig. 6.8b, where PSDF is presented as a function of radius along horizontal (red) and vertical (blue) direction. From the FWHM we estimate the length of pentacene islands in reciprocal space being 4 μm^{-1} (arrow on red curve) and corresponding to 500 nm in real space. In contrast, the calculation of width of pentacene grains is less accurate, since the PSDF exhibits relatively constant value over the whole distance. Extrapolating the PSDF with a normal distribution gives a rough estimate of FWHM of 12 μm^{-1} in reciprocal space. Using this rough estimate, we obtain approximately 40 nm as the width of pentacene islands.

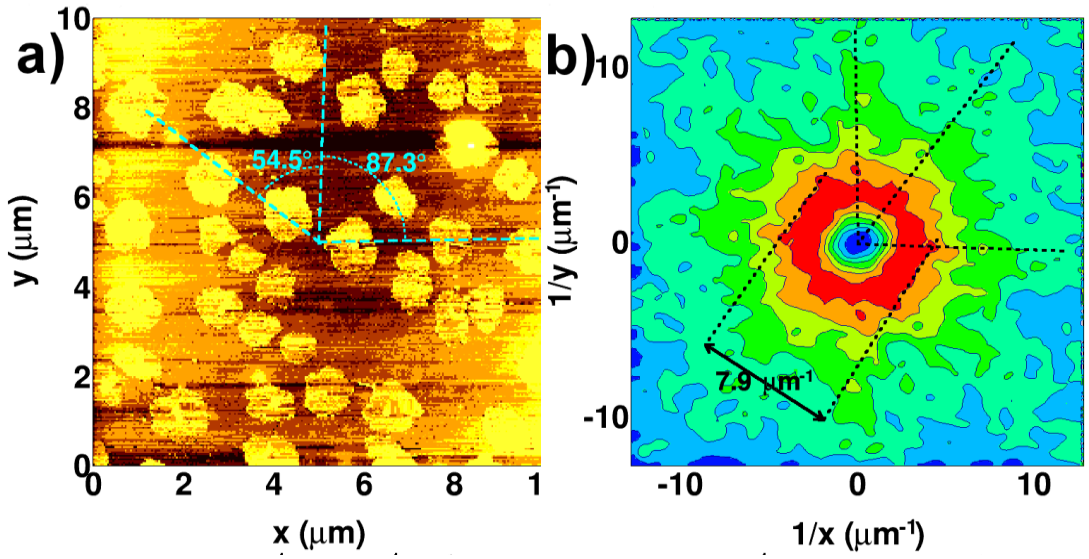

Fig. 6.9: (a) Morphology of pentacene on graphite. (b) Power spectra density of pentacene on graphite.

In Fig. 6.9a, we show the morphology of the pentacene layers deposited on the surface of MLG. At first glance the shape of these islands is disk-shaped and their position is random. However, smoothed PSDF map, presented in Fig. 6.9b reveals two characteristic features: (i) The PSDF exhibits straight edges along the directions, which are indicated with dashed lines originating from center. (ii) The highest PSDF contour has a hexagonal shape, with the diameter of 7.9 μm^{-1}. The corresponding to a hexagon in real space has a lattice of 250 nm and is rotated by 90°. The characteristic directions in real space, which correspond to the straight edges of PSDF map, are also

rotated and presented with dashed lines in Fig. 6.9a. The angle between these directions of 54.5º closely resembles the angle of hexagonal lattice (60º). In fact, the Fourier transform of a hexagon results in a PSDF of the shape of six symmetric edges with an angle of 60º between them. In addition, PSDF of randomly positioned hexagons in an ideal case exhibits a broadened six-star shape, which disappears, when hexagons are randomly rotated. Therefore, the shape of the PSDF of pentacene on HOPG indicates that the edges of pentacene islands prefer common hexagonal directions, which are likely to be determined by the underlying MLG surface.

6.4 Conclusion

In summary, we have investigated the morphology of pentacene islands on pristine SLG samples and graphene samples annealed at 350 °C in Ar by AFM. Surface characterization of graphene samples using AFM and Raman spectroscopy reveals that graphene on SiO_2 is more coarse and strained during annealing. A two-dimensional growth is observed on as prepared graphene while annealed graphene favors mostly three-dimensional growth at substrate temperature of 29 °C. The difference in pentacene morphology on annealed graphene sample is likely to be determined by depletion of water layer at the SiO_2/graphene interface. Also, pentacene on graphene transferred onto HMDS-treated SiO_2 also exhibits a 3D morphology. On the other hand, pentacene on many graphene layers transferred onto HMDS-treated SiO_2 exhibits 2D morphology due to change in surface energy of interfacial layers. Therefore, study of growth of organic molecules is an important issue as it is the growth mode of organic molecules on graphene that can control the potential of electronic devices.

7 Conclusions

In this thesis, we have studied the surface morphology of submonolayers of pentacene on graphene. Graphene samples were prepared by exfoliation of graphite and by chemical vapor deposition method.

In the first part of our research, we have investigated the growth of pentacene on graphene that was prepared by CVD method. CVD-graphene was transferred to SiO_2 substrate via wet chemical transfer route. PMMA was used as a support to transfer graphene from Cu foil to SiO_2. Graphene surface fabricated by this method comprised of folds on graphene – grafolds. When pentacene was deposited on such a surface, a 3D growth was observed. Interestingly, we have observed that most of pentacene islands are located near the grafolds (parallel to perpendicular the folds). The reason for accumulation of pentacene on grafolds was examined by Kelvin force microscopy. We have found that grafolds have different contact potential than unfolded graphene regions. The contact potentail difference between grafolds and unfolded graphene regions is 42 meV. In addition, such a pentacene morphology was not affected by the presence of PMMA residues on graphene surface which indicates the higher chemical reactivity at grafolds. Further investigations are required for determining the work functions of grafolds and the unfolded graphene.

After studying the growth of pentacene on CVD-graphene, we have focused on the study of early stages of growth of pentacene on exfoliated SLG and BLG. SLG and BLG were transferred onto 300 nm thick SiO_2 substrate. We have deposited submonolayers of pentacene on these samples. Our results from atomic force microscopy study reveal a two-dimensional growth on SLG and BLG in the range of substrate temperature from 10 ˚C to 60 ˚C. 2D islands have mean height 1.5 nm and this height indicates standing-up orientation of the molecules on graphene. Our findings show that for substrate temperature < 40 ˚C, islands are significantly smaller in size than the system size and island size distribution broadens with increasing temperature. At substrate temperatures 50 ˚C and 60 ˚C, coalescence occurs due to enlarged island size and this regime corresponds to percolation. However, we have observed a substantially different morphology of pentacene on SLG and BLG. The

island size distribution on SLG is broader and its centroid moves to higher mean island areas than on BLG. In addition to that, activation energy for molecule aggregation was investigated and is lower on SLG than on BLG. These differences in pentacene morphology on SLG and BLG are likely due to the dipole electric field which originates from water layer at graphene/SiO_2 interface.

We have extended our growth studies of pentacene on graphene to examine the influence of water layer on graphene/SiO_2 interface. Water layer at the interface lowers the surface energy of graphene due to diploe field. Therefore, surface energy plays a crucial role in determining the morphology of pentacene islands. Annealing was found to be an effective way to deplete water layer at the interface. Height difference between graphene and SiO_2 was ~ 1 nm for as exfoliated graphene that was reduced to ~ 0.5 nm on annealed graphene samples. A three-dimensional growth of pentacene on annealed graphene reveals the significant contribution from water layer. We have also performed similar experiment by treating SiO_2 substrate with HMDS prior pentacene deposition. HMDS makes surface hydrophobic and that leads to multilayer thick pentacene islands on graphene which have mean height 25 nm. However, the effect of surface treameant was not observed on pentacene islands deposited on MLG samples. Observed height of islands was 1.5 nm which is height of a monolayer of pentacene molecules. This shows that only the SLG on SiO_2 is influenced mostly by the treatment with HMDS due to close contact. Future studies should focus on detail investigation of molecular orientation of pentacene on exfoliated and on CVD-graphene. In addition, future studies should involve the finding of other organic molecules that are suitable to form organic patterns on graphene films. Since we have demonstrated that pentacene morphology is sensitive to the graphene layers and the underlying substrate treatment, other organic molecules should be studied for the same.

Bibliography

[1] K. S. Novoselov, A. K. Geim, S. V. Morozov, D. Jiang, Y. Zhang, S. V. Dubonos, I. V. Grigorieva and A. A. Firsov, Science **306**, 666 (2004).

[2] A. H. Castro Neto, F. Guinea, N. M. R. Peres, K. S. Novoselov and A. K. Geim, Rev. Mod. Phys. **81**, 109 (2009).

[3] K. S. Novoselov, D. Jiang, F. Schedin, T. J. Booth, V. V. Khotkevich, S. V. Morozov and A. K. Geim, Proc. Nati. Acad. Sci. **102**, 10451 (2005).

[4] S. J. Kang, B. Kim, K. S. Kim, Y. Zhao, Z. Chen, G. H. Lee, J. Hone, P. Kim and C. Nuckolls, Adv. Mater. **23**, 3531 (2011).

[5] G. Hong, Q.-H. Wu, J. Ren, C. Wang, W. Zhang and S.-T. Lee, Nano Today **8**, 388 (2013).

[6] A. Dodabalapur, L. Torsi and H. E. Katz, Science **268**, 270 (1995).

[7] W. H. Lee, J. Park, S. H. Sim, S. Lim, K. S. Kim, B. H. Hong and K. Cho, J. Am. Chem. Soc. **133**, 4447 (2011).

[8] X. Q. Tian, J. B. Xu and X. M. Wang, J. Phys. Chem. C **114**, 20917 (2010).

[9] C. C. Mattheus, A. B. Dros, J. Baas, A. Meetsma, J. L. d. Boer and T. T. M. Palstra, Acta Crystallogr. Sec. C **57**, 939 (2001).

[10] L. Casalis, M. F. Danisman, B. Nickel, G. Bracco, T. Toccoli, S. Iannotta and G. Scoles, Phys. Rev. Lett. **90**, 206101 (2003).

[11] S. R. Forrest, Chem. Rev. **97**, 1793 (1997).

[12] S. Pratontep, M. Brinkmann, F. Nüesch and L. Zuppiroli, Synt. Met. **146**, 387 (2004).

[13] B. Stadlober, U. Haas, H. Maresch and A. Haase, Phys. Rev. B **74**, 165302 (2006).

[14] G. Yoshikawa, J. T. Sadowski, A. Al-Mahboob, Y. Fujikawa, T. Sakurai, Y. Tsuruma, S. Ikeda and K. Saiki, Appl. Phys. Lett. **90** 251906 (2007).

[15] H. Zhou, L. Zhang, J. Mao, G. Li, Y. Zhang, Y. Wang, S. Du, W. Hofer and H.-J. Gao, Nano Res. **6**, 131 (2013).

[16] A. Charrier, A. Coati, T. Argunova, F. Thibaudau, Y. Garreau, R. Pinchaux, I. Forbeaux, J.-M. Debever, M. Sauvage-Simkin and J.-M. Themlin, J. Appl. Phys. **92**, 2479 (2002).

[17] S. Bae, H. Kim.Y. Lee, X. Xu, J.-S. Park,Y. Zheng, J. Balakrishnan, T. Lei, H. R. Kim, Y. song, Y.-J. Kim, K. S. Kim, B. Ozyilmaz, J.-H. Ahn, B. H. Hong and S. Lijima, Nat. Nanotechnol. **5**, 574 (2010)

[18] K. Kim, Z. Lee, B. D. Malone, K. T. Chan, B. Aleman, W. Regan, W. Gannett, M. F. Crommie, M. L. Cohen and A. Zetti, Phys. Rev. B **83**, 245433 (2011).

[20] N. Koch, A. Vollmer, I. Salzmann, B. Nickel, H. Weiss and J. P. Rabe, Phys. Rev. Lett. **96**, 156803 (2006).

[21] M. Chhikara, E. Pavlica and G. Bratina, Surf. Sci. **609**, L5 (2013).

[22] M. Chhikara, E. Pavlica, A. Matković, A. Beltaos, R. Gajić and G. Bratina, Carbon **69**, 162 (2014).

[23] P. Jensen, Rev. Mod. Phys. **71**, 1695 (1999).

[24] S. Dushman, *Scientific foundations of vacuum technique* (Wiley, 1962).

[25] C. Ratsch and J. A. Venables, J. Vac. Sci. & Technol. A **21**, S96 (2003).

[26] I. V. Markov, *Crystal Growth for Beginners: Fundamentals of Nucleation, Crystal Growth, and Epitaxy* (World Scientific Publishing Company, 1995).

[27] S. Pratontep, M. Brinkmann, F. Nüesch and L. Zuppiroli, Phys. Rev. B **69**, 165201 (2004).

[28] S. Pratontep, F. Nüesch, L. Zuppiroli and M. Brinkmann, Phys. Rev. B **72**, 085211 (2005).

[29] F. Schreiber, Phys. Stat. Sol. **201**, 1037 (2004).

[31] B. Cappella and G. Dietler, Surf. Sci. Rep. **34**, 1 (1999).

[32] D. Nečas and P. Klapetek, Cent. Eur. J. Phys. **10**, 181 (2012).

[33] S. Sadewasser and C. Barth, in *Characterization of Materials* (John Wiley, 2002).

[34] W. Melitz, J. Shen, A. C. Kummel and S. Lee, Surf. Sci. Rep. **66**, 1 (2011).

[35] A. C. Ferrari, J. C. Mayer, V. Scardaci, C. Casiraghi, M. Lazzeri, F. Mauri, S. Piscanec, D. Jiang, K. S. Novoselov, S. Roth and A. K. Geim, Phys. Rev. Lett. **97**, 187401 (2006).

[36] A. C. Ferrari and D. M. Basko, Nat. Nanotechnol. **8**, 235 (2013).

[37] L. M. Malard, M. A. Pimenta, G. Dresselhaus and M. S. Dresselhaus, Phys. Rep. **473**, 51 (2009).

[38] H. Shioyama and J. Mater. Sci. Lett. **20**, 499 (2001).

[39] N. D. Mermin, Phys. Rev. **176**, 250 (1968).

[40] D. S. L. Abergel, A. Russell and V. I. Fal'ko, Appl. Phys. Lett. **91** 063125 (2007).

[41] S. D. Sarma, S. Adam, E. H. Hwang and E. Rossi, Rev. Mod. Phys. **83**, 407 (2011).

[42] C. Lee, X. Wei, J. W. Kysar and J. Hone, Science **321**, 385 (2008).

[43] Q. Wang, D. X. Ye, Y. Kawazoe and P. Jena, Phys. Rev. B **85**, 085404 (2012).

[44] C. Casiraghi, A. Hartschuh, E. Lidorikis, H. Qian, H. Harutyunyan, T. Gokus, K. S. Novoselov and A. C. Ferrari, Nano Lett. **7**, 2711 (2007).

[45] M. Ishigami, J. H. Chen, W. G. Cullen, M. S. Fuhrer and E. D. Williams, Nano Lett. **7**, 1643 (2007).

[46] S. Niyogi, E. Bekyarova, M. E. Itkis, J. L. McWilliams, M. A. Hamon and R. C. Haddon, J. Am. Chem. Soc. **128**, 7720 (2006).

[47] S. Sasha, A. D. Dmitriy, H. B. D. Geoffrey, M. K. Kevin, J. Z. Eric, A. S. Eric, D. P. Richard, T. N. SonBinh and S. R. Rodney, Nature **442**, 282 (2006).

[48] C. Berger, Z. Song, T. Li, X. Li, A. Y. Ogbazghi, R. Feng, Z. Dai, A. N. Marchenkov, E. H. Conrad, P. N. First and W. A. de Heer, J. Phys. Chem. B **108**, 19912 (2004).

[49] W. A. de Heer, C. Berger, X. Wu, P. N. First, E. H. Conrad, X. Li, T. Li, M. Sprinkle, J. Hass, M. L. Sadowski, M. Potemksi and G. Martinezet, Solid State Commun. **143**, 92 (2007).

[50] H. Park, P. R. Brown, V. Bulović and J. Kong, Nano Lett. **12**, 133 (2011).

[51] K. S. Kim, Y. Zhao, H. Jang, S. Y. Lee, J. M. Kim, J. H. Ahn, P. Kim, J. Y. Choi and B. H. Hong, Nature **457**, 706 (2009).

[52] A. Kumar and C. H. Lee (InTech, 2013).

[53] B. C. Banerjee, T. J. Hirt and P. L. Walker, Nature **192**, 450 (1961).

[54] C. Mattevi, H. Kim and M. Chhowalla, J. Mater. Chem. **21**, 3324 (2011).

[55] X. Li, W. Cai, J. An, S. Kim, J. Nah, D. Yang, R. Piner, A. Velamakanni, I. Jung, E. Tutuc, S. K. Benerjee, L. Colombo and R. S. Ruoff, Science **324**, 1312 (2009).

[56] X. Li, Y. Zhu, W. Cai, M. Borysiak, B. Han, D. Chen, R. D. Piner, L. Colombo and R. S. Ruoff, Nano Lett. **9**, 4359 (2009).

[57] Y. Ren, C. Zhu, W. Cai, H. Li, Y. Hao, Y. Wu, S. Chen, Q. Wu, R. D. Piner and R. S. Rouff, Nano **7**, 1150001 (2012).

[58] S. P. Koenig, N. G. Boddeti, M. L. Dunn and J. S. Bunch, Nat. Nanotechnol. **6**, 543 (2011).

[59] H. Anders, *Thin Films in Optics* (Focal Press, 1965).

[60] P. Blake, E. W. Hill, A. H. Castro Neto, K. S. Novoselov, D. Jiang, R. Yang, T. J. Booth and A. K. Geim, Appl. Phys. Lett. **91** (2007).

[61] Z. H. Ni, H. M. Wang, J. Kasim, H. M. Fan, T. Yu, Y. H. Wu, Y. P. Feng and Z. X. Shen, Nano Lett. **7**, 2758 (2007).

[62] P. Sutter, Nat. Mater. **8**, 171 (2009).

[63] E. Rollings, G.-H. Gweon, S. Y. Zhou, B. S. Mun, J. L. McChesney, B. S. Hussain, A. V. Fedorov, P. N. first, W. A. de Heer and A. Lanzaraet, J. Phys. Chem. Solids **67**, 2172 (2006).

[64] W. A. de Heer, C. Berger, M. Ruan, M. Sprinkle, X. Li, Y. Hu, B. Zhang, J. Hankinson and E. Conrad, Proc. Nati. Acad. Sci. **108**, 16900 (2011).

[65] W. S. Hummers and R. E. Offeman, J. Am. Chem. Soc. **80**, 1339 (1958).

[66] C. Nethravathi and M. Rajamathi, Carbon **46**, 1994 (2008).

[67] D. C. Marcano, D. V. Kosynkin, J. M. Berlin, A. Sinitskii, Z. Sun, A. Slesarev, L. B. Alemany, W. Lu and J. M. Tour, ACS Nano **4**, 4806 (2010).

[68] D. R. Dreyer, S. Park, C. W. Bielawski and R. S. Ruoff, Chem. Soc. Rev. **39**, 228 (2010).

[69] S. Wang, Y. Zhang, N. Abidi and L. Cabrales, Langmuir **25**, 11078 (2009).

[70] S. Stankovich, D. A. Dikin, G. H. Dommett, K. M. Kohlhaas, E. J. Zimney, E. A. Stach, R. D. Piner, S. T. Nguyen and R. S. Ruoff, Nature **442**, 282 (2006).

[71] K. Jasuja, J. Linn, S. Melton and V. Berry, J. Phys. Chem. Lett. **1**, 1853 (2010).

[72] G. K. Ramesha and S. Sampath, J. Phys. Chem. C **113**, 7985 (2009).

[73] Y. H. Ng, I. V. Lightcap, K. Goodwin, M. Matsumura and P. V. Kamat, J. Phys. Chem. Lett. **1**, 2222 (2010).

[74] Q. Xiang, J. Yu and M. Jaroniec, Chem. Soc. Rev. **41**, 782 (2012).

[75] C. D. Dimitrakopoulos and P. R. L. Malenfant, Adv. Mater. **14**, 99 (2002).

[76] T. Siegrist, C. Kloc, J. H. Schön, B. Batlogg, R. C. Haddon, S. Berg and G. A. Thomas, Angewandte Chemie International Edition **40**, 1732 (2001).

[77] C. D. Dimitrakopoulos, A. R. Brown and A. Pomp, J. Appl. Phys. **80**, 2501 (1996).

[78] C. C. Mattheus, A. B. Dros, J. Baas, G. T. Oostergetel, A. Meetsma, J. L. de Boer and T. T. M. Palstra, Synt. Met. **138**, 475 (2003).

[79] C. Ambrosch-Draxl, D. Nabok, P. Puschnig and C. Meisenbichler, New J. Phys. **11**, 125010 (2009).

[80] R. B. Campbell, J. M. Robertson and J. Trotter, Acta Cryst. **15**, 289 (1962).

[81] H. Brune, Surf. Sci. Rep. **31**, 125 (1998).

[82] B. Voigtländer, Surf. Sci. Rep. **43**, 127 (2001).

[83] F. Family, J. Stat. Phys. **83**, 1255 (1996)

[84] R. Q. Hwang and M. C. Bartelt, Chem. Rev. **97**, 1063 (1997).

[85] B. A. Joyce, Adv. Mater. **5**, 773 (1993).

[86] M. C. Bartelt and J. W. Evans, Phys. Rev. B **54**, R17359 (1996).

[87] S. Clarke and D. D. Vvedensky, J. Appl. Phys. **63**, 2272 (1988).

[88] M. C. Bartelt and J. W. Evans, Phys. Rev. B **46**, 12675 (1992).

[89] T. Vicsek and F. Family, Phys. Rev. Lett. **52**, 1669 (1984).

[90] F. Family and P. Meakin, Phys. Rev. Lett. **61**, 428 (1988).

[91] R. Ruiz, B. Nickel, N. Koch, L. C. Feldman, R. F. Haglund, A. Kahn, F. Family and G. Scoles, Phys. Rev. Lett. **91**, 136102 (2003).

[92] J. G. Amar, F. Family and P.-M. Lam, Phys. Rev. B **50**, 8781 (1994).

[93] J. G. Amar and F. Family, Phys. Rev. Lett. **74**, 2066 (1995).

[94] J. A. Blackman and A. Wilding, Europhys. Lett. **16**, 115 (1991).

[95] J. A. Stroscio, D. T. Pierce and R. A. Dragoset, Phys. Rev. Lett. **70**, 3615 (1993).

[96] E. Kopatzki, S. Günther, W. Nichtl-Pecher and R. J. Behm, Surf. Sci. **284**, 154 (1993).

[97] Y. W. Mo, J. Kleiner, M. B. Webb and M. G. Lagally, Phys. Rev. Lett. **66**, 1998 (1991).

[98] H.-J. Ernst, F. Fabre and J. Lapujoulade, Phys. Rev. B **46**, 1929 (1992).

[99] W. Li, G. Vidali and O. Biham, Phys. Rev. B **48**, 8336 (1993).

[100] R. Q. Hwang, J. Schröder, C. Günther and R. J. Behm, Phys. Rev. Lett. **67**, 3279 (1991).

[101] J. K. Zuo and J. F. Wendelken, Phys. Rev. Lett. **66**, 2227 (1991).

[102] T. Michely, M. Hohage, M. Bott and G. Comsa, Phys. Rev. Lett. **70**, 3943 (1993).

[103] R. Stumpf and M. Scheffler, Phys. Rev. Lett. **72**, 254 (1994).

[104] D. Choudhary, P. Clancy, R. Shetty and F. Escobedo, Adv. Funct. Mater. **16**, 1768 (2006).

[105] F. Dinelli, M. Murgia, P. Levy, M. Cavallini, F. Biscarini and D. M. de Leeuw, Phys. Rev. Lett. **92**, 116802 (2004).

[106] F.-J. Meyer zu Heringdorf, M. C. Reuter and R. M. Tromp, Nature **412**, 517 (2001).

[107] R. Ruiz, B. Nickel, N. Koch, L. C. Feldman, R. F. Haglund, A. Kahn and G. Scoles, Phys. Rev. B **67**, 125406 (2003).

[108] D. Knipp, R. A. Street, A. Völkel and J. Ho, J. Appl. Phys. **93**, 347 (2003).

[109] A. C. Mayer, R. Ruiz, R. L. Headrick, A. Kazimirov and G. G. Malliaras, Org. Electron. **5**, 257 (2004).

[110] S. E. Fritz, S. M. Martin, C. D. Frisbie, M. D. Ward and M. F. Toney, J. Am. Chem. Soc. **126**, 4084 (2004).

[111] M. Shtein, J. Mapel, J. B. Benziger and S. R. Forrest, Appl. Phys. Lett. **81**, 268 (2002).

[112] H. Yang, T. J. Shin, M.-M. Ling, K. Cho, C. Y. Ryu and Z. Bao, J. Am. Chem. Soc. **127**, 11542 (2005).

[113] P. R. Ribič, V. Kalihari, C. D. Frisbie and G. Bratina, Phys. Rev. B **80**, 115307 (2009).

[114] S. Lukas, G. Witte and C. Wöll, Phys. Rev. Lett. **88**, 028301 (2001).

[115] P. Guaino, A. A. Cafolla, D. Carty, G. Sheerin and G. Hughes, Surf. Sci. **540**, 107 (2003).

[116] P. G. Schroeder, C. B. France, J. B. Park and B. A. Parkinson, J. Appl. Phys. **91**, 3010 (2002).

[117] Y. Harada, H. Ozaki and K. Ohno, Phys. Rev. Lett. **52**, 2269 (1984).

[118] S. D. Chakarova-Käck, E. Schröder, B. I. Lundqvist and D. C. Langreth, Phys. Rev. Lett. **96**, 146107 (2006).

[119] P. B. Paramonov, V. Coropceanu and J.-L. Brédas, Phys. Rev. B **78**, 041403 (2008).

[120] J. Götzen, D. Käfer, C. Wöll and G. Witte, Phys. Rev. B **81**, 085440 (2010).

[121] Y. Zheng, N. Wei, Z. Fan, L. Xu and Z. Huang, Nanotechnology **22**, 405701 (2011).

[122] A. T. N'Diaye, R. V. Gastel, A. J. Martinez-Galera, J. Coraux, H. Hattab, D. Wall, F.-J. M. zu Heringdorf, M. H. Hoegen, J. M. Gomez-Rodriguez, B. Poelsema, C. Busse and T. Mochelyet, New J. Phys. **11**, 113056 (2009).

[123] L. X. Benedict, N. G. Chopra, M. L. Cohen, A. Zettl, S. G. Louie and V. H. Crespi, Chem. Phys. Lett. **286**, 490 (1998).

[124] G. Hlawacek, F. S. Khokhar, R. van Gastel, B. Poelsema and C. Teichert, Nano Lett. **11**, 333 (2011).

[125] G. Hlawacek, F. S. Khokar, R. Van Gastel, C. Teichert and B. Poelsema, IBM J. Res. Dev. **55**, 15 (2011).

[126] M. Her, R. Beams and L. Novotny, Phys. Lett. A **377**, 1455 (2013).

[127] S. Lee, G. Jo, S.-J. Kang, G. Wang, M. Choe, W. Park, D.-Y. Kim, Y. H. Kahng and T. Lee, Adv. Mater. **23**, 100 (2011).

[128] J. Tersoff and R. M. Tromp, Phys. Rev. Lett. **70**, 2782 (1993).

[129] S. Park, D. Srivastava and K. Cho, Nano Lett. **3**, 1273 (2003).

[130] J. E. Northrup, M. L. Tiago and S. G. Louie, Phys. Rev. B **66**, 121404 (2002).

[131] D. K. Owens and R. C. Wendt, J. Appl. Poly. Sci. **13**, 1741 (1969).

[132] T. C. Nguyen, M. Otani and S. Okada, Phys. Rev. Lett. **106**, 106801 (2011).

[133] K. Kajihara, M. Hirano, L. Skuja and H. Hosono, Phys. Rev. B **72**, 214112 (2005).

[134] J. Sabio, C. Seoánez, S. Fratini, F. Guinea, A. H. C. Neto and F. Sols, Phys. Rev. B **77**, 195409 (2008).

[135] W. Gao and R. Huang, J. Phys. D: Appl. Phys. **44**, 452001 (2011).

[136] J. Rafiee, X. Mi, H. Gullapalli, A. V. Thomas, F. Yavari, Y. Shi, P. M. Ajayan and N. A. Koratkar, Nat. Mater. **11**, 217 (2012).

[137] C.-J. Shih, Q. H. Wang, S. Lin, K.-C. Park, Z. Jin, M. S. Strano and D. Blankschtein, Phys. Rev. Lett. **109**, 176101 (2012).

[138] Z. Li, Y. Wang, A. Kozbial, G. Shenoy, F. Zhou, R. mcGinley, P. Ireland, B. Morganstein, A. Kunkel, S. P. Surwade, L. Li and H. Liuet, Nat. Mater. **12**, 925 (2013).

[139] S. Wang, Y. Zhang, N. Abidi and L. Cabrales, Langmuir **25**, 11078 (2009).

[140] J. F. Dobson, A. White and A. Rubio, Phys. Rev. Lett. **96**, 073201 (2006).

[141] Y. Y. Lin, D. J. Gundlach, S. F. Nelson and T. N. Jackson, IEEE Trans. Electron Dev. **44**, 1325 (1997).

[142] R. Ruiz, D. Choudhary, B. Nickel, T. Toccoli, K.-C. Chang, A. C. Mayer, P. Clancy, J. M. Blakely, R. L. Headrick, S. Ianotta and G. G. Malliaras, Chem. Mater. **16**, 4497 (2004).

[143] A. Gupta, G. Chen, P. Joshi, S. Tadigadapa and P. C. Eklund, Nano Lett. **6**, 2667 (2006).

[144] P. Nemes-Incze, Z. Osváth, K. Kamarás and L. P. Biró, Carbon **46**, 1435 (2008).

[145] A. Matković, A. Beltaos, M. Milićević, U. Ralević, B. Vasić, D. Jovanović and R. Gajić, J. Appl. Phys. **112**, 093505 (2012).

[146] Q. H. Wang and M. C. Hersam, Nat. Chem. **1**, 206 (2009).

[147] J. W. Evans, P. A. Thiel and M. C. Bartelt, Surf. Sci. Rep. **61**, 1 (2006).

[148] W. W. Mullins, J. Appl. Phys. **59**, 1341 (1986).

[149] M. Lafkioti, B. Krauss, T. Lohmann, U. Zschieschang, H. Klauk, K. V. Klitzing and J. H. Smet, Nano Lett. **10**, 1149 (2010).

[150] L. Liu, Z. Chen, L. Wang, E. Polyakova, T. Taniguchi, K. Watanabe, J. Hone, G. W. Flynn and L. E. Brus, J. Phys. Chem. B **117**, 4305 (2012).

[151] H. G. Zhang, J. T. Sun, T. Low, L. Z. Zhang, Y. Pan, Q. Liu, J. H. Mao, H. T. Zhou, H. M. Gou, S. X. Du, F. Guinea and H.-J. Gao, Phys. Rev. B **84**, 245436 (2011).

[152] P. Lazar, F. Karlický, P. Jurečka, M. Kocman, E. Otyepková, K. Šafářová and M. Otyepka, J. Am. Chem. Soc. **135**, 6372 (2013).

[153] A. J. Martínez-Galera and J. M. Gómez-Rodríguez, J. Phys. Chem. C **115**, 23036 (2011).

[154] X. Ling, L. Xie, Y. Fang, H. Xu, H. Zhang, J. Kong, M. S. Dresselhaus, J. Zhang and Z. Liu, Nano Lett. **10**, 553 (2009).

[155] A. Brillante, I. Bilotti, R. G. D. Valle, E. Venuti, A. Girlando, M. Masino, F. Liscio, S. Milita, C. Albonetti, P. D'angelo, A. Shehu and F. Biscarini, Phys. Rev. B **85**, 195308 (2012).

[156] W. Chen, H. Huang, A. Thye and S. Wee, Chem. Commun., 4276 (2008).

[157] A. Nourbakhsh, M. Cantoro, A. Klekachev, F. Clemente, B. Soree, M. H. van der Veen, T. Vosch, A. Stesmans, B. Sels and S. D. Gendt, J. Phys. Chem. C **114**, 6894 (2010).

[158] X. Liu, A. Grüneis, D. Haberer, A. V. Fedorov, O. Vilkov, W. Strupinski and T. Pichler, J. Phys. Chem. C **117**, 3969 (2013).

[159] S. Ryu, L. Liu, S. Berciaud, Y.-J. Yu, H. Liu, P. Kim, G. W. Flynn and L. E. Brus, Nano Lett. **10**, 4944 (2010).

[160] A. Das, S. Pisana, B. Choudhary, S. Piscanec, S. K. Saha, U. V. Waghmare, K. S. Novoselov, H. R. Krishnamurthy, A. K. Geim, A. C. Ferrari and A. K. Sood, Nat. Nanotechnol. **3**, 210 (2008).

[161] Z. H. Ni, T. Yu, Y. H. Lu, Y. Y. Wang, Y. P. Feng and Z. X. Shen, ACS Nano **2**, 2301 (2008).

[162] Z. H. Ni, H. M. Wang, Y. Ma, J. Kasim, Y. H. Wu and Z. X. Shen, ACS Nano **2**, 1033 (2008).

[163] C. Metzger, S. Rémi, M. Liu, S. V. Kusminskiy, A. H. Castro Neto, A. K. Swan and B. B. Goldberg, Nano Lett. **10**, 6 (2009).

[164] H. Walk, in *Modeling Uncertainty*, edited by M. Dror, P. L'Ecuyer and F. Szidarovszky (Springer US, 2005).